UNIVERSITÀ DEGLI STUDI DI NAPOLI
FEDERICO II

DIPARTIMENTO DI INGEGNERIA INDUSTRIALE
Dottorato di Ricerca in Ingegneria Industriale

PREDICTION OF THE PROPULSION PERFORMANCES OF PLANING STEPPED HULLS: CFD IN SUPPORT OF EXPERIMENTAL TOWING TANK TESTS

Raffaele Scognamiglio

Tutor
Prof. Ing. Salvatore Miranda

Coordinatore
Prof. Ing. Michele Grassi

XXIX Ciclo

PREDICTION OF THE PROPULSION PERFORMANCES OF PLANING STEPPED HULLS: CFD IN SUPPORT OF EXPERIMENTAL TOWING TANK TESTS

raffaele.scognamiglio@unina.it

Department of Industrial Engineering, University of Naples Federico II, P.le V. Tecchio n. 80, 80125 Napoli (ITALY)

ABSTRACT

As it is clear, nowadays, the Computer Fluid Dynamics (CFD) has become a fundamental support for the hydrodynamic investigations in order to perform detailed analysis and to reduce the number of more expensive towing tank tests, which are, however, always necessary alongside for validation of numerical results. Indeed, for CFD applications in ship hydrodynamic field it is well known that the numerical simulations of high speed planing hulls are significantly less reliable those regarding displacement hulls. In particular for the stepped hulls, the physics of the hydrodynamic field is quite complex, more than for planing hulls; This is why it is important to perform a comprehensive approach for verification and validation (V&V) methodologies and procedures in order to obtain high-quality results of CFD simulations.

In the first part of this thesis, a new systematic series of eight hull models derived by one stepped hull is developed. In detail, the factors considered crucial for the experimental tests and for the physics of the hydrodynamic field are changed for each of the above models. The experimental tests are carried out in towing tank, through the “down thrust” methodology, to investigate the hull performances *i.e.*, total resistance, longitudinal trim angle, sinkage, and wetted surface. Moreover, a detailed investigation of the flow phenomena in the separated region behind the step is carried out on one of the eight hull models, which has a single-step.

In the second part, for the same single-step hull model, an assessment of the accuracy and effectiveness of different simulations setups and techniques is performed, with particular attention to the different techniques of moving mesh, such as the overset/chimera grid and morphing mesh. Afterwards, the V&V study is performed for one hull model belonging to the systematic series, and

the Unsteady Reynolds Average Navier Stokes (URANS) code results are validated by using benchmark experimental data.

The analysis of grid independence, iteration, time-step, and statistical convergence analysis for measured variables, performances *i.e.*, total resistance, longitudinal trim angle, sinkage, and wetted surface, is performed by using the deterministic methods available in the literature for uncertainty estimation.

Results of this work show that the numerical results are in good accordance with the experimental data, and the overset/chimera grid is found to be the best approach between the analyzed ones.

In addition, another contribution of this work is the detailed reading of the vortex structures in the unwetted aft body area behind the step (within the air region), and their development into the downstream water flow. The flow patterns observed in numerical test through Large Eddy Simulations on a very refined grid, appear similar to the ones observed in towing tank investigations through photographic acquisitions.

Contents

Figure Index

Table Index

Nomenclature

B	Breadth (m)
B_r	Bias systematic uncertainty
c_j	Basis constant
C_k	Correction factor
d	Vertex displacement
E	Comparison error
D	Experimental data
Fr_∇	Volumetric Froude number
F_s	Factor of safety
Fr	Froude number
g	Gravity acceleration
K	Constant value in Eq. (A.1)
L_{WL}	Water line length (m)
L_{OA}	Length overall (m)
n	Number of control vertices
S_n	Numerical simulation result
p_k	Observed order of accuracy
P_E	Effective power (kW)
P_r	Precision uncertainty
r_{ij}	Magnitude of distance between two vertices
r_k	Refinement ratio
R_k	Convergence ratio
R_{TM}	Total model resistance (kg)
S	Wetted surface (m^2)

$SDev_j$	standard deviation of j^{th} run
U	Uncertainty
U_r	Total uncertainty
U_k	*k*-input parameter uncertainty
U_I	Iterative uncertainty
U_G	Grid uncertainty
U_{TS}	Time step uncertainty
U_{SN}	Numerical simulation uncertainty
U_V	Validation uncertainty
U_D	Experimental data uncertainty
V	Hull speed (m/s)
Z	Sinkage (m)
∇	Displacement volume (m^3)

Greek symbols

α	Volume fraction
Δ	Displacement weight (N)
ε	Solution change
ρ_M	Towing tank water density (Kg/m^3)
ρ_S	Sea water density (kg/m^3)
λ	Expansion coefficient in Eq.(4.14) and model scale
Δt	Time step (s)
τ	Dynamic trim angle (deg)

Acronyms

AIAA	American Institute of Aeronautics and Astronautics
AMG	Algebraic Multi Grid
ASME	American Society of Mechanical Engineer
CF	Correction Factor
CFD	Computational Fluid Dynamics
CFL	Courant Friedrichs Lewy number
CNC	Computer Numerical Control
DAQ	Data acquisition device
DFBI	Dynamic Fluid Body Interaction
DOF	Degree of Freedom
DT	Down Thrust
EFD	Experimental Fluid Dynamics
FRP	Fiber Reinforced Plastic
GCI	Grid Convergence Index
HRIC	High Resolution Interface Capturing Scheme
ITTC	International Towing Tank Conference
LCB	Longitudinal Centre of Buoyancy
LCG	Longitudinal Centre of Gravity
LES	Large Eddy Simulation
NV	Numerical Ventilation
PVC	Polyvinyl Chloride
RANS	Reynolds Average Navier-Stokes
RBF	Radial Basic Function

RBM	Rigid Body Motion
RE	Richardson Extrapolation
RIB	Rigid Inflatable Boat
RSS	Root Sum Square
SIMPLE	Semi Implicit Method Pressure Linked Equations
SST	Shear Stress Transport
UA	Uncertainty Analysis
VOF	Volume Of Fluid
V&V	Verification And Validation

1

INTRODUCTION

Nowadays, Computational Fluid Dynamics (CFD) is widely used in all engineering fields. In the last 20 years, the CFD for ship hydrodynamics has surpassed all expectations by reaching significant progress and capabilities. Hull resistance prediction is the oldest application of CFD in ship hydrodynamics and in these years a great number of simulations have been carried out for a wide range of applications and conditions. Other than drag, sinkage and trim, local flow fields such as boundary layer and wake, and wave patterns are also predicted. Different geometries including tankers, container ships, surface combatants, and small vessels are studied in a range from very small to large Froude Numbers.

As it is clear, the CFD has become a fundamental support in order to predict ship's performance but CFD modeling as an engineering tool can be justified only on the basis of its accuracy and level of confidence of the results. Therefore, it is recognized that errors and uncertainty are unavoidable aspects of CFD modeling, and it is necessary to establish rigorous procedures to quantify the level of confidence of the results. These procedures are the verification and validation (V&V) processes. The process of verification involves quantification of the errors and the process of validation involves quantification of the input uncertainty and physical model uncertainty. Instead, regarding to experimental data, the assessment of uncertainty is a well-established practice, and the relevant techniques form part of every engineer's basic education.

Over the recent years, the accuracy of hull resistance simulations has improved significantly. Indeed, as reported in Stern et al. [1], a statistical analysis shows that in the 2010 Gothenburg Workshop [2, 3] the average error of the results of all resistance test simulations is 2.1 % rather than 4.7 % which was the average error evaluated during the Gothenburg Workshop 2005. Furthermore,

the uncertainty related to the simulation is around 4.0%. This improvement is reached for the displacement or "conventional" ship.

Conversely, for unconventional ships such as multi-hulls, planing boats, stepped hulls, with reference to the last CFD Committee Report of ITTC, "*prediction error of less than 10% could be achieved compared to the model-scale and full-scale test results"*[4].

In the hydrodynamics field of high speed planing hulls, largest errors in the resistance evaluations are related to the errors in the evaluation of the dynamic trim. This interpretation is based on the observed magnitudes of the errors of the numerically predicted trim and on the well-known relationship between dynamic trim and resistance at high speed, *i.e.*, $R_T = L \cdot tg(\tau) + R_V$. In this equation, given by Sottorf [5], R_T is the total resistance, $L \cdot tg(\tau)$ is the resistance induced to the lift with τ as the dynamic trim, R_V is the viscous resistance of the bare hull. This equation is valid for totally planing hulls but it also effectively describes the dependency of the trim angle on the resistance components. Moreover, it is worth noticing that, in the small trim angle range, which is typical for stepped planing hulls because sailed always on (n+1) wetted triangle (where n represent the steps number), also R_V is influenced by the trim because of the significant variations of the wetted surfaces; therefore, an incorrect quantification of the trim results in errors in both of the resistance components. The difficulty in identifying the dynamic trim is strongly due to the difficulties in identifying the center of pressure, or, generally, the pressure distribution on the hull bottom. The identification of pressure distribution is affected significantly by the edge effects and by the percentage of hydrodynamic lifts to sustain the stepped hull.

After developing a new systematic series of eight hull models derived by a parent stepped hull with corresponding experimental tests, the purpose of this study is to establish an integrated approach between experimental tests for one of the hull models, and the related CFD investigations. For these latter, the (U)RANS based codes are used with the aim to investigate the quite complex hydrodynamic field generated by the stepped hulls; particular attention is given to the simulation of the resistance tests. Hence, more than one mesh approaches are used for the body motion simulation, such as the overset/chimera grid and morphing mesh technique in order to achieve good numerical convergence and to capture the vortical structures observed in towing tank tests. In fact, performances of planing stepped hulls are more sensitive to the hull position (sinkage and trim) as compared to displacement hulls [6]. For this reason, accurate simulations of the hull motion are necessary. In detail, non-conventional approaches (*i.e.*, overset mesh and morphing grid) for the simulation of the hull motion are required, as indicated in [7]. Furthermore, this study presents a

detailed study of the vortex structures in the unwetted aft body area and their development into the downstream water flow by means of photographic acquisitions and Large Eddy Simulations (LES) on a very refined grid.

2

PERFORMANCE PREDICTION OF STEPPED HULLS

2.1. Introduction

In the last years, the development of light weight engines and propulsion systems, and the development of lighter boats built by shipyards with new technology and materials imposed to designer to pay increasing attention on the hull design. The engine weight reduction is carried out by using composite materials or aluminum alloys, whereas the power increase is ensured by turbocharge and electronic control. As a consequence, outboards engines with a very low weight/power ratio can be attained, which are more reliable and used for military, commercial, pleasure or racing.

The new composite materials as pre-preg with low temperature curing or the lamination building techniques as the infusion resin allow a boat weight reduction of 30% as compared with a traditional hand-made layup. In this scenario, in recent years, the high speed planing craft for several final uses, with a very low weight/power ratio have spread even more. The reduction of the weight/power ratio allows to increase the maximum speed, and, as a consequence, naval architects are oriented even more in stepped planing hull design to reduce the resistance at high speed and ensuring a good dynamic stability and seakeeping at high speed.

The classification of advanced vehicles and their hybrid derivation usually follows the classical sustention triangle [8]. The corners of this triangle represent the vessels supported by hydrostatic buoyancy, hydrodynamic lift and powered lift. The edges and the inside of the triangle represent the

hybrids, *Figure 2.1*. Planing boats and, therefore, the stepped hull move to the right side of the triangle as a speed variation occurs.

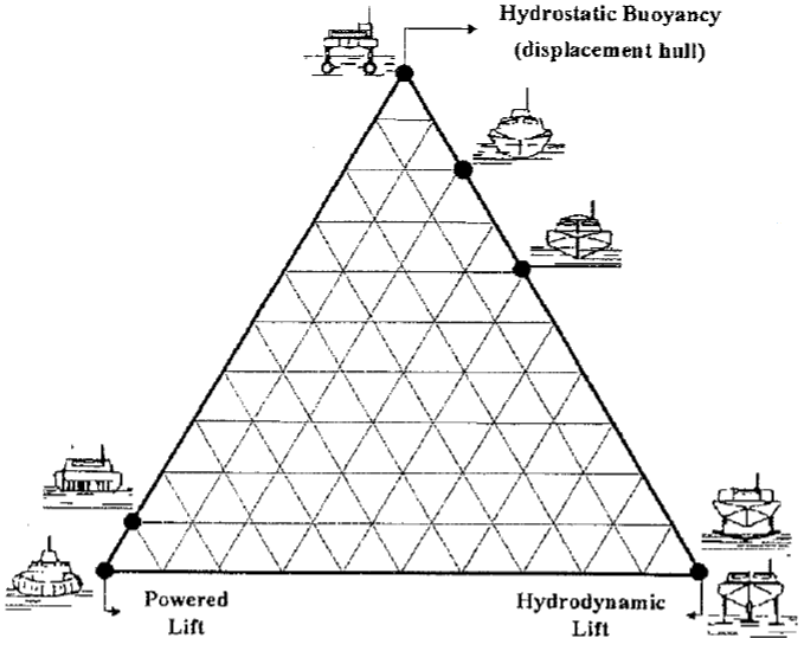

Figure 2. 1. Sustention triangle [8]

2.2. History of the stepped hull

The first stepped hulls were originally proposed by Rev. Ramus of Sussex England in 1872. Probably the first systematic and scientific data, also useful for planing hulls, were obtained by the experimental tests on the model stepped hulls of seaplanes between the two world wars. In this regard, it is worth to remember the research institutes of Langley Field (USA), Farnborough (England), Hamburg (Germany) and Guidonia (Italy). The last two were destroyed following the events of the last world war. At the beginning of the 1900s, the stepped hulls were used for seaplane skids. They had considerable takeoff and landing speeds, much higher than the speed of marine vehicles of that period. That is why many studies were carried out in USA and published by Society of Naval Architect and Marine Engine in 1911 on Transaction [9], where different flat plates, V-shaped plates as well as stepped plates were tested to analyze their performance. In the past the only hulls able to develop high speeds were the few operating in the marine and in racing. For this reason the study of the first of them was kept a secret and for the second ones the experiences of naval architects and boat yards were well protected.

Today it is easy to find low cost high powered engines, especially as boats are lighter and thanks to new building technologies with composite materials, it is easy to reach quite high speeds (high F_r numbers).

2.3. Hydrodynamic operational principle of a stepped hull

Stepped hulls are planing powerboats with V-shaped hulls. Theirs shapes can be both prismatic and with decreasing deadrise angle further aft [10]. Steps are discontinuities located at the hull bottom, with a V-shape where the vertex faces aft ward. At the waterline, steps taper out to a larger hole, in such a way air can be sucked down into the water through them. In most cases, steps run from the chine on both outboard sides, slightly aft down to the keel line. This will ensure that a larger amount of air can be sucked into the step for higher speeds, since the entry angle will be at a smaller angle to the oncoming airflow [10].

Steps have been recognized as efficient devices allowing to reduce resistance. In presence of more than one step, when a boat travels at high speeds, the air sucked through the outboard side apertures leads to the flow separation, like the water sliding out of the transom, thereby forming gas cavities. Considering the geometry and difference in angle of attack between the steps, the water reattaches to the hull towards the aft. In literature, many work focused on how the step allows to reduce the resistance. Among others, the theory reported in Savitsky and Morabito [11], can be validated through video-frames of planing stepped hulls from under the water. According to this theory, steps allow to reduce the resistance due to the geometrically lower wetted area, which is obtained by the water stream skipping the areas after the steps. As consequence, the gas cavities present low pressure due to the speed of the passing water. This low pressure sucks air down through the outboard side apertures, thereby causing “ventilation” of the steps [10]. Similarly to the first step, the same occurs at the other ones. When the water flow reattaches to the bottom hull, then a new stagnation pressure occurs. This latter is the pressure line, where most of the dynamic lifting force is located. A new stagnation pressure peak will occur at the next step as well. For a typical planing V-shaped hull without steps, there will be one only stagnation pressure line, where the hull intersects the water flow as shown in *Figure 2.2* [10]. Contrarily, for stepped hulls, several stagnation pressures create multiple lifting forces, thereby achieving a greater total lift force for a smaller wetted area.

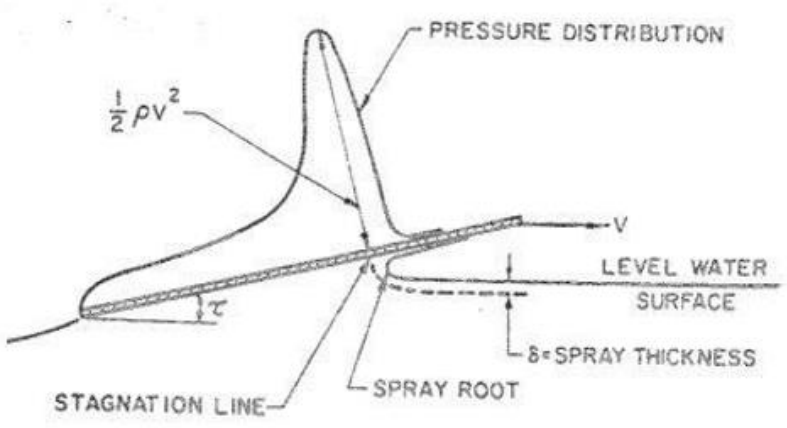

Figure 2. 2. The pressure distribution of a flat plate planing at the water surface, showing a peak at the stagnation line[10]

In case of two steps, the boat travels on three wetted areas, by balancing on three lifting forces related to the planing surfaces between the steps, as shown in *Figure 2.3*. The generated wetted areas are short and wide, and they look as the wings on an airplane. Moreover, they present a higher aspect ratio towards the oncoming flow as compared to a conventional V-shaped planing hull, which presents a larger wetted surface with lower aspect ratio. According to the wing theory, a higher aspect ratio allows to increase the lift force/drag ratio on a lifting surface [12].

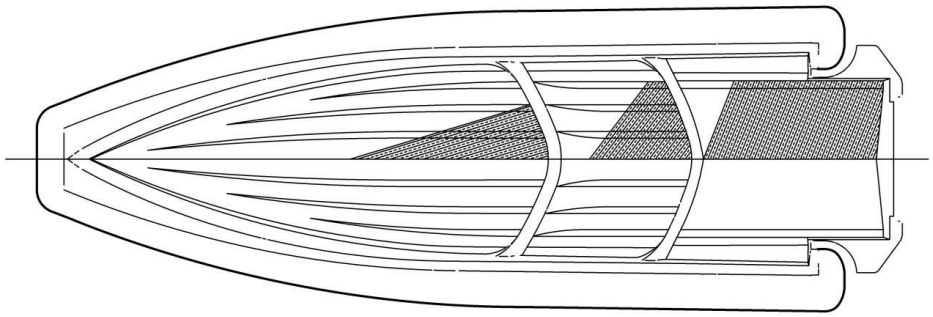

Figure 2. 3. Stepped hull, wetted surface at high speed

A stepped hull presents a lower wetted surface and a higher lift/drag ratio as compared to a traditional planing hull. In addition, it also has a more ideal trim angle to the oncoming flow, and makes the boat less sensitive to changes in the longitudinal center of gravity (LCG), hence the trim angle. However, for lower boat speeds before than the hump speed, the steps increase the resistance, due to the absence of the "ventilation" phenomenon.

2.4. Literature overview of hydrodynamic analysis of stepped hulls

Until now, hydrodynamics investigations of the planing hull, by virtue of different methodologies, mainly concentrated on the simple mono-hull, *i.e.*, without chine, and step. Among others, Savitsky [13] carried out comprehensively contribution to the understanding and modeling of planing crafts. He developed regression formulas based on prismatic hull form model tests to estimate the hydrodynamic forces acting on planing crafts. In 2007, Savitsky et al. investigated the effect of the whisker spray at the bow and its effect on the drag [14].

In the latest years, due to the market needs and, in order to gain more efficiency by the stepped hull, marine researchers have rigorously pursued this topic and much effort has been devoted to investigate their hydrodynamics by experimental test, as well as empirical and numerical methods.

Experimental Fluid Dynamics (EFD) as towing tank tests is more expensive and time consuming; a systematic series for this kind of hull is only available from experimental tests performed at the University of Southampton [15].

The empirical methods are those published in Savitsky and Morabito [11] and Svahn [16]. The first method experimentally studied the longitudinal surface wake profiles aft of prismatic hulls, the second method combined the equation of Savitsky and Morabito [11] with the equations of Savitsky's method for conventional planing hulls for power prediction of a stepped hull.

Numerical methods, as CFD tools, can be used to calculate the hydrodynamic performance of a stepped hull. In the last years, some studies have investigated this research field as Garland and Maki [17], which conducted a numerical study on two-dimensional stepped planing surface. Their results show that the lift-to-frictional-drag ratio varies very little with respect to the step location. Makasyeyev in [18] developed a solution method for two-dimensional mathematical problem of planing of the stepped air cavity hulls.

Matveev in [19] applied hydrodynamic discrete sources for two-dimensional modeling of stepped planing surfaces. The water surface deformations, wetted hull lengths, and pressure distribution are calculated at given hull attitude and Froude number (*Fr*). Matveev, in a successive study [20], presented the steady hydrodynamic modeling of semi-planing hulls with pressurized and open air cavities. This method is based on a linearized potential-flow theory for surface flows. Brizzolara and Federici in [21] developed an integrated semi-theoretical/numerical (CFD) method for the design of V-shaped stepped planing hulls that presented a considerable resistance reductions with respect to conventional hull forms. Lotfi in [22] used an unsteady RANS solver (ANSYS-

CFX) based on Volume of Fluid (VOF) approach for examining the characteristics and performance of a planing hull having one transverse step. A similar research was conducted by Bakhtiari [23].

3

EXPERIMENTAL TESTS

3.1. Background: the systematic series as an effective tool to predict the propulsion performances of vessels

The method of systematic series is recognized as an effective tool to predict the propulsion performances of vessels [24]. Nowadays, data for the calm water performance of systematic series of high speed planing craft are limited, and include Series 62 [25], Series 65 [26], and, more recently, a series based on the US Coast Guard 47ft Motor Lifeboat (MLB) [27]. In addition, there is also the NSS (Naples Systematic Series) consisting of five models, four of which are derived from the parent hull [28]. In this latter, the derived hulls are obtained by scaling depth and breadth by the same reduction factors, with the aim of maintaining the homothetic forms of all of the transversal sections. These transformations increase the ratio between the length and beam of the craft. The availability of seakeeping data for systematic series of high speed planing craft is even more limited. The most significant series is represented by the prismatic hull series tested by Fridsma [29, 30] and extended by Zarnick [31]. Other tests of high speed planing craft in waves include those were carried out by Rosen and Garme et al [32 - 34]. The models tested in these calm water resistance and seakeeping tests are either prismatic forms, or are not representative of modern high speed stepped hull forms. Moreover, the hard chine hulls have an intrinsic limit given by their geometric shape; indeed the higher the speed, the higher also the vessel resistance compared with a simple chine stepped hull. Instability and dynamic phenomena occur more easily.

To overcome the above limits, another series of stepped hull forms was designed by Tauton et al in [15]. In detail, two hulls were derived from the parent hull with one and two steps, respectively. The performances of the models were investigated by varying *L/B* and *B/T* values.

3.2. Design issues (parent hull)

The craft for this investigation is a Rigid Inflatable Boat (RIB) Mito 31 by MV Marine S.r.l. with two outboard engines. *Figure 3.1* shows some details and the main particulars of the hull body.

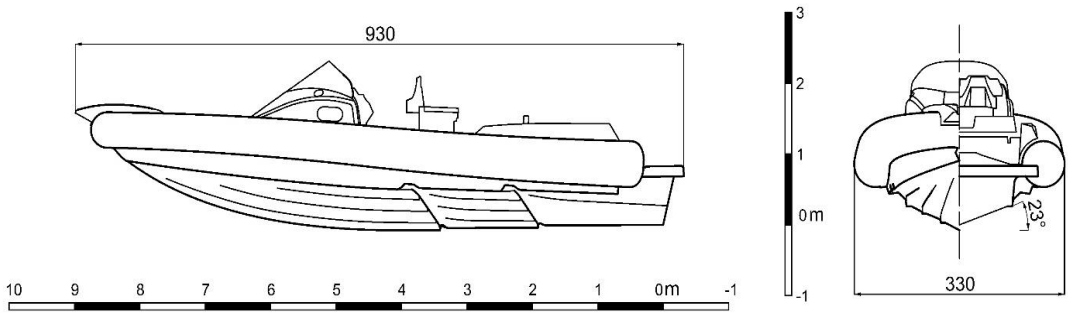

Figure 3. 1. Dimension and characteristics of RIB Mito 31 by MV Marine

In *Table 3.1*, the RIB geometrical details are reported. Some of the design data mentioned in the table below are taken as input for the analyzed systematic stepped hull series. These design data are derived from a detailed analysis of the relevant works in literature, as discussed in the following.

Step Number (NS) is 2 because this hulls have a high *L/B* ratio. In accordance with Peters in [35] and Akers in [36], single or twin step decisions depend on the length-to-beam ratio, and speed. The low aspect ratio lifting surface of a boat with narrow beam requires two steps for lift.

Step Height (HS) is 40 mm, but it is a parameter difficult to define since generally this characteristic is different for every hull and is based on the angle of attack. Peters in [35] defines a minimum and maximum value for Step Height (31,8 mm, 65,5 mm). Akers in [36] in accordance with the author Norman Skene specifies that high steps are not necessary and that experience shows steps as low as 16 mm could be effective. The real issue with high speed steps is that an “S” curve should be put in the buttock line behind the step to control the angle of attack of next step.

Table 3. 1 Dimensions and geometric characteristics of RIB Mito 31 by MV Marine

Hull Type	**Hard chine, stepped hull**
Length Overall (m)	10
L/B ratio	5
Chine Beam (m)	2
Deadrise Angle (°)	23
Step number	2
Step height (mm)	40
Maximum Speed (knots)	50
Propulsion type	Outboard engine
Longitudinal Step Position (LSP) (cm)	step 1 = 184 step 2 = 337

As regards the Longitudinal Step Position (LSP), there are several solutions in literature. Firstly, in accordance with Acampora in [37], Akers in [36] and Peters in [35], a solution is based on the concept that it is necessary to have a middle surface close to the LCG, with the forward and aft portions of the hull stabilizing the craft longitudinally. This solution has a problem: if the steps are too close to each other, the water attaching to the second step is contaminated by the aerated low-density water from the first step. Secondly, Clement and Pope [39] define a procedure to obtain LSP as a function of hull geometric parameters. However, the step is always further forward than the LCG. The third solution, in accordance with Clement in [39], is based on the usage of a design approach for a stepped hull similar to a design of a hydrofoil boat or an airplane. Therefore, this approach is able to find the optimum configuration of a lifting surface to obtain a maximum lift-drag ratio, but, as consequence, the CG (Center of Gravity) is closed in a forward lifting surface. On the other hand, the LCG is near the fore step but further forward than it. When the LCG is put so that weight is balanced across the steps, only a small change in the relative locations of LCG and center of pressure will change the boat from stable to unstable. Referring to the static trim angle at rest τ_0, as shown in [40], a boat trim by stern presents a higher resistance at low Froude numbers, while at high Froude numbers resistance will be lower.

3.3. Testing methodology

Power prediction through the towing tank tests is carried out at the Department of Industrial Engineering section of Naval Architecture and Marine Engineering of the University Federico II of Naples. Dimensions of the basin are defined in the following:

- Length: 137.5 m;
- Width: 9 m;
- Deep: 4.25 m.

The tow carriage is able to develop a maximum speed of 10 m/s with a maximum acceleration of 1 m/s^2. The test is based on Froude methodology for effective power calculation; the scale model is chosen by considering the maximum velocity of the carriage.

The first test series are carried out with R47 by Kempf & Remmers equipment which constrains the model by system forces shown in *Figure 3.2*. The thrust *T*, as the shot force which occurs in the hinge, is located in a higher position compared to the center of gravity, and higher with respect to hydrodynamics center. The R47 instrumental gravity center is located at the same longitudinal abscissa as the buoyancy centre. Moreover, several tests are also carried out to reduce the instruments weights by a tackle. However, the results are found to be poor, since the values of τ angle and running resistance obtained by model experiments result to be very different as compared to sea trial results.

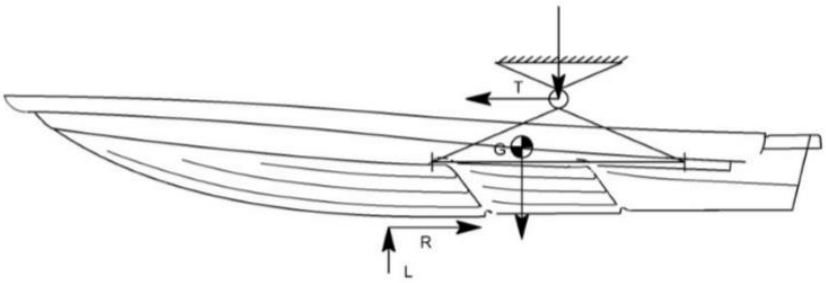

Figure 3. 2. R47 system forces

3.3.1 Experimental analysis

Towing tank tests are useful for development and consequent spread of stepped hulls forms. In the analyzed case, towing tank tests are carried out with a scale model of a standard RIB Mito 31 built by MVmarine, with different testing methodologies. The small model dimension makes the

experimentation and towing tank-sea correlation hard, because of scale effect problems and high ship speed (50 Knots, Fr equal to 3,0 and Fr_{∇} (Volumetric Froude number) equal to 7,0). However, a particular test system is setup, which reproduces in the towing tank the same dynamic condition as occurring in the sea. This new setup is established to reproduce in the towing tank test the same angles measured in sea trial, since the trim angle is an essential characteristic for the dynamical similarity between model and ship flows. Froude methodology is used to attain speed and resistance measurements, up to a speed of 50 knots. The angle τ is a direct consequence of the forces system acting on the running hull and influencing the relationship between lift and drug *L/D*, dynamic stability, purposing and sea keeping.

3.3.2. Sea trial tests for measurement of the dynamic trim angle

The necessity to start from sea trial tests is due to the issues related to the towing tank ones with the R47 Kempf & Remmers instruments, which are generally used for planing hulls. The tests show that the hull model was unable to lift itself from the water at high speed, with high resistance value. Contrarily, the full scale RIB Mito 31 has a different behavior, thereby providing the suggestion to carry out a series of sea trial tests on Mito 31 RIB.

In sea trial tests, an inertial platform has been installed to measure Euler angle and acceleration, as shown in *Figure 3.3*.

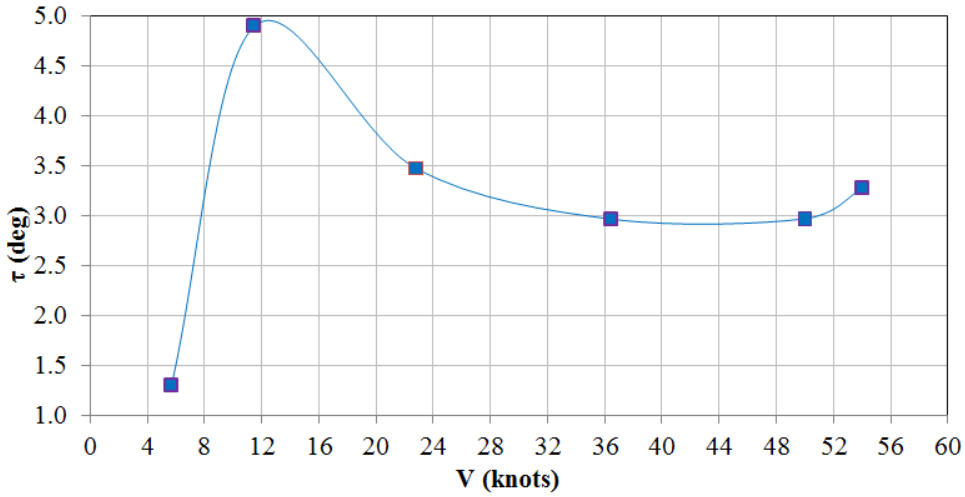

Figure 3. 3 Sea trial test τ vs speed curve

The fuel consumption and rpm engines have been acquired for each speed value as shown in *Figure 3.4*, by using onboard instruments.

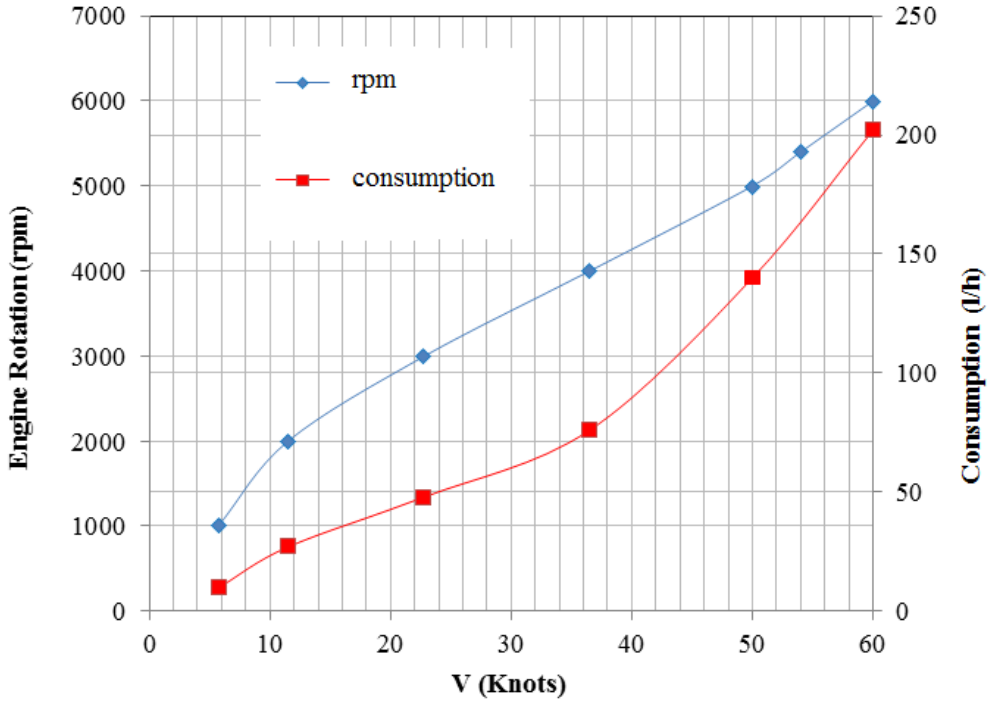

Figure 3. 4 Sea trial test, speed, rpm, fuel consumption curve

3.3.3 Trim Engine effect

All outboard engines are equipped with power trim and tilt systems, with the aim to direct thrust in the center plane. This allows to attain a variation in the moment that the engine transfers on the transom. The effects of this regulation at maximum engine rotation allow the gaining of 4 knots at maximum speed and 0.5° of dynamic trim angle τ influencing hump speed. Accordingly, to reduce the number of variables, all sea trial tests have been performed with RIB ships and the thrust direction in a horizontal position in static condition, with zero trim and zero thrust angle (*Figure 3.5*, T vector parallel to WL).

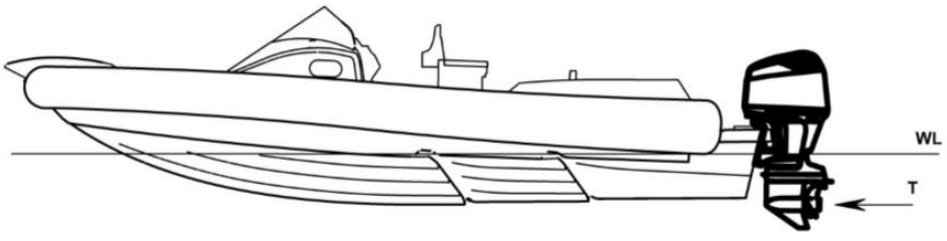

Figure 3. 5 Outboard engine thrust

3.3.4 Down Thrust Methodology

The analyzed true forces system are shown in *Figure 3.6*, and a similar system has been also reproduced in the towing tank test to obtain the same τ angle.

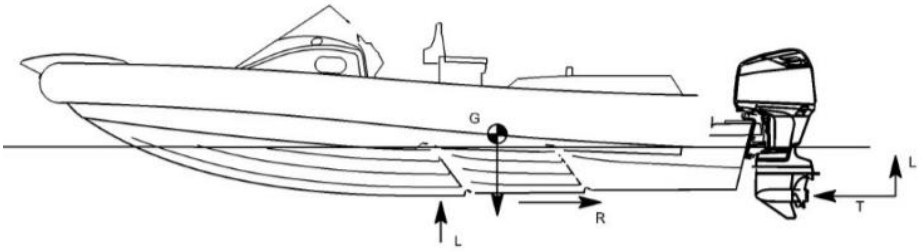

Figure 3. 6 Analyzed true forces system

To reproduce at best the system forces, the real RIB has been considered. The two outboards engines have been constrained to the transom through four bolts for each engine. Two of them are located in highest bracket zone and the other two ones are located in the lowest bracket zone (*Figure 3.7*).

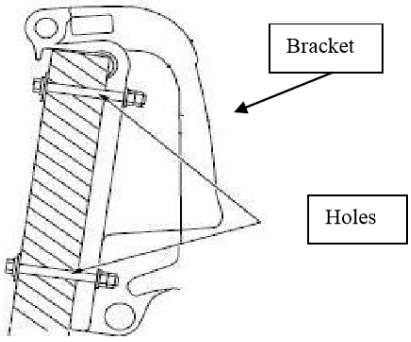

Figure 3. 7 Engine bracket

When the engine goes forward, it transfers the thrust *T* to the transom through the force *F1*, which is applied in the lowest brackets area and the thrust moment M_T, as regards the lowest brackets area through traction force *F2*, which is applied in the highest part of the bracket (*Figure 3.8*). Consequently, the system forces engine/RIB is similar to a beam supported by a pin and a roller (*Figure 3.9*). In fact, the propeller thrust is transmitted to stern through a moment generated by the thrust vector with respect to the lowest brackets area, whereas the highest holes are in contrast (*Figure 3.10*). This latter consideration is based on the location of the model point thrust. In fact, the thrust to the transom is transmitted entirely from the lowest bracket area. In a horizontal

position in a static trim angle at rest τ_0 equal to zero, the towing tank thrust force is applied in the point *P* intersection between the engine thrust direction and the keel line at the bow (*Figure 3.11*).

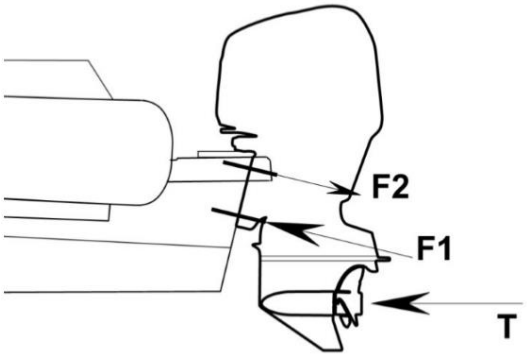

Figure 3. 8 Engine forces

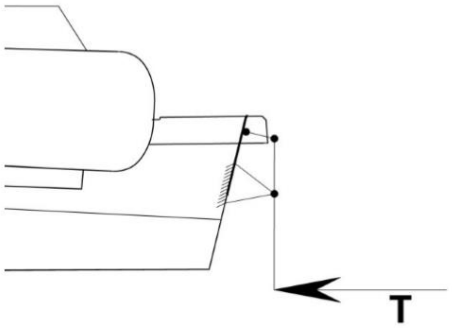

Figure 3. 9 Engine thrust 1

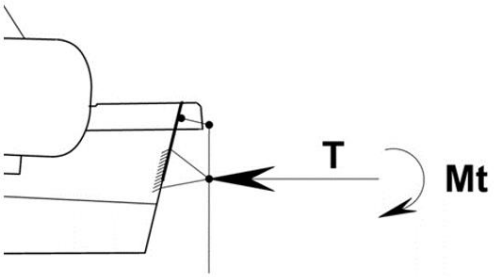

Figure 3. 10. Engine thrust 2.

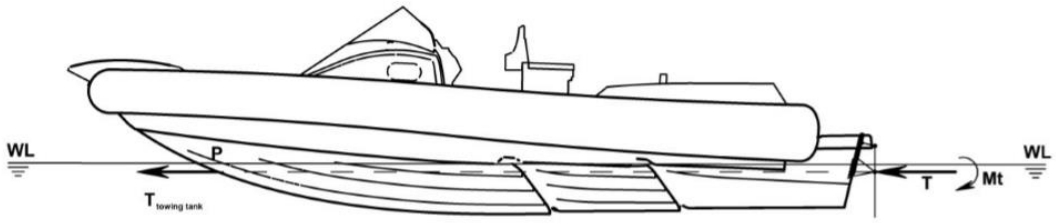

Figure 3. 11 Towing tank thrust force

This is defined the "Down Thrust" (DT) methodology, which does not consider the M_T moment effect, which could generate an increasing τ angle on the RIB. In the analysis, there is a fixed orthogonal reference axis with origin in the aft perpendicular. The X-axis is parallel to the base line and positive toward the bow, the Z-axis is orthogonal to the still water plane and positive upwards, and the Y-axis is positive towards the RIB right side. With R47 instruments, the model has just 3 degrees of freedom, moving along X- and Y-axis and rotating around Y-axis. In the Down Thrust methodology, the model has all the six degrees of freedom. To avoid instability phenomena, the model has been realized with two guide model masts, with the first one located in the bow, and the second one at stern, which engage in two forks. (*Figure 3.12*).

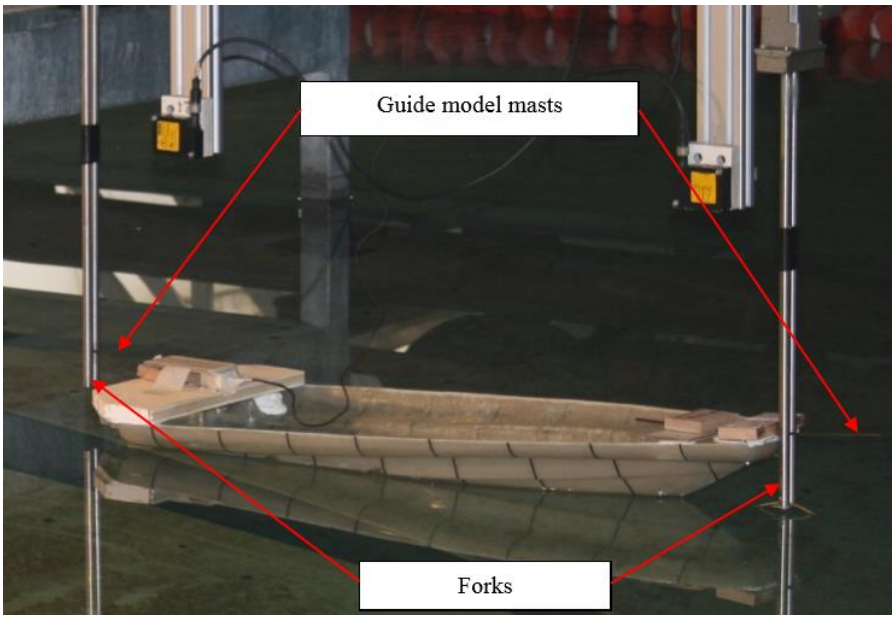

Figure 3. 12 Towing tank DT Test, stepped hull, Model Basin photo

Down Thrust allows the model hull to move along the X- and Z-axis but not along the Y-axis, and allows τ for rotation around the Y- and X-axis but not around Z-axis. Consequently only the yaw and drift motion are constrained. This solution has been reached releasing the model from each instrument, because with such a small model displacement (3.13 kg), the RIB model becomes

sensitive to all external forces. All the towing tank tests have been carried out with a zero trim in static conditions. The towing tank and sea trial test results are compared for τ and total resistance, R_{TM}, in *Figure 3.13* and *Figure 3.14*, respectively.

Figure 3.13 shows the τ angle versus the speed. It can be noted that τ - V curve obtained by Down Thrust test shows the same trend as the sea trial test curve. Contrarily, the R47 instrument has registered the lowest τ values because it produces a bow pitch moment transferred to the small hull model, due to the highest thrust respect to the hydrodynamic resistance center. For speeds in the range between 30 and 50 knots, the difference between the τ_M angle measured in towing tank test with respect to the sea trial test τ_S angle is represented by an average of 0.3°.

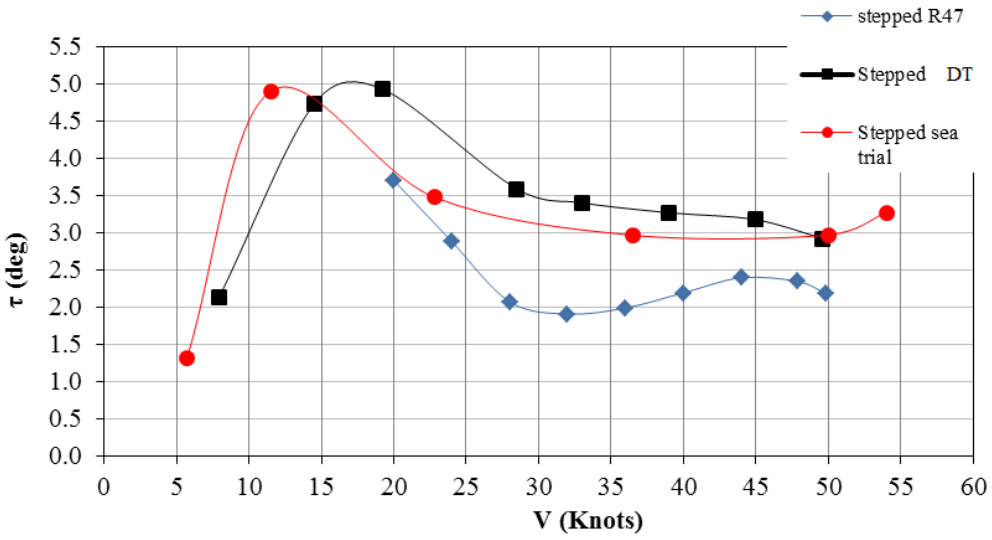

Figure 3. 13 Sea trial and towing tank tests, τ vs. V curve

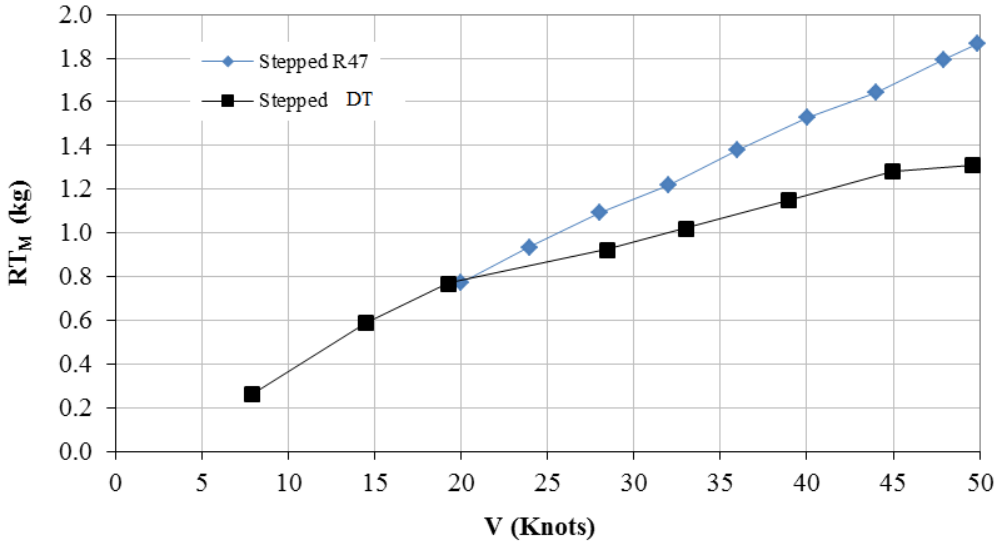

Figure 3. 14 Towing tank tests compare results, R_{TM} measure with Down Thrust and R47

With Down Thrust Methodology, the experimental measure of the resistance and trim angle can be considered reliable. This methodology has been used to measure R_{TM} in all the towing tank tests. The effective power, P_E, has been calculated according to the Froude method (ITTC '57).

3.4 Limits due to the experimental layout

All the limits of the experimental layout are verified for each test. Considering the towing length, the distance for the carriage acceleration, the minimum time for data acquisition and the distance for deceleration, the model maximum speed limit is 8.05 m/s.

The test has been performed by using the Froude methodology, and the model scale ratio has been considered according to the maximum ship and the maximum carriage velocities. It follows that:

$$V_S / V_M = \sqrt{\lambda} \tag{3.1}$$

where, in accordance with data design, the maximum ship speed, V_S, is about 50.0 knots (25.72 m/s) and maximum towing tank carriage speed, V_M, is 8.05 m/s. Therefore, the model scale, λ, is:

$$\lambda = \left(V_S / V_M\right)^2 = 10.24 \tag{3.2}$$

In accordance with design data, assuming a model scale ratio as 1:10, the model displacement is calculated as:

$$\Delta_S / \Delta_M = \frac{\rho_S}{\rho_M} \cdot \lambda^3 = 31392N / \Delta_M \Rightarrow \Delta_M = 31.39N \tag{3.3}$$

where ρ_s is the sea water density and ρ_M is the water density of the towing tank. The model for towing tank test has been designed in 3D CAD and built with composite materials. The model has a transparent bottom realized only with isophthalic resin to provide a full view of the water flow under the hull. The side of the model has been realized in fiber reinforced plastic (FRP), and the model surface has been realized with high-gloss neopentilic gelcoat transparent.

The model has been manufactured in hand-made layup through a mold. The mold has been designed in 3D CAD/CAM and has been built in FRP through the following step:

- milling of high-density PVC foam with CNC five-axis machine with a rough finish to build a “model for mold”;
- covered with a spray polyester pastes;
- milling the foam covered with the polyester pastes with CNC machine five-axis with a good finish;
- spraying the polyester gelcoat;
- tooling in hand-made, polish and wax;
- spraying the polyester gelcoat for mold;
- laminating the FRP (glass fiber and isophthalic resin) in hand-made layup.

In accordance to [41], the model hull tolerances for breadth, drought, and length are ±0.5 mm. The manufacturing tolerance for length is less than 0.05%, and special attention has been paid into the shaping of chines and step.

3.5 Laboratory instrumentation and measurements

The carriage has been instrumented on board with a sensor network and a data-acquisition (DAQ) device. The sensors used in these tests are the encoder for speed carriage, load cell for resistance measure, balance for model and ballast weights, thermometer for water temperature, accelerometer for trim, and laser for sinkage. The thermometer used during the tests allows a range from -5.0 °C to 40 °C, with and accuracy of 0.1 °C and resolution of 0.1 °C.

The speed of the carriage has been measured by using a high-quality encoder and a counter/timing card. The high-quality of the encoder is due to the fact that the encoder wheel rolls without slithering. The encoder is not fixed to the any wheel drive of carriage, and it gives 1000 pulses per one round (1 pulse for each mm). The encoder sensor has an accuracy of 1.0 mm/m and a resolution of 1.0 mm. The period between two pulses has been measured by a counter/timing card at 32 bits with a clock of 80 MHz. The card has a range from 1.25×10^{-8} s to 53.69 s; the clock at 80 MHz has an accuracy of $\pm4.0\times10^{-3}$ MHz and a resolution of 1.25×10^{-8} s.

The resistance measure has been performed by a high-quality load cell (precision class 0.003) and conditioning-acquisition card. The load cell has a range up to 50 N, an accuracy of 0.003%, and

a resolution of 0.005 N. The conditioning-acquisition card has a software programmed range of 50 N, accuracy of 0.08%, 16-bit resolution, and sampling rate up to 200 kSamples/s. For these measurements, the row data have been oversampled at a rate of 10 kSamples/s, and compressed at a rate of 500 Samples/s for further reduction of the noise.

Running trim measure has been performed by an accelerometer and a conditioning-acquisition card. With running model hull, in stationary conditions, the accelerometer measures the *g* components with respect to a reference system, which is in-built to the model hull. Based on this measure, it is possible to evaluate the trim. The accelerometer sensor has a range of 40 m/s^2, accuracy of ±0.1%, and resolution virtually infinite. The conditioning-acquisition card has a software programmed range of 40 m/s^2, accuracy of 0.1%, and 16-bit resolution.

Sinkage has been measured by two high-quality laser sensors and a conditioning-acquisition card. The two lasers have a range from 0.2 to 1 m, accuracy of 0.5 mm, and resolution of 0.05 mm. These laser devices have been placed perpendicularly with respect to the water surface, at two positions, one at fore section and second at aft section. The conditioning-acquisition card has a software programmed range up to 1 m, accuracy 0.1%, and 16-bit resolution.

The weight and ballast of the model have been measured with a balance with a range of 600 N, accuracy of ±0.1 N, and resolution of 0.1 N.

Wetted surface measures are possible through a video camera placed on towing carriage, in perpendicular position with respect to the model's center of gravity. The video camera with 50 mm lens recorded each test from the start to the end. In such a way, it has been possible reconstruct the dynamic of the vortex phenomena near the step.

3.6 Experimental results

The study of the factors involved in the experimental tests is a crucial task and requires intensive knowledge transfer. The first brainstorm step involves all the listing factors that, according to different technological points of view and competencies, come out during team discussion.

As regards the control factors in the screening experimental phase, the following have been selected: numbers of the steps (NS), step height (HS), longitudinal position of the step (LSP).

A new systematic series of eight hull models derived by the stepped hull Mito 31 (described in the previous sections) has been developed. In detail, during the planning of the scale models of the

eight hulls, the step height has been set to 2 and 6 mm on model scale, which means 20-60 mm in ship scale, as these are considered the limit values suggested by Peters in [35] e by Akers in [36]. Referring to the longitudinal step position, inspiration has been taken from the two planning ideas suggested by Clement & Pope in [38] and Clement in [39], then the hulls designed with a value of longitudinal step position equal to 0 m have a step corresponding exactly with the center of gravity as in [39], whereas the ones with a value of the longitudinal step position equal to 1.4 m have the step on forward of the centre of gravity as in [38].

To perform the experimental tests, the hull models have been built with different geometries according to the change of the control factors. In *Table 3.2*, the main characteristics of the derived hulls are summarized. Both the longitudinal step position and the longitudinal centre of buoyancy (LCB) are measured from the hull transom.

Table 3. 2 Main characteristics of the eight hull models derived from the parent hull Mito 31.

Hull ID number	**Step Number**	**Step Height [mm]**	**LSP [mm]**	**LCB [mm]**
Mito 31 model (parent hull)	2	3	step 1 = 184 step 2 = 337	299
C02_1_20_0	1	2	step 1 = 300	277
C03_1_60_0	1	6	step 1 = 300	291
C04_1_20_1	1	2	step 1 = 440	276
C05_1_60_1	1	6	step 1 = 440	286
C06_2_20_0	2	2	step 1 = 147 step 2 = 300	283
C07_2_60_0	2	6	step 1 = 149 step 2 = 302	307
C08_2_20_1	2	2	step 1 = 288 step 2 = 441	282
C09_2_60_1	2	6	step 1 = 290 step 2 = 443	310

The results of calm water resistance tests and trim angle are presented in the following. The non-dimensional total resistance of the analyzed systematic series is shown in *Figure 3.15*. The resistance curves shown are typical of planing hulls. In detail, for Fr_∇ values in the range 1 – 2, a similar trend can be noted for all the analyzed hulls. This is due to the motion regime occurring, which is the displacement one. As Fr_∇ increases, for values in the range 2 – 4, the resistance trends is different for the analyzed hulls. In particular for Fr_∇ values higher than 2, the C02, C03, C04, C05, C08, C09 hulls reach the hump speed, thereby resulting in a lower slope, as compared with the previous range analyzed. The hump speed phenomenon occurs for Fr_∇ values higher than 2.5 for the parent hull, as well as for C06 and C07 hulls, with higher evidence for this latter.

Finally, for Fr_∇ values higher than 4, resistance increase again, except for the parent hull.

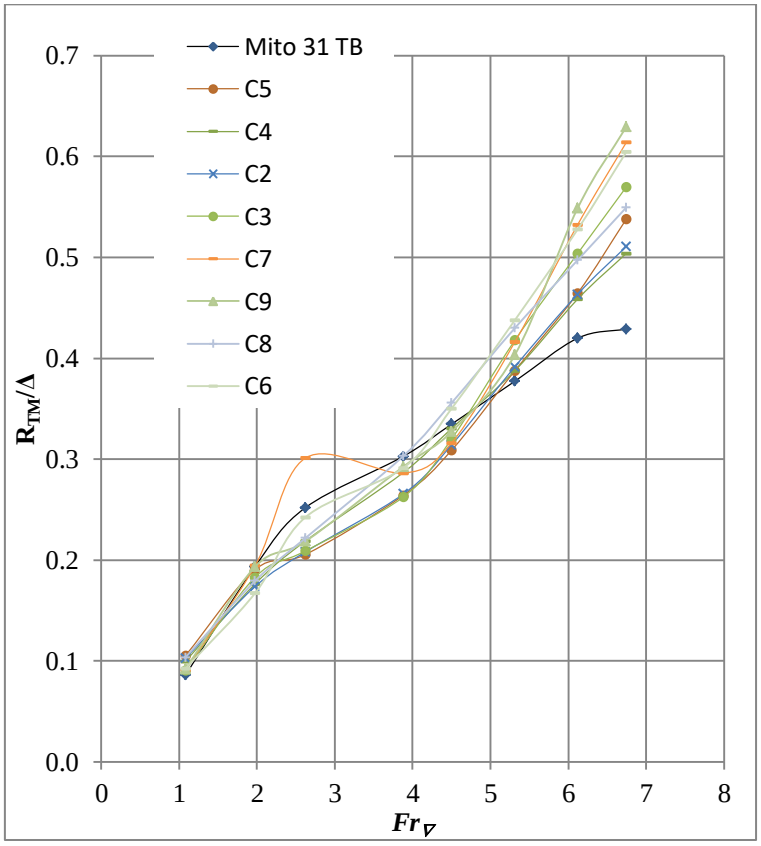

Figure 3. 15 Non-dimensional total resistance of the new systematic series

Table 3.3 shows the detailed experimental results of the non-dimensional total resistance of the systematic series analyzed.

Table 3. 3 Non-dimensional total resistance R_{TM}/Δ of the new systematic series

Fr_{∇}	Mito 31	C2	C3	C4	C5	C6	C7	C8	C9
1.086	0.086	0.103	0.091	0.100	0.105	0.092	0.091	0.104	0.092
1.984	0.194	0.174	0.183	0.176	0.190	0.167	0.194	0.179	0.193
2.636	0.252	0.208	0.209	0.219	0.206	0.243	0.301	0.222	0.219
3.899	0.303	0.265	0.263	0.287	0.264	0.291	0.286	0.303	0.293
4.519	0.335	0.314	0.320	0.330	0.309	0.350	0.316	0.356	0.327
5.337	0.377	0.392	0.418	0.388	0.388	0.438	0.416	0.430	0.403
6.146	0.420	0.463	0.504	0.459	0.464	0.528	0.532	0.497	0.549
6.777	0.429	0.511	0.570	0.504	0.538	0.605	0.614	0.550	0.630

Figure 3.16 shows the trim angle curves of the systematic series analyzed. As well as for resistance curves, also for trim angle, the trends are typical of planing hulls. Before the hump speed occurs, trim angles strongly increases for all the analyzed hulls, reaching the maximum at the hump speed. Then, after the hump speed, in the planing phase, trim angle strongly reduces, until arriving at a sub-horizontal trend for Fr_{∇} values higher than 4, except for the C05 model.

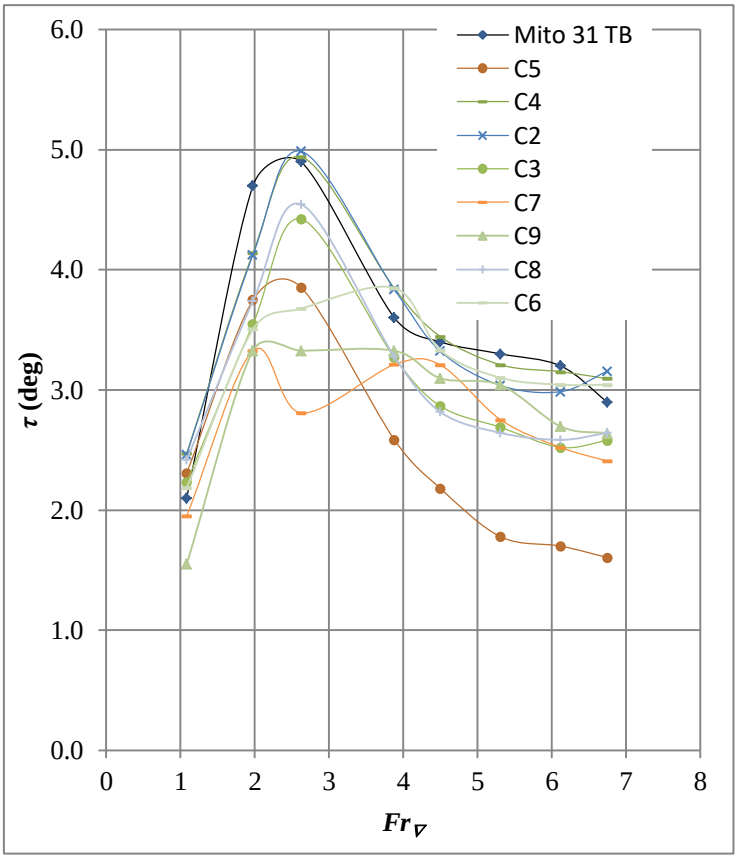

Figure 3. 16 Trim angle of the new systematic series

Table 3.4 shows the detailed experimental results of the dynamic trim angle of the systematic series analyzed.

Table 3. 4 Dynamic trim angle (deg) of the new systematic series

Fr_∇	Mito 31	C2	C3	C4	C5	C6	C7	C8	C9
1.086	2.1	2.46	2.23	2.47	2.30	2.18	1.95	2.42	1.55
1.984	4.7	4.13	3.55	4.14	3.75	3.50	3.33	3.74	3.33
2.636	4.9	4.99	4.42	4.94	3.85	3.68	2.81	4.54	3.33
3.898	3.6	3.84	3.27	3.84	2.58	3.85	3.21	3.28	3.33
4.519	3.4	3.32	2.87	3.44	2.18	3.33	3.21	2.82	3.10
5.337	3.3	3.04	2.69	3.21	1.78	3.10	2.75	2.64	3.04
6.146	3.2	2.99	2.52	3.15	2.93	3.04	2.52	2.58	2.70
6.777	2.9	3.16	2.58	3.09	1.61	3.04	2.41	2.64	2.64

Table 3. 5 Non-dimensional dynamic sinkage $Z/\nabla^{1/3}$ of the new systematic series

Fr_{∇}	Mito 31	*C2*	C3	C4	C5	C6	C7	C8	C9
1.086	N/A	-0.051	-0.081	-0.048	N/A	-0.111	-0.082	-0.059	N/A
1.984	N/A	0.037	0.011	0.021	N/A	-0.068	-0.005	-0.002	N/A
2.636	N/A	0.101	0.048	0.143	N/A	-0.059	0.045	0.066	N/A
3.898	N/A	0.135	0.086	0.169	N/A	0.071	0.153	0.146	N/A
4.519	N/A	0.248	0.142	0.198	N/A	0.047	0.130	N/A	N/A
5.337	N/A	0.165	0.149	0.186	N/A	0.104	0.151	0.139	N/A
6.146	N/A	0.196	0.154	0.189	N/A	0.050	0.150	0.149	N/A
6.777	N/A	0.212	0.184	0.220	N/A	N/A	0.157	0.196	N/A

As mentioned at beginning of this thesis, for the study of vortical flow phenomena at the bottom of the step, only one model, *i.e.*, C03 has been chosen. This model hull has one transverse step, located in the same longitudinal position of center of gravity with a forward shape, as shown in *Figure 3.15*.

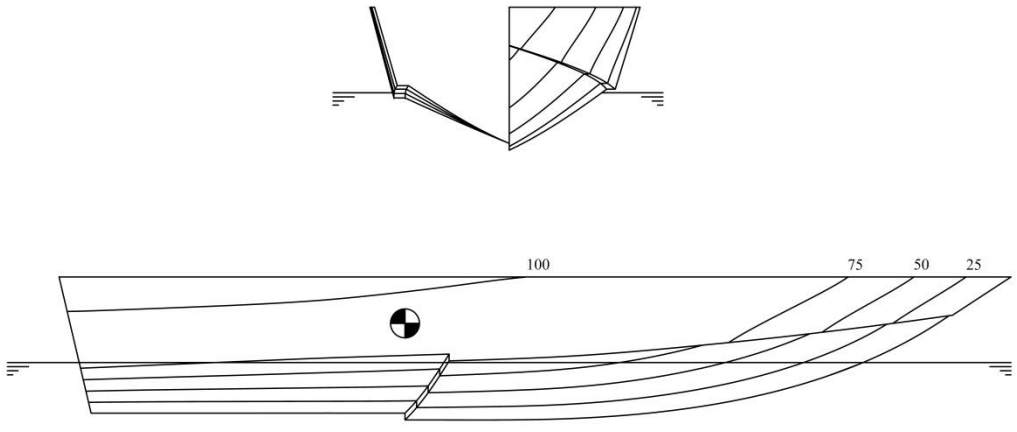

Figure 3. 17. C03 model body plan (transversal section every 0.1 m) and profile (buttock line every 0.025 m)

The model has the same main dimensions: keel line, chine line, deadrise angle, displacement, LCG, step shape, step angle, and keel line of RIB Mito 31, with 1:10 scale.

The details of the hull model are reported in *Table 3.4.*

Table 3. 6 Main dimensions of the C03 model hull

Length over all L_{OA} [m]	0.935
Breadth max B_{MAX} [m]	0.335
Deadrise angle at transom [°]	23
Step height [mm]	6.0
Displacement [N]	30.705
LCG [% *L*]	33
Model scale	1:10

The results of calm water resistance tests are presented in *Figure 3.18, Figure 3.19, Figure 3.20, Figure 3.21* and *Table 3.5*. All values are plotted with reference to the volumetric Froude number $\left(Fr_{\nabla}\right)$. In particular:

- the non-dimensional total resistance $\left(R_{TM}/\Delta\right)$ is shown in *Figure 3.18*;
- the dynamic trim angle (τ) is shown in *Figure 3.19*;
- the non-dimensional dynamic sinkage $\left(Z/\nabla^{1/3}\right)$ is shown in *Figure 3.20*;
- the non-dimensional dynamic wetted surface $\left(S/\nabla^{2/3}\right)$ is shown in *Figure 3.21*.

These results are typical of a stepped hull. In particular, as expected, the trim angles are quite low for higher Froude numbers and change slightly with Fr_{∇}.

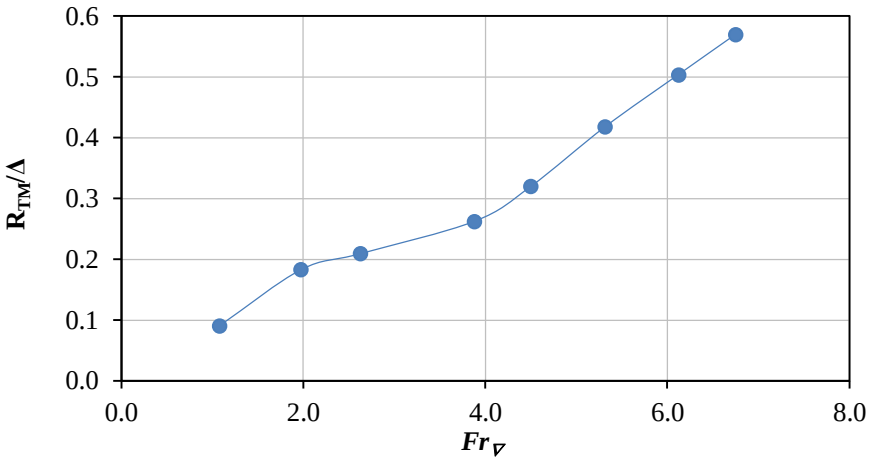

Figure 3. 18 Non-dimensional total resistance C03

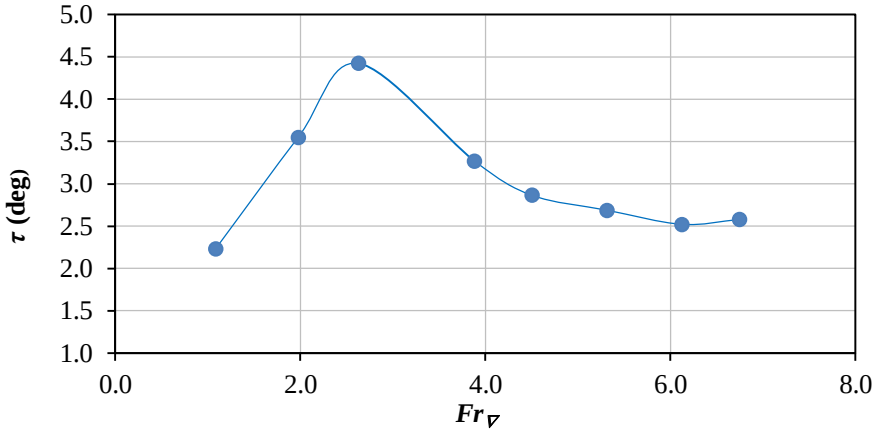

Figure 3. 19. Trim angle C03

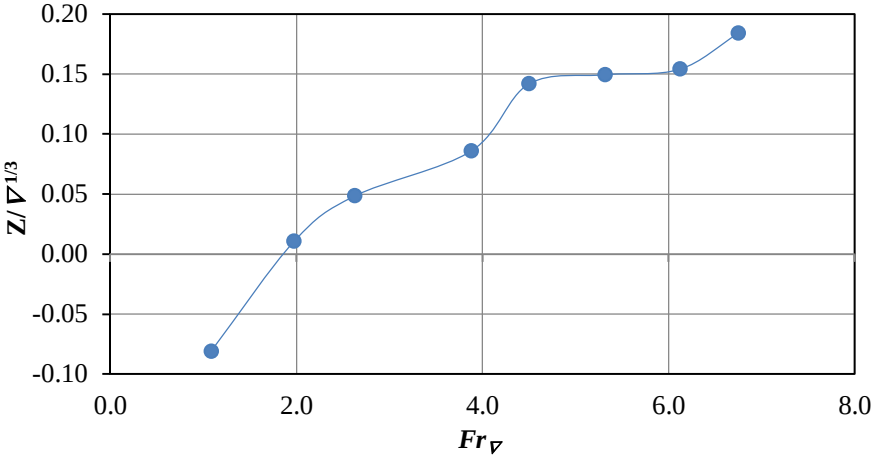

Figure 3. 20. Non-dimensional dynamic sinkage C03

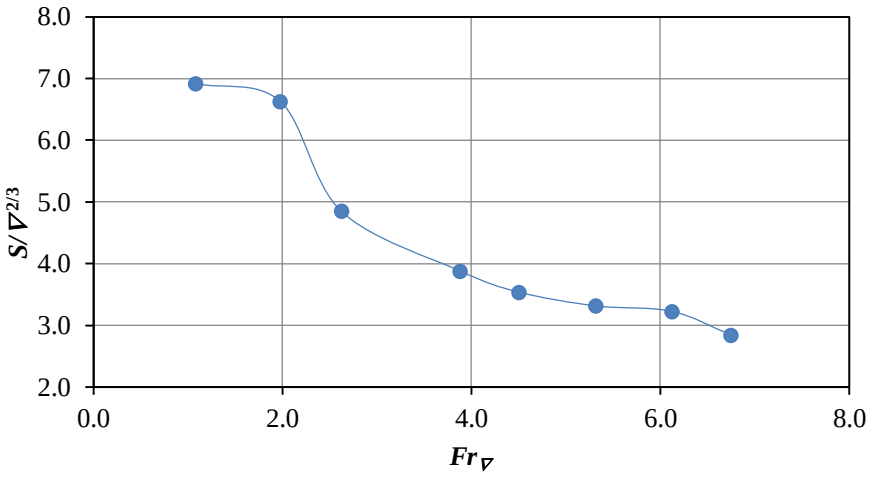

Figure 3. 21 Non-dimensional dynamic wetted surface C03

Table 3. 7 Main experimental results

Fr_{∇}	R_{TM}/Δ	τ	$Z/\nabla^{1/3}$	$S/\nabla^{2/3}$
1.984	0.183	3.55	0.011	6.631
3.898	0.263	3.27	0.086	3.881
5.337	0.418	2.69	0.149	3.316
6.777	0.570	2.58	0.184	2.845

A significant outcome of the present experimental investigation is given by the observation of some clear vortical patterns that develop into the unwetted aft body area behind the step, and partly continue downstream in the water wake. The vortex in the unwetted aft body area appears for towing speeds greater than 2.36 m/s ($Fr_{\nabla} > 1.97$) These phenomena are visible thanks to the transparent bottom of the hull model, which was expressly designed. Some pictures of the flow patterns are shown in *Figure 3.22* , and *Figure 3.23* (upper part). Additionally, a video recording of a towing tank run has been released in the public domain in L. Vitiello [42]; it documents the time development of well visible vortex structures under the hull, as seen from an observer looking from the top and through the transparent bottom.

Uncertainty Analysis (UA) in experimental fluid dynamics (EFD) has been also performed according to ITTC [43] as reported in Appendix A.

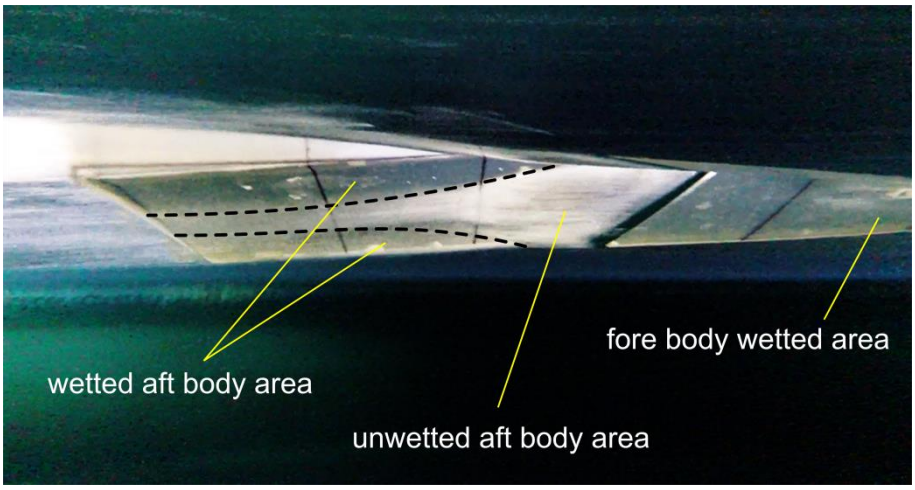

Figure 3. 22 Experimental wetted surface right-side view at Fr_{∇} =3.898

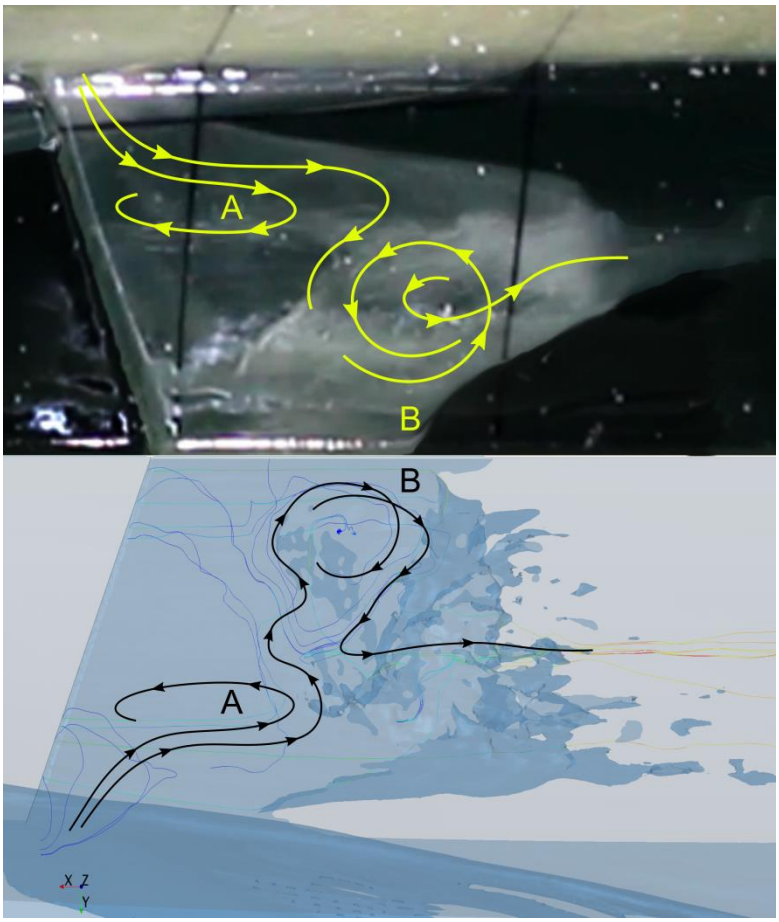

Figure 3. 23 LES simulation at Fr_{∇} =3.898; flow patterns in the unwetted aft body area, top view

4

NUMERICAL METHODS

In this chapter, the main aspects of the mathematical models of the CFD codes are described, focusing on the commercial code CD-Adapco Star CCM+, which is used to represent the physical model typically occurring in hydrodynamics problems, focusing on the resistance test simulation of planing and stepped hulls.

After the description of the governing equations of the flow solver, the main aspects of the spatial and time discretization, the rigid body motion solver, the coupling with the flow simulation, and the dynamic mesh are treated in detail.

4.1 Governing Equations

The governing equations for the fluid flow are the continuity and Navier–Stokes (NS) ones. Flows in the laminar regime are completely described by these set of equations and, for simple cases, the continuity and NS equations can be solved analytically. More complex flows can be tackled numerically with CFD techniques such as the Finite Volume Method (FVM) without additional approximations.

However, in ship hydrodynamic field, many flows are turbulent. Fluid engineers need access to viable tools capable to represent the effect of turbulence. Turbulence causes the appearance in the flow of eddies with a wide range of length and time scales interacting in a dynamically complex way. There are many numerical methods to capture the effects due to the turbulence. The methods can be grouped into the following three categories:

- Turbulence models for RANS equations (effect of turbulence on mean flow properties);
- Large Eddy Simulation (LES) (intermediate form of turbulence calculations);
- Direct Navier Stokes (DNS) (compute the mean flow and all turbulent velocity fluctuations).

For most of engineering purposes, it is unnecessary to resolve the details of the turbulent fluctuations. CFD users are almost always satisfied with information about time-averaged properties of the flow (*e.g.*, mean velocities, mean pressure, etc.). Therefore, the vast majority of the turbulent flow computation in the ship hydrodynamic field has been and will continue in the next years to be carried out with procedures based on the RANS equations.

In the RANS method, the solver is applied to the following group of equations which express the mass continuity and the NS with a Reynolds time-average approach. The RANS equations can be expressed, in the typical hydrodynamic applications, as an incompressible flow as follows:

$$\begin{cases} \nabla \cdot V = 0 \\ \rho \dfrac{dV}{dt} = -\nabla \cdot P + \mu \cdot \Delta V + \nabla \cdot T_{\mathrm{Re}} + S_M \end{cases} \tag{4.1}$$

where V is the Reynolds averaged flow velocity vector, P is the average pressure field, μ is the dynamic viscosity, T_{Re} is the tensor of Reynolds stresses, and S_M is the vector of the momentum sources.

The component of T_{Re} is computed by using the selected turbulence model, in agreement with the Boussinesq hypothesis, *i.e*:

$$\tau_{ij}^{\mathrm{Re}} = \mu_t \left(\frac{\partial V_i}{\partial x_j} + \frac{\partial V_j}{\partial x_i} \right) - \frac{2}{3} \rho k \delta_{ij} \tag{4.2}$$

where μ_t is the turbulent viscosity, and k is the turbulent kinetic energy. There are several turbulence models which can be used to close the hydrodynamic problem in the RANS method. In the hydrodynamic field, the widely used turbulence models are those with two-equation, such as the k-ω SST [45] and the Realizable k-ε. Finally, in order to discretize the physical model, the RANS solver is based on the FVM.

4.2 Spatial discretization schemes

The convection and diffusion terms in equation (4.1) can be discretized by using different numerical schemes which allow to estimate the face values of the flow variables. Most often, diffusion terms are discretized by using a Central Differencing (CD) scheme, where the face values are calculated through interpolation between the closest cells. In order to discretize the convection terms, the flow direction has to be taken into account.

The easiest way is to let the face value between two cells be equal to the value of the first upstream cell which is done in the first order upwind scheme. In the second order upwind scheme, the face value is calculated from the two closest upwind cells.

It is usually recommended to start a numerical solution process with lower order schemes, such as the first order upwind scheme, since they are stable. However, the low accuracy of these schemes may lead to a high degree of unphysical diffusion in the solution, which is known as numerical diffusion. The second order upwind scheme is often considered as a suitable discretization scheme, since it exhibits a good balance between numerical accuracy and stability.

4.3 The Finite Volume Method

The FVM is a numerical method of discretizing a continuous Partial Differential Equation (PDE), into a set of algebraic equations. The first step of the discretization is to divide the computational domain into a finite number of volumes, forming the mesh or the grid. Then, the PDE is integrated in each volume by using the divergence theorem, yielding an algebraic equation for each cell. In the cells' centers, cell-averaged values of the flow variables are stored in the nodes. This implies that the spatial resolution of the solution is limited by the cell size, since the flow variables do not vary inside a cell. The FVM is conservative, meaning that the flux leaving a cell through one of its boundaries is equal to the flux entering the adjacent cell through the same boundaries. This property makes it advantageous for problems in fluid dynamics.

All the CFD models using fully three-dimensional viscous formulations are typical of the FVM formulation, which need that the computational domain is discretized into a finite number of three dimensional volumes. The solution mesh may be created by using either a structured or unstructured approach. The structured approach requires a 1:1 mapping of grid points in the domain. Therefore, unstructured mesh greatly simplifies mesh generation for complex geometries,

and allows higher quality meshes to be created which result in greater numerical accuracy and faster computation time. The pros and cons of the two different mesh types are summarized in *Table 4.1*.

Table 4. 1. Pros and cons of the structured and unstructured mesh, source CD-Adapco User's Guide [46]

	Structured	**Unstructured**
Geometric Flexibility	less	greater
Adaptability of grid	less	greater
Suitability to the calculation of viscous flows (cells with a high aspect ratio)	greater	less
Deformable Grid	less	greater
Amount of Memory Required	greater	less
CPU Power Required	greater	less

The structured mesh is the fastest method, and uses the least amount of memory for a given number of cells. Multi-part or multi-region meshes with a conformal mesh interface are allowed. The structured meshing model employs in 3D cases the hexahedral cell shape in order to build the core mesh. In CD-Adapco Star CCM+, the Delaunay method is used to build the mesh, which iteratively inserts points into the domain, forming high-quality hexahedral in the process. The resulting mesh strictly conforms to the triangulation of the surface at the domain boundary, so that the quality of the original surface mesh allows to ensure a good quality volume mesh.

The unstructured meshes provide a balanced solution for complex mesh generation problems. They are relatively easy and efficient to build, requiring no more surface preparation than the equivalent hexahedral mesh. They also contain approximately five times fewer cells than a hexahedral mesh for a given starting surface. In addition, multi-region meshes with a conformal mesh interface are allowed. The unstructured meshing model generally uses an arbitrary tetrahedral cell shape in order to build the core mesh. The CD-Adapco Star CCM+ code has the distinction to use the polyhedral cell shape for unstructured mesh.

4.4 Pressure-velocity coupling method

The RANS equations contain one continuity equation and three momentum equations, if a 3D system is considered. There are four unknown variables in these equations, namely the pressure and the three velocity components. Therefore, there is no equation for the pressure, so that the continuity equation must be used as an indirect equation for the pressure. This is achieved by using a pressure-velocity coupling, which can be either segregated or coupled. The properties of these two groups of algorithms will be described briefly. A more thorough explanation was given by Versteeg and Malalasekera [47].

The semi-implicit method for pressure linked equations (SIMPLE) is a segregated algorithm solving each equation separately. This model solves the flow equations (one for each component of velocity, and one for pressure) in a segregated, or uncoupled, manner. The linkage between the momentum and continuity equations is achieved with a predictor-corrector approach. Firstly, a pressure is assumed and the velocities are calculated from the momentum equations. If the continuity equation is not satisfied by these velocities, the pressure is modified and the velocities are calculated again.

The complete formulation can be described with a SIMPLE-type algorithm. This model has its roots in constant density flows. Nevertheless, it can handle mildly compressible flows and low Rayleigh number natural convection flow, but it is not suitable for shock-capturing, high Mach number, and high Rayleigh-number applications.

4.5 Temporal discretization schemes

For transient problems, the transport equation must also be discretized in time. This is done by integrating the PDE over a time step, Δt, in addition to the spatial discretization. In order to solve this integrated equation, the cell values of the flow variables must be evaluated at a certain time.

Implicit time integration means that the flow variables are evaluated at the next time step, $t + \Delta t$. The implicit time integration requires iteration, since these variables are not known in the current time step. In comparison to explicit time integration, where the flow variables are evaluated at the current time step so that iteration is avoided, implicit time integration is more computationally expensive. On the other hand, implicit time integration is unconditionally stable, meaning that it is

stable for all time step sizes. The implicit unsteady model is the only unsteady model available with the SIMPLE segregated flow algorithm. The unsteady model is required in simulations with:

- Time-varying boundary conditions;
- Moving mesh problems;
- Free surface problems;
- Transient heat transfer.

In the implicit unsteady approach, each time-step involves some number of inner iterations to converge the solution for that given instant of time. The number of inner iterations in the time step is hard to quantify. Generally, this number is determined by observing the effect that it has on results. Smaller time steps generally mean that the solution is changing less from one time step to the next one; therefore fewer inner iterations are required.

The Courant Friedrichs Lewy (CFL) number is a helpful indicator for selecting the time step size: for time accurate simulations, the CFL number should be one on average in the zone of the interest. This value implies that the fluid moves by about one cell per time step. There is an optimal balance of time step size and number of inner iterations for a given problem and desired transient accuracy. If the convergence of iterations is slow, the time step is too large and there are significant temporal discretization errors. Generally, it is better to reduce the time step than to perform much iteration within a large time step.

4.6 The Free Surface Models

As above mentioned, a peculiarity of ship hydrodynamic problems is the presence of the water free-surface. For simulation of viscous free surface flow, several different theoretical models can be used, due to the large differences in the treatment of the water surface typically used. A popular classification of water surface models is reported in Wackers et al. [48].

- Fitting methods, where the grid is deformed and free-surface boundary conditions are applied to a boundary of the grid. These methods are usually solved in an iterative process, where, alternately, the flow field is computed and the grid is deformed to match the current shape of the wave surface.
- Interface Capturing methods with reconstruction. In these methods, the grid is not necessarily deformed. The interface is defined as a surface which cuts through the grid.

Initially, this surface has been defined by convecting marker particles on the surface with the flow field. Later, variants of the VOF method use the convected value of the water volume fraction in cells to determine the surface location. The latest addition to these methods is the level-set method, where the plane is defined by a convected continuous function.

- Interface Capturing methods without reconstruction. For these methods, like the original VOF method as formulated by Hirt and Nichols [49], a volume fraction equation determines the amount of each fluid in the cells, and local fluid properties are set as a mixture of the two pure-fluid properties according to this volume fraction. No attempt is made to reconstruct the interface. Conversely, it appears as a numerical discontinuity in the volume fraction.

The comparison of the different free-surface simulation techniques available in the existing CFD codes are reported in the report of Gothenburg 2010 workshop [2], as shown in *Figure 4.1*. The VOF method is the most popular choice. Level-set method is slightly popular and identifies the second largest group (5 codes, 17%). Only 3 of the 33 existing codes (9%) use the free-surface fitting methods.

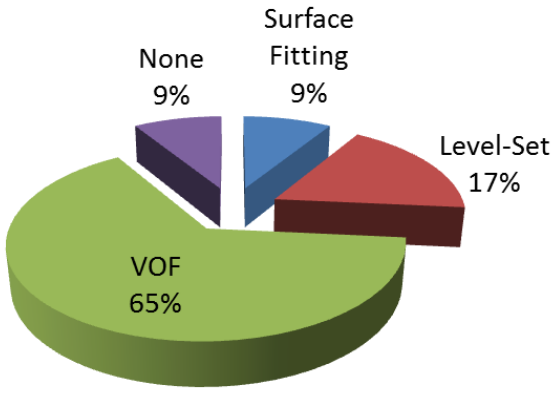

Figure 4. 1 Gothenburg Workshop 2010 – free surface models in the widely used CFD codes, source: Bohm [50]

4.6.1 VOF discretization schemes

As mentioned above, the VOF method is the widely used free-surface scheme, and the CD-Adapco Star CCM+ also uses this method. The VOF employs the concept of an equivalent fluid. This approach assumes that the (two) fluid phases share the same velocity and pressure fields thereby allowing them to be solved with the same set of governing equations describing momentum

and mass transport as in a single phase flow. The volume fraction α_i of the i^{th} phase describes to which level the cell is filled with the respective fluid.

$$\alpha_i = \frac{V_i}{V} \tag{4.3}$$

The VOF approach is suitable when the grid is fine enough to resolve the interface between two immiscible fluids and it is a simple multiphase model. The free surface is then defined as the isosurface at which the volume fractions take the value of 0.5, as shown in *Figure 4.2*. It is important to note, that this location is not at the control volume center but rather interpolated to the geometrical value.

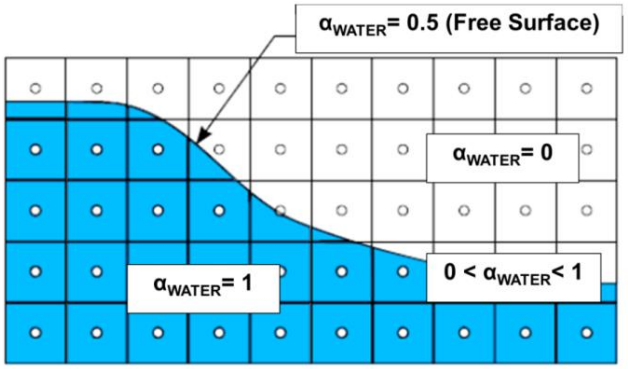

Figure 4. 2 Visualization of air and water volume fractions and related free-surface, source: CD-Adapco User's Guide [46]

To simulate wave dynamics, an equation for the filled fraction of each control volume is solved, in addition to the equations for conservation of mass and momentum. Assuming incompressible flow, the transport equation of volume fractions is described by the following conservation equation.

$$\frac{\partial}{\partial_t}\int_V \alpha_i dV + \int_V \alpha_i (V - V_b) n dS = 0 \tag{4.4}$$

The physical properties of the equivalent fluid within a control volume are then calculated as functions of the physical properties of the phases and their volume fractions.

$$\begin{cases} \rho = \sum_i \rho_i \alpha_i \\ \mu = \sum_i \mu_i \alpha_i \\ 1 = \sum_i \alpha_i \end{cases} \tag{4.5}$$

Strict conservation of mass is crucial, but this is easily obtained within this method as long as it is guaranteed that equation 42 is fulfilled. The critical issue for this kind of methods is the discretization of the convective term. Low-order terms like for instance first order upwind are known to smear the interface and introduce artificial mixing of the two fluids. Therefore higher order schemes are preferred. The goal is to derive schemes which are able to keep the interface sharp and produce a monotone profile over the interface. All of these schemes are based on the Normalized Variable Diagram (NVD) and the Convection Boundedness Criterion (CBC).

4.6.2 Normalized Variable Diagram

The NVD provides a framework for the development of convective schemes which, in combination with the CBC, guarantees boundedness of the solution. In the context of the NVD, boundedness allows to create convection schemes which are both stable and accurate. All elementary schemes have certain advantages and disadvantages. Pure upwind schemes are stable but diffusive. The central differencing scheme is more accurate but introduces propagating dispersion thereby leading to unphysical oscillations in large regions of the solution. Therefore, practical schemes are often designed as a blending of upwind, downwind and central differencing schemes to obtain the desired properties. The advantage of the NVD is its simplicity. For a 1-D case the NVD takes the following form.

The *Figure 4.3* shows three cells in the vicinity of a cell face *f*, across which the velocity v_f is known. The nodal variable values are labelled, α_D, α_C and α_U, representing the downwind, central, and upwind positions relative to each other.

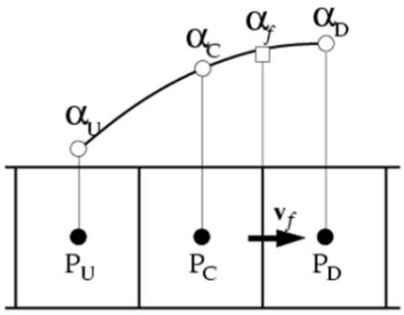

Figure 4. 3 Upwind, downwind, and central cells that are used in the analysis[50]

The normalized variable $\xi(r, t)$ in the vicinity of face f is defined as:

$$\xi(r,t) = \frac{\alpha(r,t) - \alpha_U}{\alpha_D - \alpha_U} \tag{4.6}$$

And the normalized face value:

$$\xi_f = \frac{\alpha_f - \alpha_U}{\alpha_D - \alpha_U} \tag{4.7}$$

With this definition, any differencing scheme using only nodal values at point U, C and D to evaluate α_f may be written as:

$$\xi_f = \xi_f\ (\xi_C) \tag{4.8}$$

To avoid that the solution unphysically oscillates, α_C has to be locally bounded between α_U and α_D:

$$\alpha_U \le \alpha_C \le \alpha_D \tag{4.9}$$

If this criterion is satisfied for each point in the solution domain, then no unphysical oscillations will occur, for example, the phase volume fraction cannot become negative, or larger than unity.

According to the CBC, a numerical approximation of ξ_f is bounded, if are achieved the following conditions:

- For $0 \leq \xi_C \leq 1$ the bounded region lies above the line $\xi_f = \xi_C$ and below $\xi_f = 1$.
- For $\xi_C \leq 0$ and $\xi_C > 1$, $\xi_f = \xi_C$.

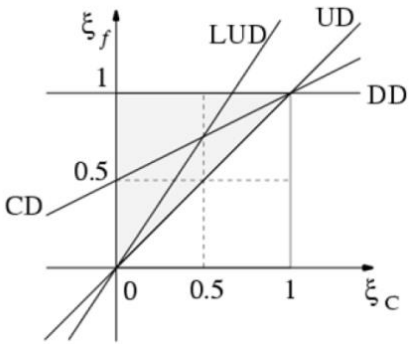

Figure 4. 4 The NVD with the linear schemes: Central Differencing (CD) and Linear Upwind Differencing (LUD): the shaded area shows the zone for which the CBC is valid [50]

Observing the *Figure 4.4*, it has to be noted that, with exception of Upwind Differencing (UD), none of these linear schemes (CD and LUD) fulfil the boundedness criterion. Therefore, it can be concluded that the linear schemes either lack stability or accuracy. The need of boundedness, stability and accuracy consequently led to the combination of the advantages of the different linear schemes. This led to the development of nonlinear schemes.

Lower order numerical schemes are bounded but will smear out the interface due to numerical diffusion while higher order schemes are more accurate but less stable.

A combination of higher and lower order schemes is often used like in the High-Resolution Interface Capturing (HRIC) and the Compressive schemes used in CD-Adapco STAR CCM+ and in most commercial and not CFD codes. More details about the different Interface Capturing schemes are available in Wackers et al. [51].

4.6.3 HRIC scheme

The HRIC scheme is designed to mimic the convective transport of immiscible fluid components, resulting in a scheme which is suited for tracking sharp interfaces, that is an important quality of an immiscible phase mixture (*e.g.*, air and water).

The HRIC scheme, based on the Compressive Interface Capturing Scheme for Arbitrary Meshes (CICSAM) introduced by Ubbink [52] and developed by Muzaferija and Peric [53], uses a

combination of upwind and downwind interpolation. The aim is to combine the compressive properties of the downwind differencing scheme with the stability of the upwind scheme. The blending of the schemes in each cell is a function of the volume fraction distribution over the neighboring cells. The value of the flow variable is then corrected by the local value of the CFL number.

The bounded downwind scheme is formulated as:

$$\xi_f = \begin{cases} \xi_C & if \quad \xi_C < 0 \\ \xi_C & if \quad 0 \le \xi_C < 0.5 \\ 1 & if \quad 0.5 \le \xi_C < 1 \\ \xi_C & if \quad \xi_C \ge 1 \end{cases} \qquad (4.10)7$$

Since the amount of one fluid convected through a cell face shall be less or equal than the amount available in the donor cell, the calculated value of ξ_f is corrected with respect to the local *CFL* number. The correction takes the form of equation below reported and effectively controls the blending between HRIC and UD scheme with two limiting Courant numbers CFL_L and CFL_U which normally takes values of 0.5 and 1.0 respectively.

$$\xi^* = \begin{cases} \xi_f & if \quad CFL < CFL_L \\ \xi_C + (\xi_f - \xi_C)\dfrac{CFL_U - CFL}{CFL_U - C_U} & if \quad CFL_L \le CFL < CFL_U \\ \xi_C & if \quad CFL_U \le CFL \end{cases} \qquad (4.11)$$

Effectively, this correction implies that the HRIC scheme is used for a local *CFL* smaller than the CFL_L limiter and UD scheme for *CFL* equal or greater than the CFL_U limiter. Between those values a blending of both schemes is used. This correction is applied to improve robustness and stability when large time variation of the free surface shape is present and the time step is too big to resolve it.

The HRIC scheme is the currently most successful advection scheme and widely used in CFD. Nevertheless, various authors, including Andrilion and Alessandrini [54] and Ferziger and Peric [55], have found that the local CFL dependency scheme can cause the spread of the free surface interface, and this could be the main cause of the artificial mixing of air and water, which is nominally known as numerical ventilation.

4.7 The Rigid body motion

The 6 Degrees of Freedom (6-DOF) models solve the rigid body motion of an object exposed to fluid forces. The 6-DOF body is created with a Dynamic Fluid Body Interaction (DFBI) motion. This approach is suitable for the hydrodynamic simulations that require capability to capture the change of position of the hull during the simulation.

The model DFBI is used to simulate the motion of a rigid body in response to pressure and shear forces that the fluid exerts on the body. The code calculates the resultant force and moment acting on the body due to all influences, and solves the governing equations of rigid body motion to find the new position of the rigid body relative to the body local coordinate system, as also reported in CD-Adapco User's Guide [46]:

$$\begin{aligned} m\frac{dv}{dt} &= f \\ I\frac{d\overline{\omega}}{dt} + \overline{\omega} \times I\overline{\omega} &= n \end{aligned} \tag{4.12}$$

where:

- m is the mass of the body.
- f is the resultant of the forces acting on the body.
- v is the speed of the center of mass.
- I is the tensor of the moments of inertia.
- $\overline{\omega}$ is the angular velocity.
- n is the moment of the resultant force acting on the body.

The force and the resulting moment acting on the body are obtained by the fluid pressure and shear forces acting on each face of the boundaries of the body. The workflow of the rigid body motion technique is shown in *Figure 4.5*.

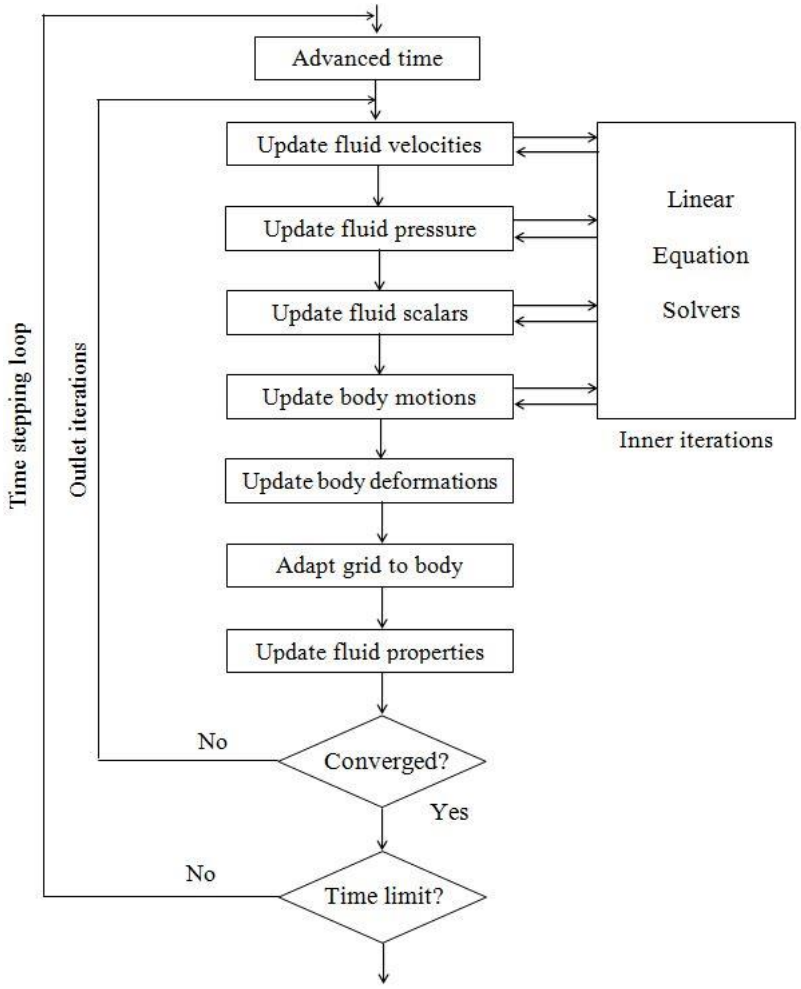

Figure 4. 5 Workflow of rigid body motion

4.8 Dynamic meshing

To be able to handle motion, it is necessary that the mesh structure changes dynamically with the moving object. There are different methods for the dynamic movement of the mesh. The three that are most suitable for hull simulations are the simple moving grid, the diffusion-based smoothing method/morphing grid, and the Overset/Chimera grid, which are described in the following sections.

4.8.1 Moving grid

Within this method, the entire grid is moved according to the motions of the rigid body. The grid itself is not altered but instead kept rigid. This approach bears several advantages. Among other, there is the great robustness and low computational efforts due to the fact that only the flow

variables have to be corrected according to the body motion. On the other hand, the method is only applicable for the motion of one rigid body.

As regards the application of this technique to the simulation of resistance test of planing hull, there are two main and significant drawbacks. The first one is the care which has to be taken to smoothly resolve the free surface interface. *Figure 4.6* shows a plane of a grid including the free water surface. It can be noted that the grid pattern on the stern of the hull follows the free surface contour, while increasing the trim angle, the grid pattern no longer follows the water free surface.

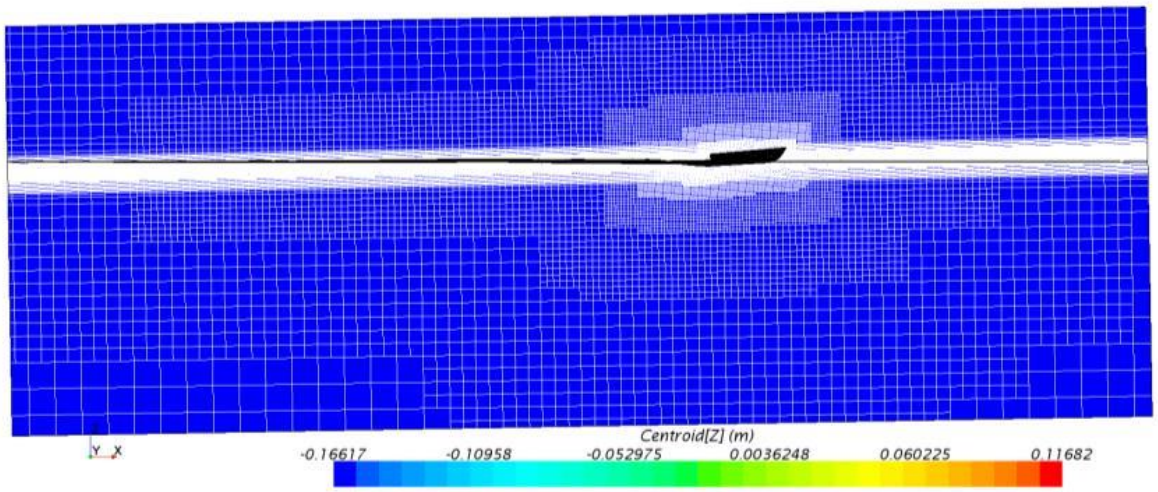

Figure 4. 6 Resistance test simulation of planing hull using moving grid with free-surface and mesh visualization

The second drawback is connected with the first one. Indeed during the simulation of resistance test, in particular for planing hull, there is, in the initial phase, oscillations of the trim and sinkage of the hull caused the variation of height of the water plane at the inlet and outlet boundaries, as reported by Viola et al. [56]. Such oscillations introduce a “fake-wave” into the computational domain, which can induce additional oscillation of the trim, sinkage, and resistance of the hull. This “fake-wave” can affect the convergence significantly.

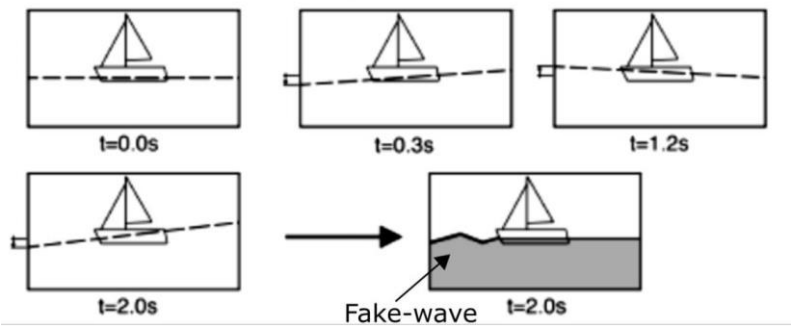

Figure 4. 7 Schematic drawing of the free surface perturbation and “fake-wave” due to the moving grid for inlet boundary, source: Viola et al. [56].

In order to minimize the generation of “fake-wave” and to avoid that the grid pattern no longer follows the water free surface, there are some tricks, such as:

- The upstream inlet face should be as close as possible to the boat and the hull.
- If the final sink and trim are known, these values should be used as the initial conditions for positioning the hull.
- Use of the damping function on the wave surface near the boundaries.
- The pitching inertia can be increased respect to the experimental (and real) value to speed up the convergence.
- Extension of the height of the grid refinement for the water free surface (high increase of number of cells).

However, some of these tricks can be a source of error, thereby increasing uncertainty, reducing the reliability of the simulation, and increasing the computational efforts. For these reasons, alternative solutions are checked to the simple moving grid technique.

4.8.2 Overset/Chimera grid method

The overset/chimera grid method uses two regions of meshes, one for the moving part and one for the stationary background, as shown in *Figure 4.8*. The moving part, referred to the overset mesh, uses the mesh rotation and translation method where the fluid mesh is replaced with a rigid body mesh. All cells maintain their shape and the mesh motion is described by a displacement vector and rotation angles. In the case that there is a solid that interacts with the fluid, the position of the mesh is determined by solving the equations of the motion and rotation of the body.

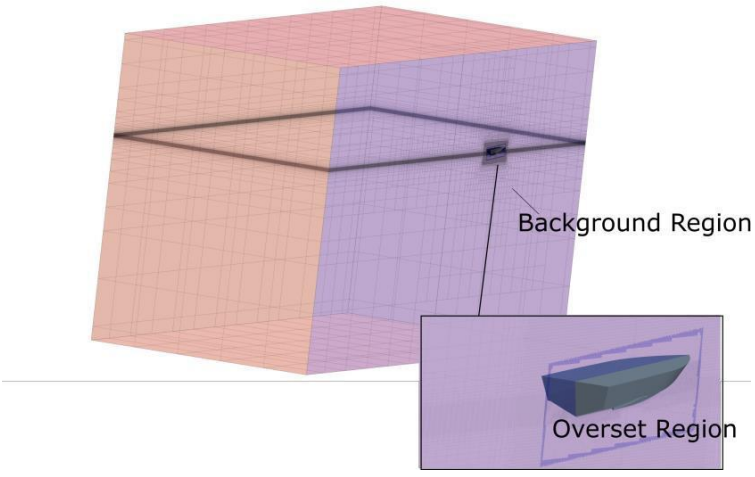

Figure 4. 8 The overset/chimera grid with the two regions: moving region (overset) and stationary region (background)

It is important to observe that this approach is not a conventional way to rank the performances of the hulls in the still water condition. Only a few researchers used this approach, as Carrica et al. [57] and Bertorello et al [58]. Usually this technique is used for numerical simulation of maneuvering tests, roll decay tests and to estimate the ship's response to waves, as Tezdogan et al. [59], Begovic et al. [60], and Swidan et al. [61].

To establish the connectivity between the background and the overset regions, a two-step overset assembly process takes place as described below. The cells around the interface of the overset mesh are identified and labelled as donor cells. Then, the cells in the background closest to the donor cells are identified and set as acceptor cells. These cells have to form a continuous layer of cells around the overset mesh. The background cells that are completely covered by the overset region are inactivated (the hole cutting process). The donor and acceptor cells transfer information between the meshes. Each acceptor cell has one or more donor cells. The set of donor cells depends on the interpolation option chosen and on the number of active cells in the donor region around the acceptor cell centroid.

As reported in CD Adapco User's Guide [46], the interpolation schemes are:

- Distance-weighted, where the interpolation factors are inversely proportional to the distance from acceptor to donor cell center, resulting in the closest cell giving the largest contribution. This involves 3 donor cells (in 2D case) or 4 (in 3D case).
- Least squares, consider mapping data from faces of the background mesh to faces of the overset mesh using a least squares scheme. Assuming a face in a cell of the background mesh (Face 0), as the closest to a face (Face A) of the target cell (in the overset region). The neighbors of Face 0 are defined as any face that shares at least one vertex with Face 0. These neighbors are included as part of the interpolation stencil. The solver uses the second-order terms of a Taylor series expansion as a "cost function" to approximate the error of the function distribution at assigned point. It then minimizes the cost function in equation for the function at the target point A.

  The drawback of a neighbor-based least squares scheme is that some of the faces of the background mesh that the target face imprints upon are not included in the stencil. More details of the neighbor-based least squares scheme are reported in CD Adapco User's Guide [46].

- Linear interpolation using shape functions spanning a triangle (in 2D case) or a tetrahedron (in 3D case) defined by centroids of the donor cells. This option is more accurate, but also more expensive in terms of calculation effort

The interpolation function is built directly into the coefficient matrix of the algebraic equation system.

In the *Figure 4.9*, two acceptor cells are shown using dashed lines, one in the background mesh and one in the overset mesh. The fluxes through the cell face between the last active cell and the acceptor cell are approximated in the same way as between two active cells. However, whenever the variable value at the acceptor cell centroid (marked by the open symbols in the *Figure 4.9*) is calculated by the weighted variable values at the donor cells using the following expression:

$$\varphi_{acceptor} = \sum \alpha_i \varphi_i \tag{4.13}$$

where α_i is the interpolation weighting factor, φ_i is the value of the dependent variable φ at donor cells N_i and subscript i runs over all donor nodes of an interpolation element (denoted by the green triangles in the figure). This way, the algebraic equation for the cell "C" in the figure below involves three neighbor cells from the same mesh (N_1 to N_3) and three cells from the overlapping mesh (N_4 to N_6).

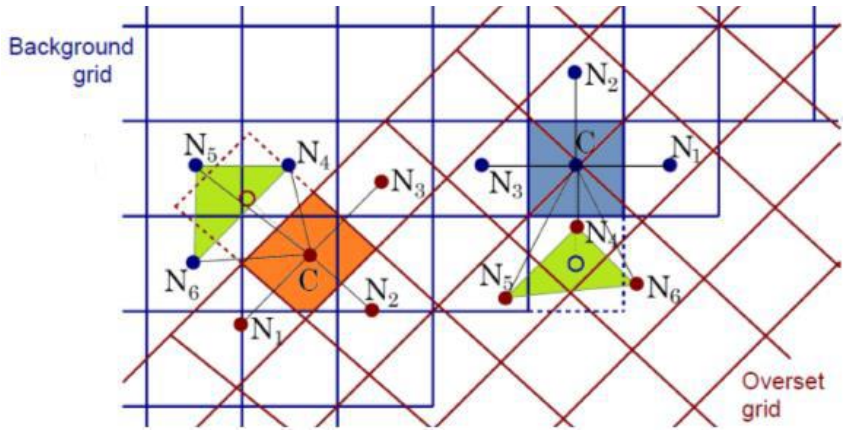

Figure 4. 9 Connectivity between the background and the overset regions, source: CD-Adapco User's Guide [46]

The advantage with the overset method is that only a certain part of the mesh is moving without requirement for altering the grid topology. A drawback is that the interpolation between the meshes

can cause numerical errors and increase the computational effort. The pros and cons of the overset mesh are reported in *Table 4.2*.

Table 4. 2. Pros and cons of the overset and morphing mesh, source CD-Adapco User's Guide [46]

	Chimera/Overset Grid	**Morphing Grid**
Geometric Flexibility	greater	greater
Adaptability of grid	less	greater
Suitability to the calculation of viscous flows (cells with a high aspect ratio)	greater	greater
Deformable Grid	greater	medium
Amount of Memory Required	greater	uncertain
CPU Power Required	greater	uncertain

4.8.3 Smoothing/Morphing mesh

The dynamic meshing can be incorporated using smoothing methods, also called morphing mesh technique, where the cells are moved with a deforming boundary, whereas the number of cells and their connectivity remain unchanged, as shown in *Figure 4.10*. The morphing mesh is suitable for complicated and arbitrary relative motion and for relatively small boundary deformations, while larger deformations may require generation of new cells in order to maintain a high quality mesh. Among the smoothing methods, there is the diffusion-based smoothing, where the motion of the cells is modelled as a diffusive process.

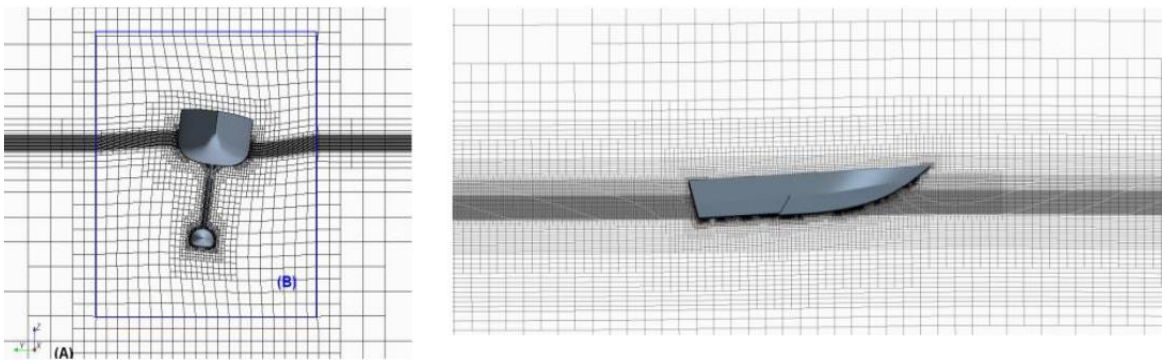

Figure 4. 10 Examples of smoothing/morphing mesh in marine hydrodynamics application: (left) sail yacht, source: Bohm [50]; (right) planing stepped hull simulation

Traditionally the morphing mesh can be used to model scenarios where components deform and change shape, *e.g*. in marine application field: Kang et al. [62] and Biancolini and Viola [63]. However this technique has been never used in ship hydrodynamics for resistance test simulations.

The morphing mesh can be employed easily for the rigid body motion case. During the process of morphing, the mesh vertices are redistributed in response to the movement of a set of control points. The morpher solver, as reported in CD-Adapco User's Guide [46], takes the control points and their associated displacements and generates an interpolation field. The interpolation field is then used to displace the vertices of the mesh based on Radial Basis Functions (RBF) method.

To generate the interpolation field, a system of equations is solved, using the control vertices and their specified displacements: for every control vertex i, its displacement $d_i^{'}$ is approximated with the combination:

$$\begin{aligned} d_i^{'} &= \sum_{j=1}^{n} \lambda_j \sqrt{r_{ij}^2 + c_j^2} + y \\ r_{ij} &= \left\| x_i - x_j \right\| \end{aligned} \tag{4.14}$$

where r_{ij} is the magnitude of the distance between two vertices; λ_j is the expansion coefficient, x_i is the position of vertex i; n is the number of control vertices; c_j is the basis constant; and y is a constant value. More details about the RBF method and the morphing mesh technique are reported in de Boer et al. [64] and Biancolini [65].

5

NUMERICAL TEST

In order to confirm the experimental results presented above, including the existence of the observed vortices, a campaign of computational fluid dynamics simulations has been carried out. Moreover, a detailed study of the flow field has been made to reconstruct the vortex patterns both into the unwetted aft body area and in water downstream the step.

In this section, the details of the numerical setup used in all the simulations are reported. In particular, the detailed analysis of common and different setup used in the two different mesh approaches applied in this study are presented and discussed.

Unsteady RANS simulations have been performed for four model speeds: 2.357, 4.631, 6.340, and 8.050 m/s, corresponding to Fr_∇ = 1.984, 3.898, 5.337, and 6.777, respectively. All simulations have been made with two different mesh treatments as discussed in the following.

5.1 Physical modeling and coordinate system

The unsteady RANS equations are solved using an implicit and iterative solver in order to find the field of all hydrodynamic unknown quantities in each time step. The velocity–pressure coupling and overall solution procedure are based on a semi-implicit method for pressure-linked equations (SIMPLE) to conjugate pressure and velocity fields. The discretized algebraic equations are solved using a point-wise Gauss–Seidel iterative algorithm and an algebraic multigrid (AMG) method was employed to accelerate the solution convergence. Furthermore, a segregated flow solver approach is used for all simulations and the turbulence closure of the RANS equations was ensured by the k-ω shear stress transport (SST) turbulence model.

The RANS solver is based on a finite-volume method to discretize the physical domain. The relative numerical results presented in Chapter 6, have been obtained by solving the full unsteady flow equations and marching the numerical simulation in time with a pseudo-compressibility approach, to be discussed in the next Chapter.

The equations for the incompressible multiphase fluid are joined with one more transport equation for the VOF model. This equation helps to ensure the correct shape of the free surface between water and air. In these simulations, the modified high-resolution interface capturing scheme (HRIC) is used as advection schemes. The modified configuration of the HRIC scheme removes the dependency scheme on local Courant-Friedrichs-Lewy number (CFL), as reported in [55]. This correction is applied to avoid the spread of the free surface interface because this could be the main cause of the problem nominally known as numerical ventilation (NV), [54, 56]. This problem is one of the main sources of error in the numerical simulation, in particular for planing hull resistance test simulation, as indicated in [59].

In order to simulate the hull free to move in the pitch and heave directions, the dynamic fluid body interaction (DFBI) model is used. The DFBI model allows the RANS solver to evaluate the force and moments on the hull and to solve the governing equations of body motion in order to relocate the body. The DFBI model is applied by using two different methods: the overset mesh method and the morphing grid.

The right-hand orthogonal coordinate system, as used in all simulations, has the origin O-XYZ of the reference frame located in the longitudinal position of the center of buoyancy (LCB) (X coordinate), in the vertical position of the calm free surface (Z coordinate), and transversal position in the symmetry plane (Y coordinate). The x-axis is forward and parallel to the baseline of the hull, the y-axis is to portside, and the z-axis is vertically upward.

A CFD code commercially available STAR-CCM+ by CD-adapco is used for mesh generations and computations.

5.1.1 Computational domain and time-step analysis

As for the computational domain, the overset mesh technique requires two different regions, i.e., the background and overset regions, as shown in *Figure 5.1 (a)*. However, it is important to note that, in the ship hydrodynamics field, no defined recommendations in terms of domain dimensions are available for the overset region, as indicated in [59]. However, the background region usually is

designed in compliance with the ITTC's CFD recommendations (in particular the dimensions are not less than twice the ITTC recommendations) [66].

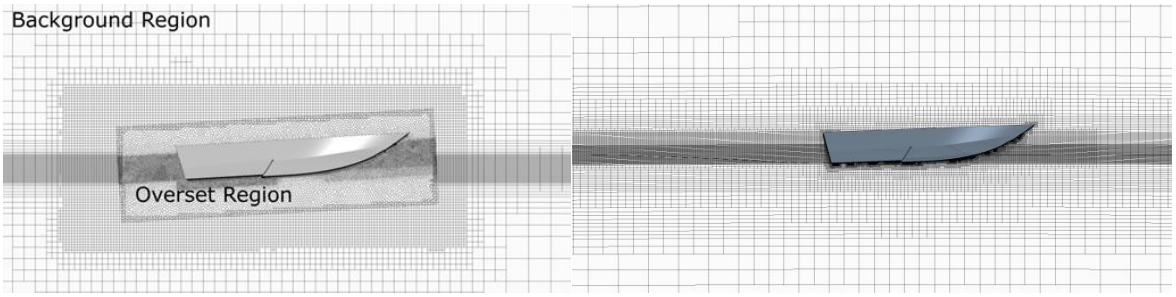

(a) *(b)*

Figure 5. 1 (a) Overset grid visualization with different meshes for regions (polyhedral: overset region, trimmed: background region; (b) Morphing mesh visualization

In regards to the morphing mesh approach, only one region is required, and the relevant dimensions of the calculation domains are in compliance with the ITTC prescriptions [66] (in particular the dimensions are not less than 2.5 times the ITTC recommendations), as shown in *Figure 5.1 (b).*

The dimensions of the calculation domains and the boundary conditions for the two different mesh approaches are illustrated, in *Figure 5.2, Figure 5.3, Figure 5.4,* and *Figure 5.5,* respectively.

The boundaries are placed far enough away from the ship hull in order to avoid the reflection of the fluid flow from the boundaries.

The flow around the ship hull can be assumed symmetrical with respect to center plane of the hull. This is a typical boundary condition used in the CFD resistance test simulations, as indicated in the ITTC guidelines [66], and the effects of this assumption are negligible in terms of simulation results, as indicated in many works. This is a reasonable assumption that leads to significant reduction in computational time. Therefore, a symmetry plane is located in the center line of the domain.

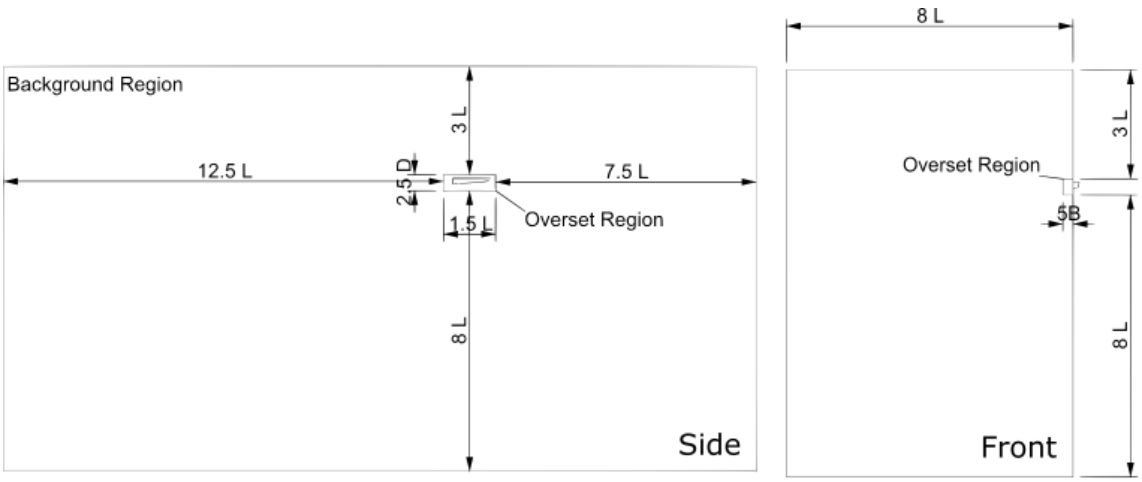

Figure 5. 2 Domain dimensions: overset grid case

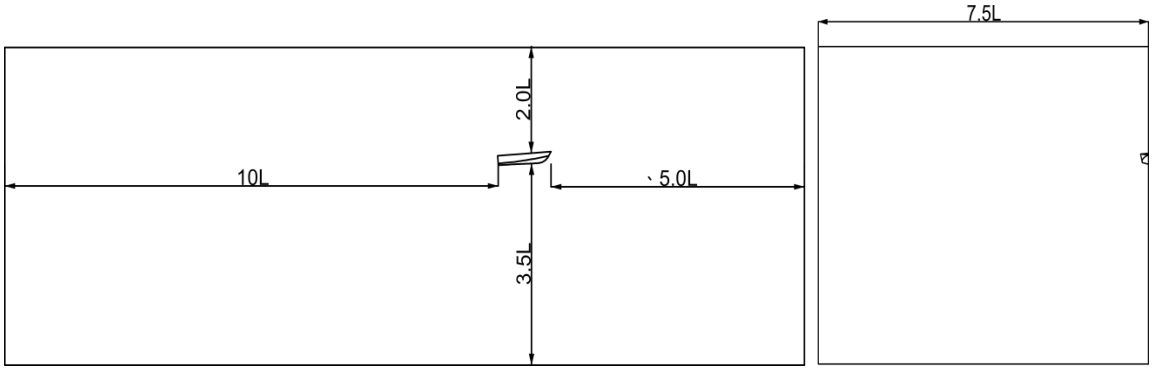

Figure 5. 3 Domain dimensions: morphing grid case and LES simulation

The time-step used in the simulations is a function of the hull speed, according to the following ITTC equation [66]:

$$\Delta t = 0.01 \div 0.005 \frac{l}{V} \tag{5.1}$$

where V is the hull speed and l is the characteristic length value of the analyzed body. In this thesis, l is assumed equal to dynamic L_{WL}, detected by towing tank tests at each analyzed speed. Furthermore, the time-step is a function of the grid density in order to keep constant the *CFL* number.

A summary of the main properties of the numerical solver used for the overset and morphing mesh cases are reported in *Table 5.1*.

Table 5. 1 Summary of numerical simulation setup

Pressure link	SIMPLE
Pressure	Standard
Convection Term	2nd Order
Temporal Discretization	1st Order
Time-step (s)	Function of velocity and grid
Iteration per time-step	5
Turbulence Model	k-ω SST

5.2 Overset/chimera grid setup

One of the main advantages of the overset/chimera grid technique for the hull motion is that this approach avoids numerical accuracy losses in inclined positions in the far fields, which is a typical problem occurring on the planing hulls where there is a significant variation of the dynamic trim angle, as reported in [56].

However, the simulations performed with the overset/chimera grid method requires additional settings. In particular, to establish the connectivity between the background and the overset regions, an interpolation scheme is required. According to previous numerical tests conducted on planing hulls models [28], it is identified that the linear interpolation scheme is the most suitable in terms of adequacy of the numerical results with the experimental data. However, the computational effort required is higher than in other methods. A detailed analysis of the different interpolation schemes available with the overset/chimera grid method are reported in [46]. The overset mesh solution for this analysis is similar to the solution adopted in [58] with trimmed mesh (background region) and polyhedral mesh embedded zone (overset region), as shown in *Figure 5.1 (a)*. The main data of the mesh solution chosen for the background and overset regions are given in *Table 5.2*.

Table 5. 2 Overset case: mesh properties summary

Type of mesh	Trimmed (Background. Region)	Polyhedral (Overset Region)
No. of cells	662290	1994122
Base size (m)	0.3	0.7

The dimensions of the calculation domains and the boundary conditions are shown in *Figure 5.2* and *Figure 5.4*, respectively.

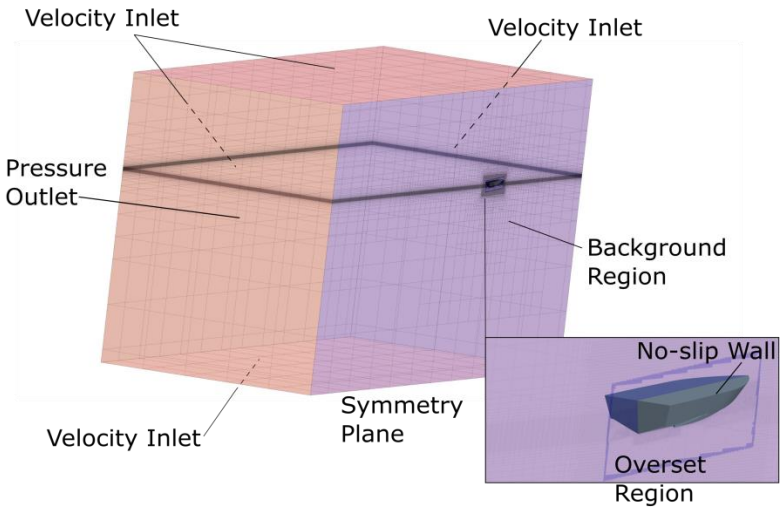

Figure 5. 4 Boundary conditions: overset grid case (view from the back of the domain).

5.3 Morphing mesh grid setup

It is known that morphing grids require special treatment of the moving nodes in order to control the accuracy of the space derivatives and of the time-stepping scheme. This is done by appropriately interpolating the fluid flow variables. Then, the interpolation field is used to displace the vertices of the mesh based on the RBF method. To generate the interpolation field, a system of equations is solved, using the control vertices and their specified displacements: for every control vertex i, its displacement $d_i^{'}$ is approximated by the combination:

$$d_i^{'} = \sum_{j=1}^{n} \lambda_j \sqrt{r_{ij}^2 + c_j^2} + \alpha \tag{5.2}$$

where $r_{ij} = \| x_i - x_j \|$ is the magnitude of the distance between two vertices, λ_j is the expansion coefficient, x_i the position of the vertex i, n is the number of control vertices, c_j the basis constant, and α a constant value. More details are reported in [64].

Differently from what happens for the overset/chimera grid method, the morphing grid does not require additional settings. The dimensions of the calculation domains and the boundary conditions are shown in *Figure 5.3* and *Figure 5.5* , respectively.

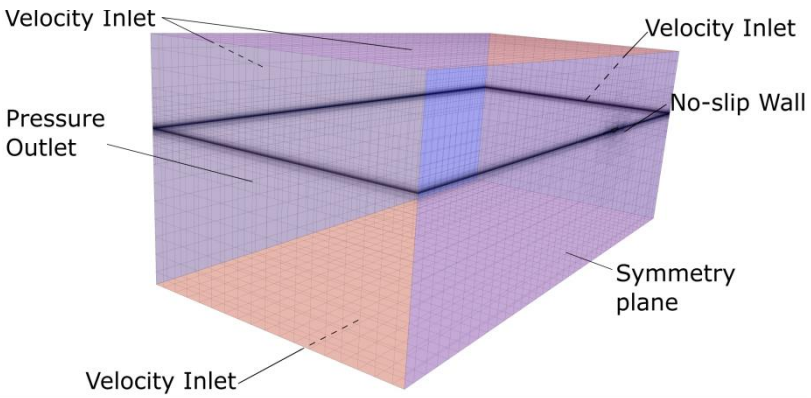

Figure 5. 5 Boundary conditions: morphing grid case (view from the back of the domain)

In simulation of the moving meshes, the morphing technique is combined with rigid motions, as mentioned above. Because morphing strategies can lead to poor quality cells, it becomes important to keep under control the topological deformations taking place in the surface mesh and in the volume cells, by means of specific mesh quality metrics. To minimize the topological deformations of the grid domain, the hull at the starting point has an initial trim angle of 2 degrees aft.

A visualization of the grid with refinement in the air/water interface area is shown in *Figure 5.1 (b)*.

5.4 Wall y + treatment

The wall function is used for the near wall treatment, and the *All-Wall y+* is the wall treatment used for all simulations. It is a hybrid approach that attempts to emulate the high *y+* wall treatment for coarse meshes (for $y+>30$), and the low *y+* wall treatment for fine meshes (for $y+\approx1$). It is also formulated with the desirable characteristic of producing reasonable answers for meshes of intermediate resolution (for *y+* in the buffer layer) [46]. This approach is considered a reasonable compromise among the acceptable quality of the boundary layer description and the calculation time. The values of wall *y+* on the hull are shown in *Figure 5.6*, where it is possible to observe the wall *y+* range on the hull at maximum speed tested for the two different mesh techniques.

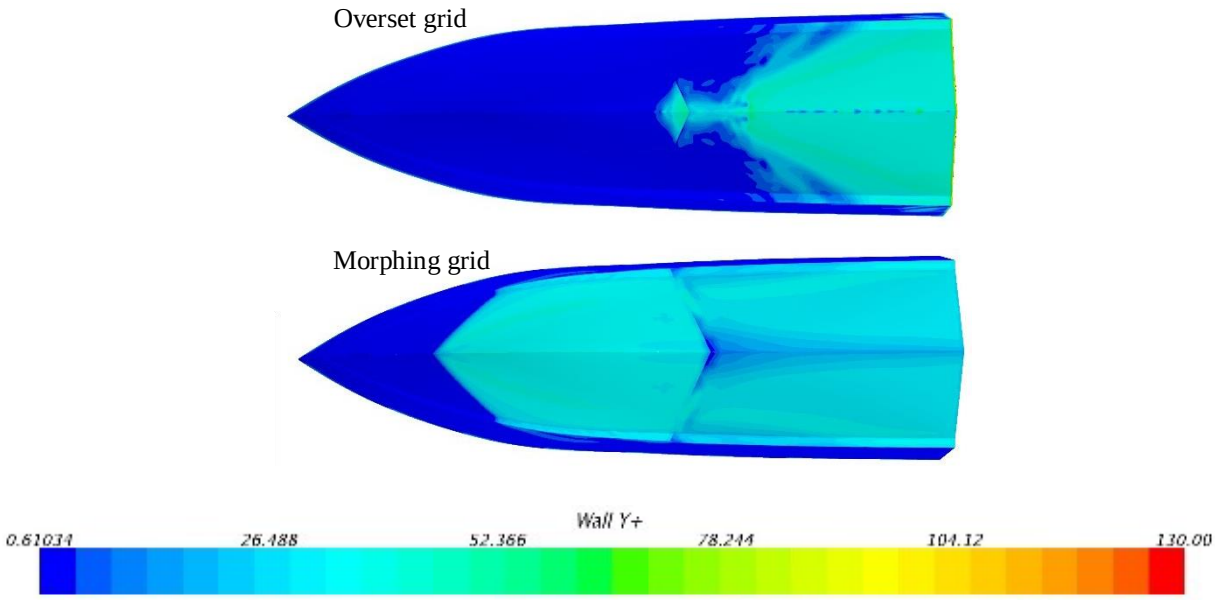

Figure 5. 6 Wall y+ visualization on the hull at Fr_∇=3.898 for the different mesh technique: overset/chimera grid (top), morphing grid (down)

5.5 Verification and Validation study

A verification and validation study (V&V) is carried out for R_{TM}/Δ, τ, $Z/\nabla^{1/3}$, and $S/\nabla^{2/3}$ at one speed (4.631 m/s, Fr_∇=3.898); the results of this analysis are reported in Appendix B.

The results of simulation and validation uncertainty for the two different simulations techniques, *i.e.*, overset and morphing mesh, are listed in *Tables B.1* and *B.2* in Appendix B, respectively.

The monotonic convergence is reached in all cases except for the sinkage in the overset mesh.

The validation process is achieved for the resistance/displacement ratio and for the trim angle in the overset case. In spite of what happens with the overset mesh, for the morphing mesh case a higher scatter in the solutions is detected. This is probably one of the main reasons for which the validation is achieved only for the sinkage and trim angle. When the comparison error is much higher than validation uncertainty (E >> U_V), in particular for the wetted surface, the validation is not achieved, but it is significant, and the main challenge becomes the improvement of the simulation modeling.

The iterative uncertainty is not reported in the tables reported in the Appendix, because it is found to be always negligible as compared with other sources of uncertainty as reported in similar studies, e.g., [58].

6

NUMERICAL RESULTS AND DISCUSSION

In this section, a comparison between experimental and numerical results is presented and discussed. The main aims are to evaluate the reliability of the different simulation techniques adopted, as well as to find a confirmation in the numerical simulations of the vortex phenomena observed experimentally in the aft body waterplane area behind the step.

Moreover, the numerical analysis is used to reconstruct with greater detail the recirculation paths, which are seen experimentally from top- and side-view photographs.

6.1 Total resistance, dynamic sinkage, and trim angle

The results in terms of $R_{TM}/\Delta, \tau, Z/\nabla^{1/3}$, and $S/\nabla^{2/3}$ are reported in *Figure 6.1*, *Figure 6.2*, *Figure 6.3*, and *Figure 6.4* versus Fr_{∇} respectively. The numerical results are in accordance with the experimental data and all of the experimental and numerical results are summarized in *Table 6.1*. The better performance of the overset grid approach is evident because, as compared with the experimental values, the percentage differences are in the range from 2.2% to 9.3% for the R_{TM}/Δ.

Similar results are achieved for trim angle. In fact, for velocities over the hump speed (3.13 m/s, 2.61 Fr_{∇}), the overset grid approach has better performance as compared to the morphing grid approach, based on the comparison with the experimental values. The difference between the two methods is mainly due to the underestimation of trim with morphing grid in velocity range over to the hump speed, as shown in *Figure 6.2*.

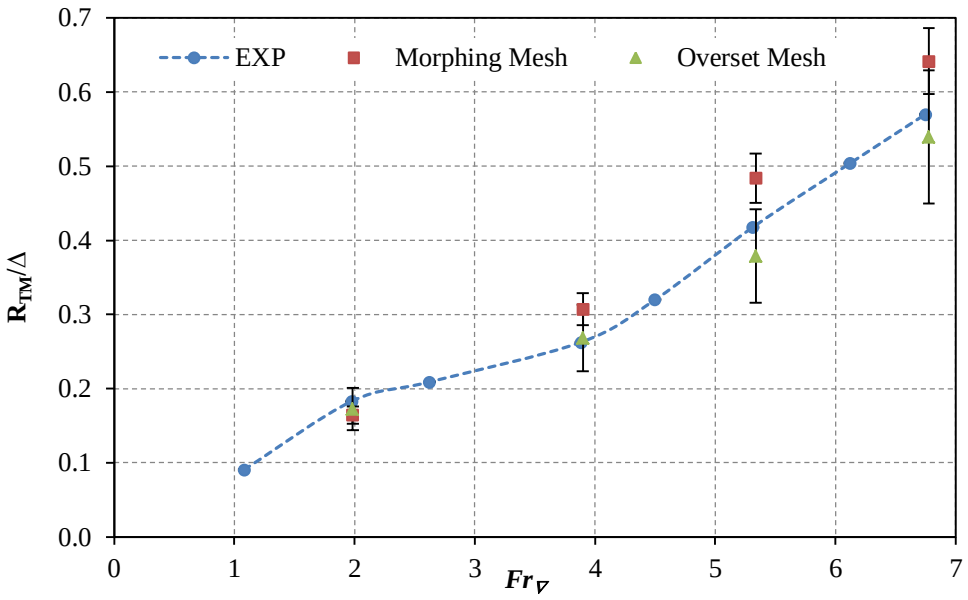

Figure 6. 1 Non-dimensional total resistance comparison between EFD and CFD simulations with uncertainty bars

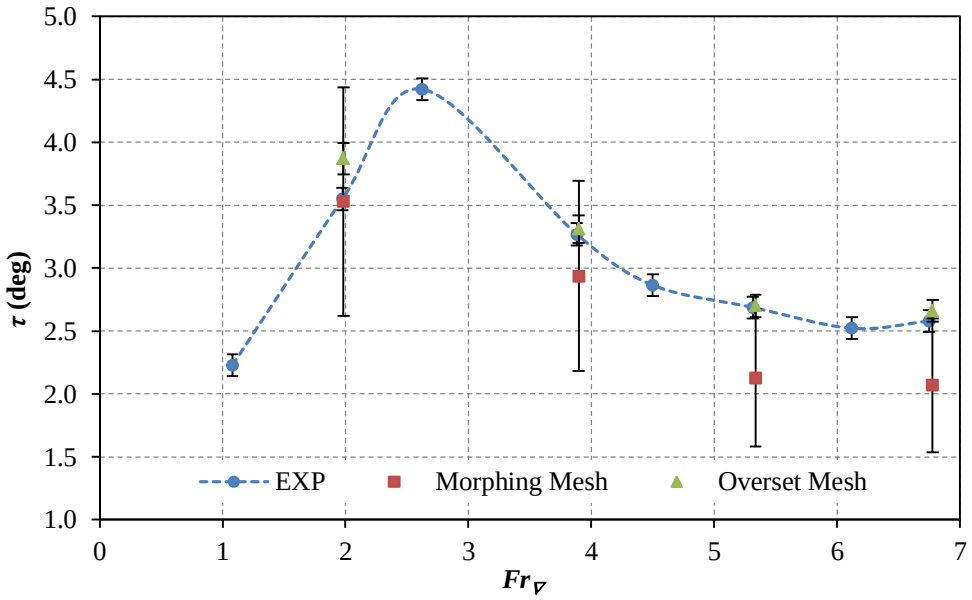

Figure 6. 2 Trim comparison between EFD and CFD simulations with uncertainty bars

The value of the numerical non-dimensional dynamic sinkage obtained with the two different mesh techniques are generally close to the experimental results and the percentage differences comparing the overset approach and morphing grid, are up to 8.9%, as shown in *Figure 6.3*.

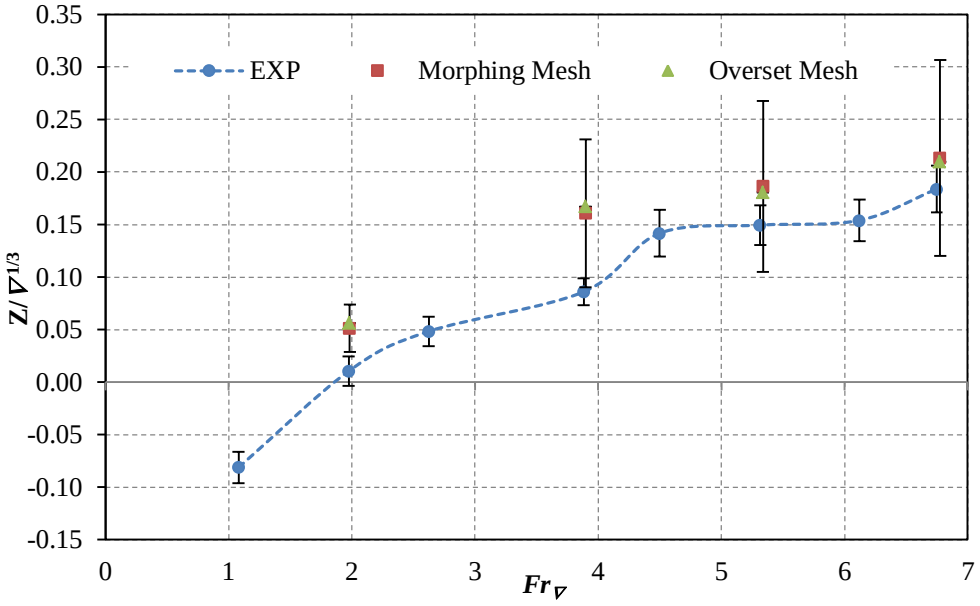

Figure 6. 3 Non-dimensional dynamic sinkage comparison between EFD and CFD simulations with uncertainty bars

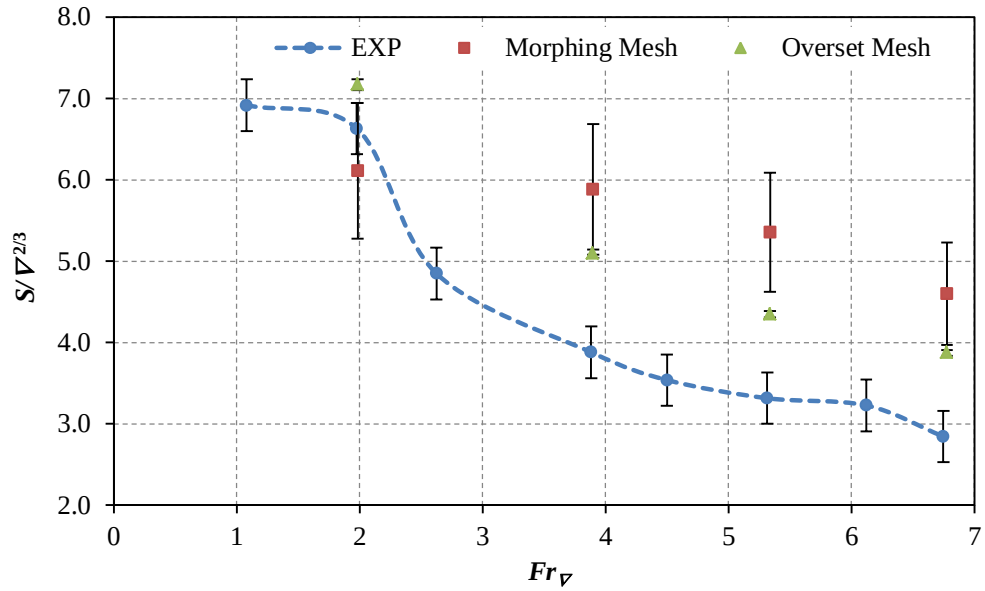

Figure 6. 4 Non-dimensional dynamic wetted surface comparison between EFD and CFD simulations with uncertainty bars

Table 6. 1 Experimental and simulation results

Fr_{∇}	$\frac{R_{TM}}{\Delta}$			τ			$\frac{Z}{\nabla^{1/3}}$			$\frac{S}{\nabla^{2/3}}$		
	Exp	CFD Morphing	CFD Overset.	Exp	CFD Morphing	CFD Overset	Exp	CFD Morphing	CFD Overset	Exp	CFD Morphing	CFD Overset
1.984	0.183	0.164	0.173	3.55	3.53	3.87	0.011	0.051	0.056	6.631	6.110	7.171
3.898	0.263	0.307	0.268	3.27	2.94	3.31	0.086	0.161	0.167	3.881	5.885	5.092
5.337	0.418	0.484	0.379	2.69	2.13	2.70	0.149	0.186	0.181	3.316	5.358	4.349
6.777	0.570	0.642	0.540	2.58	2.07	2.66	0.184	0.213	0.210	2.845	4.601	3.873

All the analyzed results show that the overset mesh technique is more effective than the morphing one, but also more demanding in terms of computational times required (1800 versus 980 seconds of CPU time per time step).

The errors in CFD predictions are in line with those indicated in [4]. Therefore, the morphing and overset mesh techniques result to be successful to predict performance of planing stepped hulls. In particular, the simulations campaign shows that the overset mesh ensures high-quality of the simulation results and shows high-adaptability to the wide variations of trim and heave of the stepped hull (thanks to the use of two regions, i.e. the moving or overset region and the background region). As consequence, the overset mesh is more suitable for the planing stepped hull, as also indicated in De Luca et al. [7].

It is well known that the traditional simulation approach (single grid with rigid body motion) for planing stepped hull presents two main and significant drawbacks. The first one is the care which has to be taken to smoothly resolve the free surface interface. The second is related to oscillations of the trim and sinkage values of the hull during the initial phase of resistance test simulation (for planing stepped hull). This problem is caused by the variation of the height of the water plane at the inlet and outlet boundaries, as reported by Viola et al. [56]. These oscillations introduce a "fake-wave" into the computational domain, which can induce additional oscillation of the trim, sinkage, and resistance of the hull.

6.2 Dynamic wetted surface

Figure 6.4 shows a comparison between numerical and experimental values of the $S/\nabla^{2/3}$ versus Fr_∇. The experimental wetted surface values are estimated through digital analysis of video frames, which are referenced to the original 3D CAD model. The numerical values are calculated by the fluid dynamics solver. In general, especially at high Fr_∇ number, the values of wetted surface calculated numerically are more reliable than those extracted from the video recordings.

A source of uncertainty in the estimation of wetted surface is the spray area, which is hard to evaluate experimentally on the basis of the video footages. In fact, as reported in Appendix A, the bias of $S/\nabla^{2/3}$ mainly consists of the bias of wetted surface estimation (B_S), which is 80.81% of $S/\nabla^{2/3}$ total bias.

The issue of evaluation of the spray area also affects the numerical solution; indeed, this evaluation is a nontrivial task for RANS solver and requires a very high-resolution grid, as indicated in [67]. In particular, it is necessary to consider the complexity/limit of the RANS solver to evaluate the spray sheet zone and the blister spray. These two aspect produce a high uncertainty on the wetted surface evaluation as reported in Mousaviraad et al. [67]. For this reason, the overestimation of the wetted surface as compared to the experimental results should be caused by using the VOF value equal to 0.5 as indicated in [66].

The numerical results are closer to the experimental measurements when obtained by the overset mesh approach, as compared to the morphing grid approach. The difference between the two numerical methods is mainly due to the underestimation of trim, as shown in *Figure 6.2*. Infact the largest errors in the numerical wetted surface evaluations are related to the error in the numerical evaluation of dynamic trim. Moreover, it is worth noting that small variations of the dynamic trim imply significant variations of the wetted surface evaluation as also indicated in D. Savitsky and M. Morabito [11].

In particular, the experimental wetted surface is underestimated compared to the real wetted surface and the numerical wetted surface is an overestimation considering the VOF value equal to 0.5. Infact, as was reported in [68], in the estimation of the wetted surface area, a distinction should be made between the area covered by spray and that covered by solid water. It is a common practice to disregard the viscous drag of spray-covered areas and to account for only the viscous drag of the area wetted by solid flow. This practice is questionable but the flow in the spray region is extremely complex and no alternative practices are known. In this study, only the “solid water” has been taken into account to evaluate the experimental wetted surface.

As mentioned above, the use of the transparent bottom hull ensures a full view of the water flow under the hull, and the estimation of the wetted surface. During the towing tank tests, a particular flow phenomenon has been detected at all Fr_∇. This phenomenon consists in two vortex structures under the hull and behind the step, as shown in the video clip in [69].

However, for this study, the speed condition of Fr_∇=3.898 has been chosen because the phenomenon is especially visible (see *Figure 6.5* and *Figure 6.6*).

The vortex structures are also visible in the numerical simulation with an overset mesh approach, as shown in the comparison of two views of the flow under the hull (*Figure 6.5*). The upper picture is a top view of the transparent hull model, showing the unwetted aft body area and a well-developed vortex. This vortex trails downstream into the water, departing from the aft region of the

unwetted aft body area. The lower picture is taken from the numerical solution and shows the isosurface at volume of fraction equal to 0.5. This visualization emphasizes the presence of the unwetted aft body area behind the step, as opposed to the fore body wetted surface. The two visualizations are in good agreement, both in terms of wetted surface extension and in terms of shape of unwetted aft body area.

Similarly, *Figure 6.6* and *Figure 6.7* show two side views of the underwater flow behind the step. Also in this case, the two visualizations show good agreement between the experimental evidence and the numerical results.

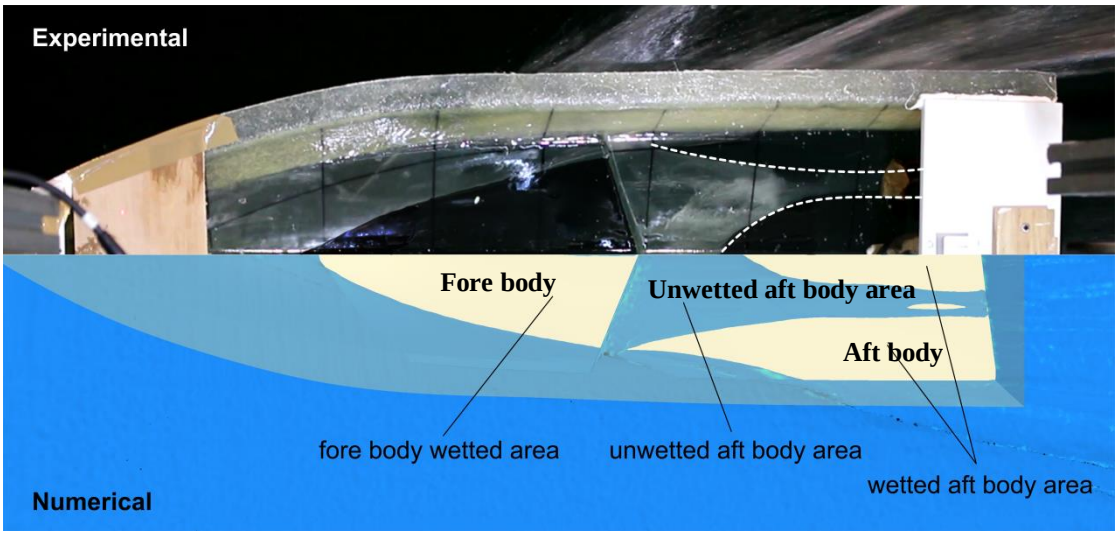

Figure 6. 5 Wetted surface top view at $Fr_{\nabla} = 3.898$, comparison between experimental (top side), and RANSE overset simulation 2.5×10^6 cells (down side), air/water interface as isosurface at VOF = 0.5

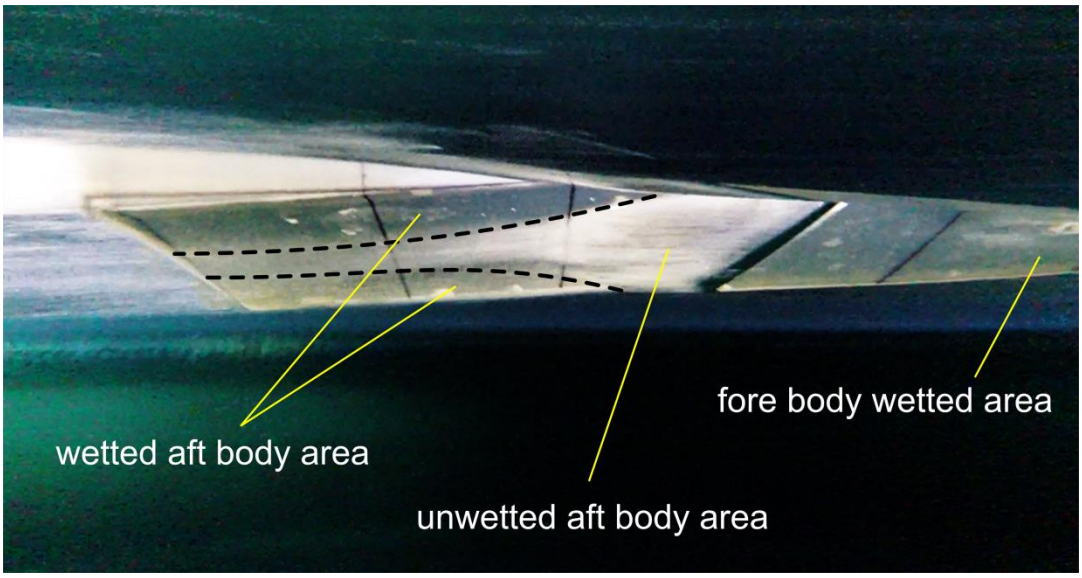

Figure 6. 6 Experimental wetted surface right-side view at $Fr_{\nabla} = 3.898$

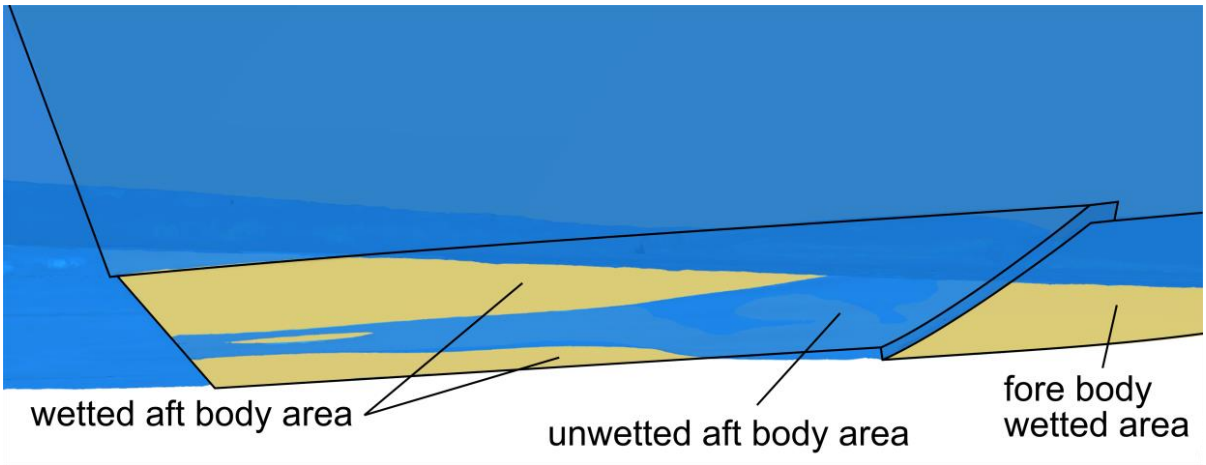

Figure 6. 7 Wetted surface right-side view at Fr_∇ = 3.898, RANSE overset simulation (2.5×10^6 cells), air/water interface as isosurface at VOF = 0.5.

6.3 Analysis of the fluid-dynamics in the unwetted aft body area

A detailed study of the flow patterns in the unwetted aft body area behind the step has been performed at Fr_∇ =3.898. Starting from the experimental values of trim and sinkage in this condition (see *Figure 6.2* and *Figure 6.3*), the zero (DoF) hull has been simulated at the given Froude number with a large eddy simulation (LES) approach on a very fine grid of approximately 12×10^6 cells (see *Figure 6.8*) with the same size of computational domain and boundary conditions previously described for the morphing grid simulation (see [46] for the details of the applied LES formulation).

Successively, the converged solution has been used as the initial condition of further simulations with free heave-and-pitch degrees-of-freedom. The final two-DoF converged solution has been post-processed to gain insight into the complex flow pattern behind the step. The streamlines both in water and in air have been analyzed, and a flow pattern in the unwetted aft body area has been characterized. The flow patterns (in-air and in-water) are clearly visible from the bottom and side views of the LES solution shown in *Figure 6.9*, *Figure 6.10*, *Figure 6.12*, *Figure 6.13*, *Figure 6.14*, *Figure 6.15*, and *Figure 6.16*.

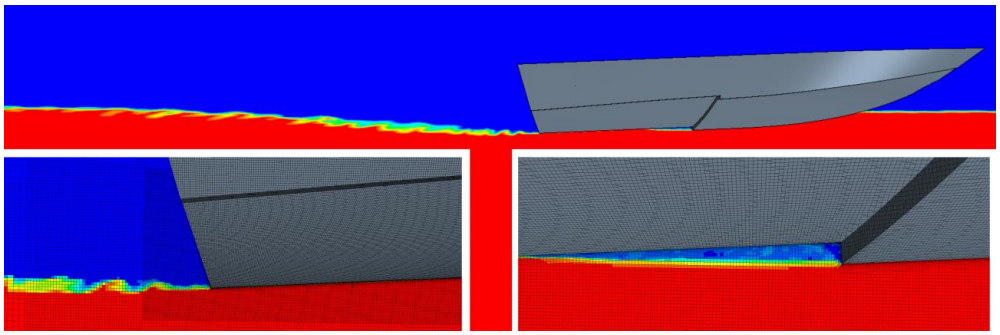

Figure 6. 8 Details of the LES simulation at Fr_{∇} =3.898 with very fine grid used for the flow pattern study in the unwetted aft body area (12×10^6 cells). Contour maps of VOF (red in water; blue in air). See also Figure 6.11.

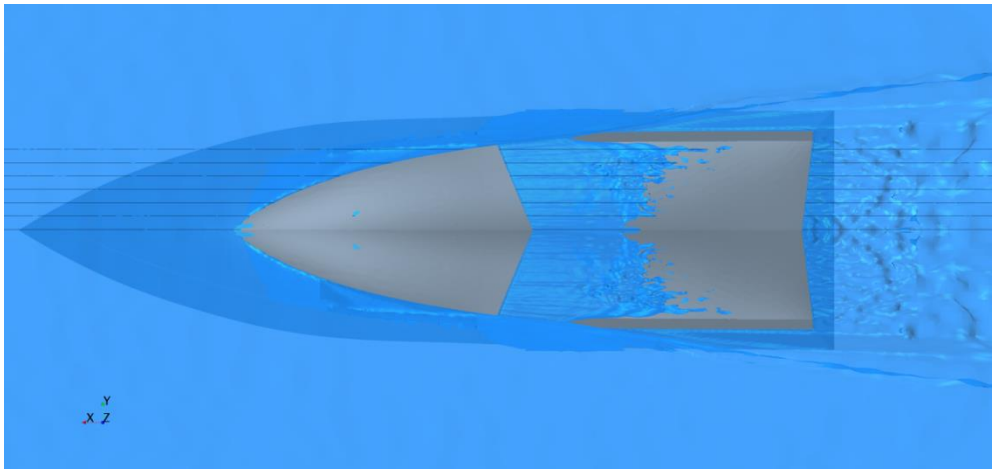

Figure 6. 9 LES simulation at Fr_{∇} = 3.898; bottom view with VOF isosurface at 0.5, and wave cuts (12×10^6 cells)

A bottom view of the LES solution is shown in *Figure 6.9* where some selected streamlines on the air/water interface have been calculated and visualized. The same streamlines are visible in *Figure 6.10*. These representations emphasize the shape of the unwetted aft body area and the extension in the aft region of the step. In particular, the extension of the separated region is evident from the flow field cross sections of *Figure 6.11* at different x-stations (x=0 at the LCB).

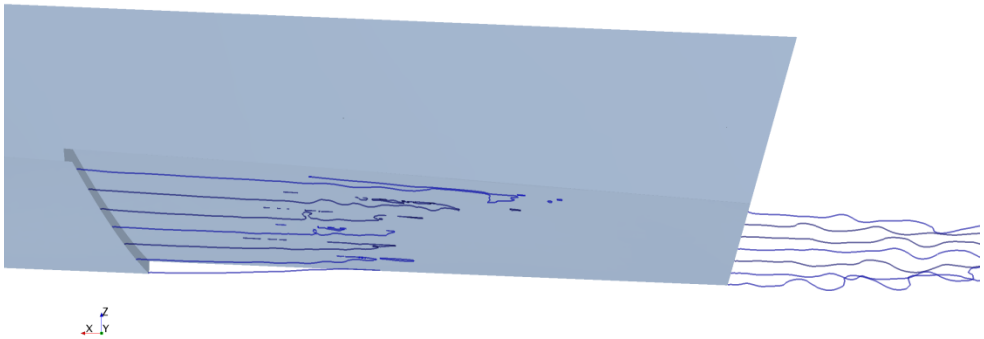

Figure 6. 10 LES simulation at Fr_{∇} = 3.898; side view of wave cuts of VOF isosurface at 0.5, dry region behind the step and stern wake profile

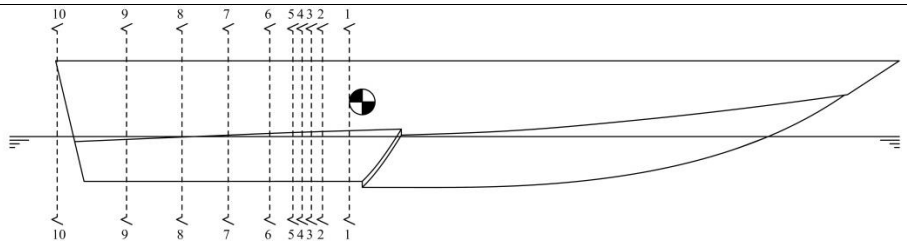

Cross-section indices

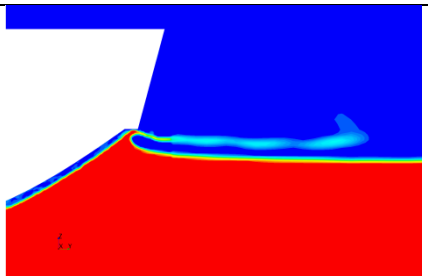

Section 1-1: Δx = 0.014 m

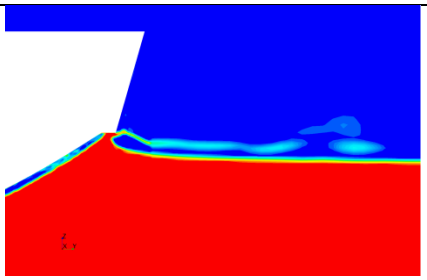

Section 2-2: Δx = 0.043 m

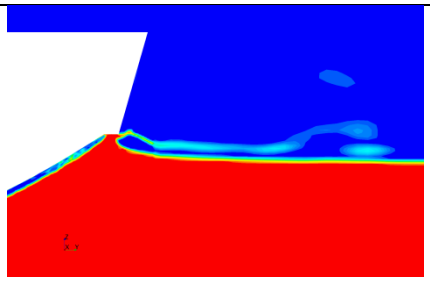

Section 3-3: Δx = 0.055 m

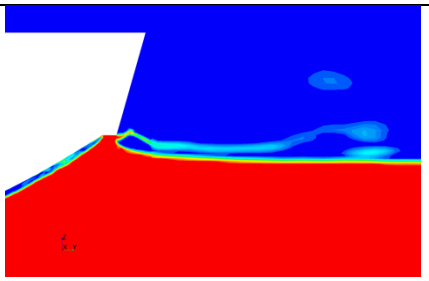

Section 4-4: Δx = 0.065 m

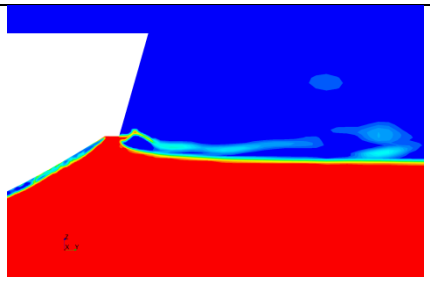

Section 5-5: Δx = 0.075 m

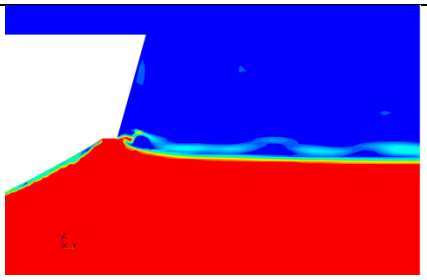

Section 6-6: Δx = 0.100 m

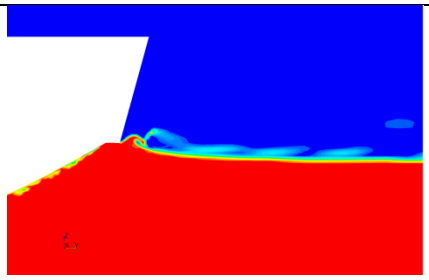

Section 7-7: Δx = 0.145 m

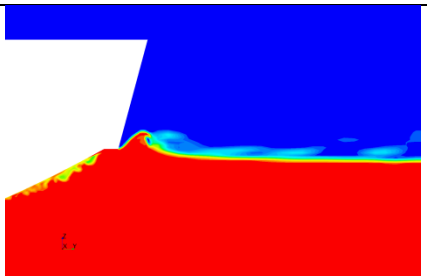

Section 8-8: Δx = 0.195 m

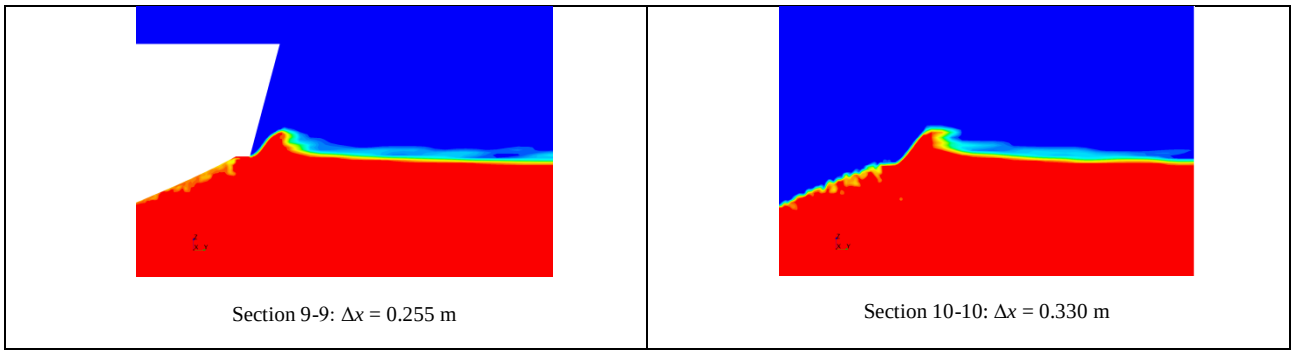

Figure 6. 11 LES simulation; volume fraction contours at different cross sections (at ⊿x from LCB, positive forward), at Fr_∇=3.898. Contour maps of VOF (red in water; blue in air)

A more detailed set of visualizations is given by *Figure 6.12*, *Figure 6.13*, and *Figure 6.14*. The main feature of the flow pattern inside the unwetted aft body area depends on the air inlet (shape and longitudinal position). The air inlet is located at the intersection of the chine with the step, and facing the side of the main flow. A fairly complex 3D flow is visible from the representation of the streamlines. The air particles enter the unwetted area through the inlet and successively propagate inside the air region according to different patterns. Finally, a mix of air and (mostly) water particles flows downstream of the aft body into a visible vortex. The separation of the water-flow induced by the step is similar to what happens in the transom. The pressure of the flow after the separation is the atmospheric pressure. The physics of this 3D-phenomenon is mainly regulated by the Fr_∇ according to [11]. Therefore, according to [18] the cavitation number behind the step is σ = 0.018.

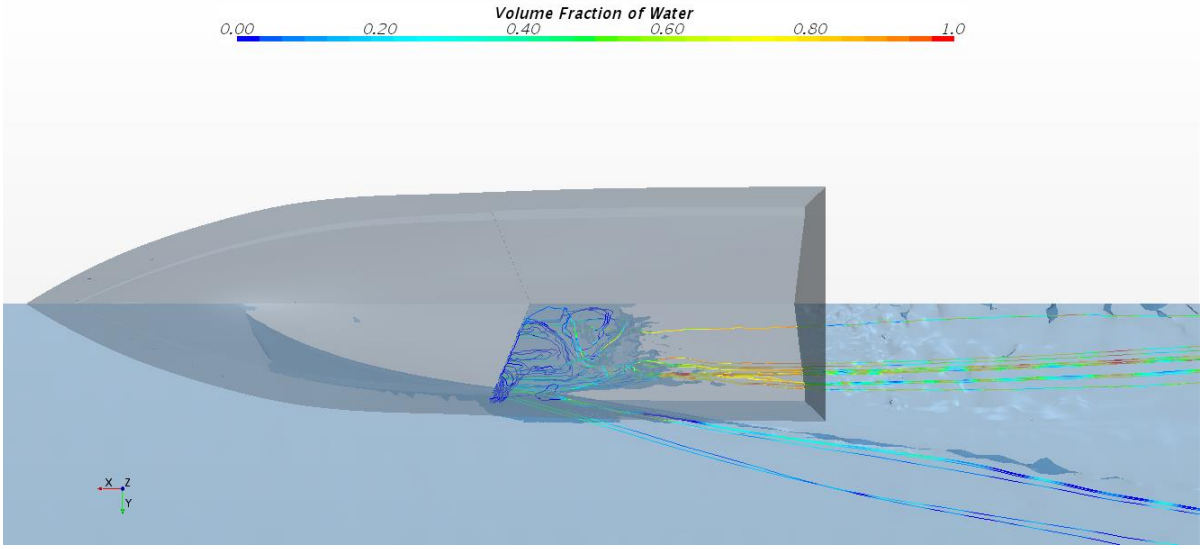

Figure 6. 12 LES simulation at Fr_∇ = 3.898; streamlines in air and water

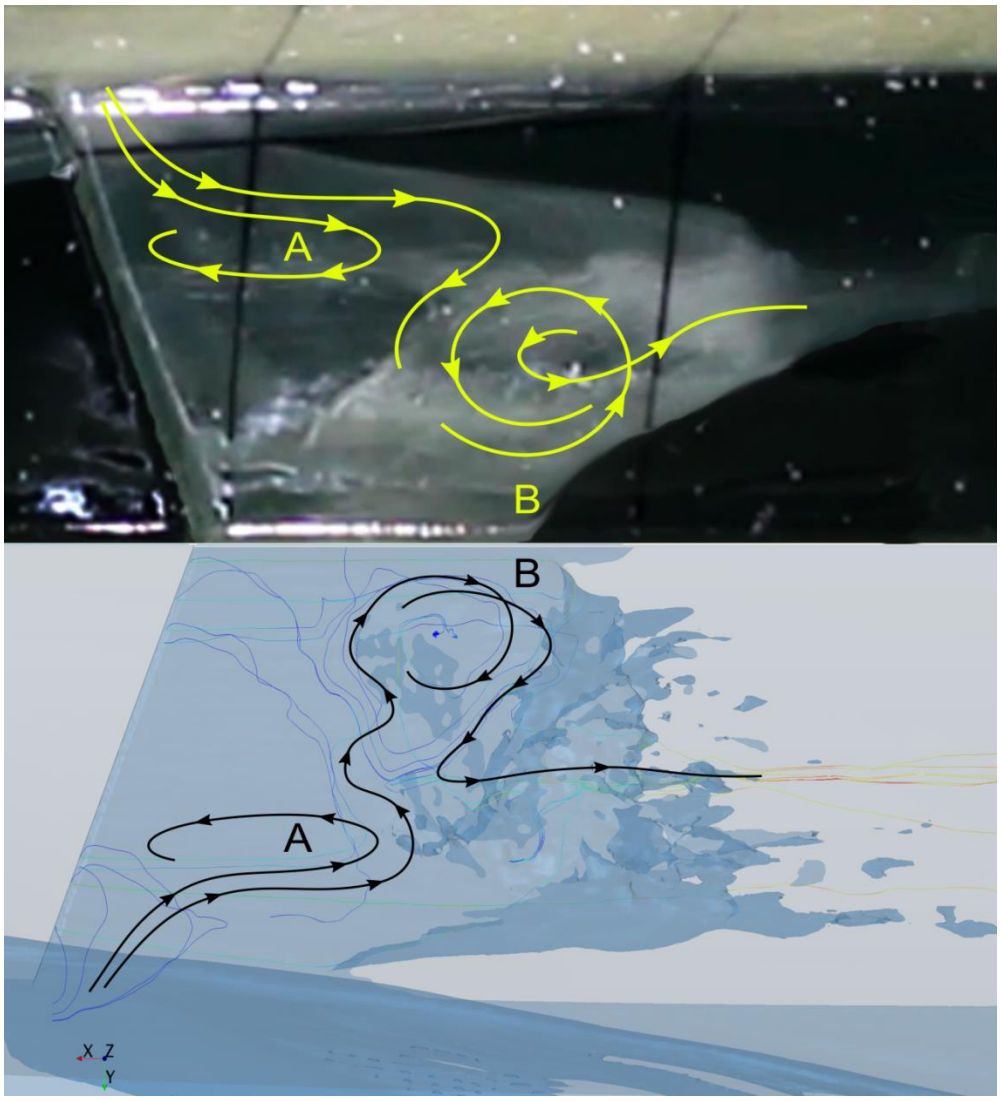

Figure 6. 13 LES simulation at Fr_{∇} = 3.898; flow patterns in the unwetted aft body area, top view

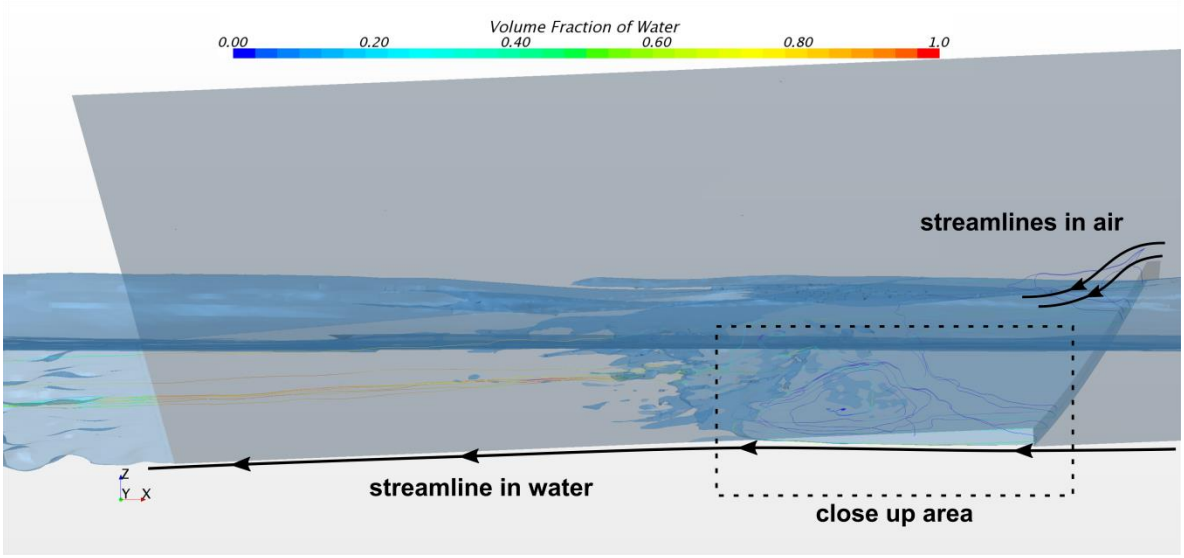

Figure 6. 14 LES simulation at Fr_{∇} = 3.898; side air inlet at the step, side view

A close-up picture of the transparent hull model taken from the experimental test is shown in *Figure 6.13* (upper part). In the photograph, the two-main observed counter-rotating flow patterns are depicted and named pattern A and pattern B. In the lower part of the same figure, a similar visualization taken from the LES solution is reported. Two similar flow patterns are visible by inspection of the numerically calculated streamlines. The complexity of the 3D streamlines is visible in *Figure 6.14* and *Figure 6.15*. The side view of *Figure 6.15* shows that streamlines originating from the inlet propagate according to a recirculating path induced by the external water flow overcoming the step. Finally, a perspective bottom view of the streamlines is shown in *Figure 6.16*.

The flow patterns obtained numerically look similar to the ones observed in towing tank investigations. The same flow patterns seem to be confirmed by ongoing LES simulations on a full scale hull with a very fine grid of 17.7×10^6 cells. The LES simulation has been performed for a speed of 15.5 m/s, (28.5 knots in full scale), equal to $Fr_\nabla = 3.898$. Furthermore, the results in terms of trim angle, and non-dimensional total resistance, sinkage, wetted surface, are comparable respect to the model scale simulation.

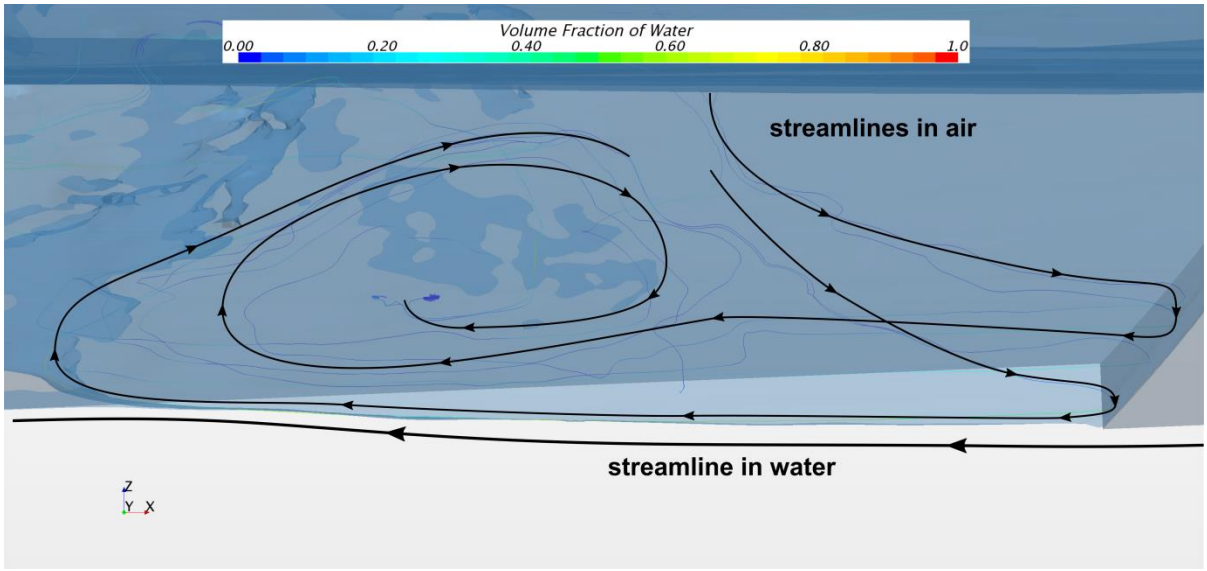

Figure 6. 15 LES simulation at $Fr_\nabla = 3.898$; close up of 3D patterns of air flow in the unwetted aft body area, side view

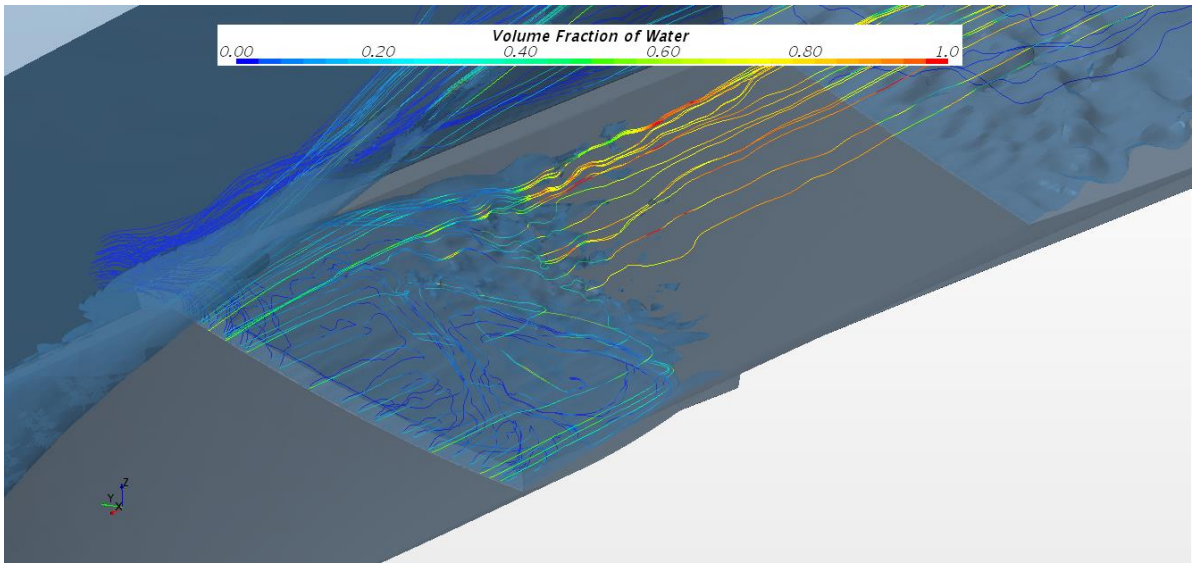

Figure 6. 16 LES simulation at Fr_{∇} = 3.898; perspective view of streamlines in the unwetted aft body area

7

CONCLUSIONS

In this thesis, a new systematic series of eight hull models derived by one stepped hull has been developed, and several experimental tests have been carried out in towing tank to investigate the hulls performances such as total resistance, longitudinal trim angle, sinkage, and wetted surface.

Due to the hull model's low weight and sensitivity to external applied forces, the "down-thrust" methodology has been applied in order to release the model from the instrumentation weight. This approach allowed to attain high precision of data acquisition, such as resistance, sinkage, trim, and dynamic wetted surface measurements. The proposed solution is proven to reproduce with good accuracy the real system of forces exerted by the outboard engines on the transom of the hull in full scale.

The transparent bottom of the hull model allows to observe some unique vortical flow phenomena in the unwetted aft body area behind the step. In detail, a fairly complex 3D flow is visible from the representation of the streamlines. The air particles enter the unwetted area through the air inlet and successively propagate inside the air region according to different patterns. Finally, a mix of air and (mostly) water particles flows downstream of the aft body into a visible vortex. This vortex results to be visible for towing speeds greater than 2.36 m/s ($Fr_{\nabla} > 1.97$).

An uncertainty analysis of the experimental results has been performed in compliance with the ITTC standards.

To confirm this experimental evidence, the same test conditions have been reproduced with CFD simulations for one of the eight models of the new systematic series, by using different unconventional dynamic mesh techniques, which are the overset mesh and the morphing grid.

The results of the overset mesh approach, in spite of being obtained with a greater computational effort, show lower errors (as compared with the experimental case), with respect to those of the morphing grid technique. In detail, the overset mesh ensures high-quality of the simulation results and shows high-adaptability to the wide variations of trim and heave of the stepped hull. This confirms that the numerical results obtained by the overset mesh approach, are closer to the experimental measurements as compared to the morphing grid approach.

The simulation uncertainty analysis shows that the grid represents the main source of simulation numerical error, as already identified in literature. The uncertainty in the non-dimensional variables, such as total resistance/displacement ratio, non-dimensional dynamic sinkage, dynamic trim angle, and non-dimensional dynamic wetted surface, is, for the hull considered in this work, relatively greater when using the morphing grid technique. The validation process highlights that, especially for the dimensionless wetted surface, the comparison error is much greater than the validation uncertainty, which implies that it is necessary to reduce the modeling error. However, by using Large Eddy Simulation (LES) approach on a refined grid, a detailed analysis of the flow in the unwetted aft body area behind the step confirms the existence of the same vortical structures observed experimentally.

In summary, it can be said that regarding the simulation of stepped hull, the use of the overset mesh technique is suitable for the detection, in a sufficiently accurate way, of the total resistance and of the hull running attitude. Conversely, the LES approach is more suitable for the evaluation of the details of water flow phenomena around the hull and wetted surface. Moreover, in the design of planing stepped hull, and in the absence of towing tank tests, a useful methodology is to couple a RANS simulation, performed with the overset mesh technique, for the determination of the global parameters as resistance, trim and sinkage, whereas to use LES approach simulations for any detailed investigation.

Furthermore, a particular vortex pattern in the unwetted aft body area has been observed for a scaled single-step hull model in towing tank tests. At the same time, similar flow patterns have been found in the numerical simulations on a very fine mesh, in which additional details on the 3D flow have been explored in this area.

APPENDIX A

EXPERIMENTAL UNCERTAINTY ANALYSIS

Uncertainty Analysis (UA) in Experimental Fluid Dynamics (EFD) has been also performed according to ITTC [43]. As a first step, UA is performed for each individual variable *r* (model geometry, displacement, speed, resistance, density, running trim, and sinkage). Second, UA is performed for non-dimensional coefficients (R_{TM}/Δ, τ, $Z/\nabla^{1/3}$, and $S/\nabla^{2/3}$). The UA procedure is based on the methodology proposed by [44] with 95% confidence interval, hence, considers normal distributions with a large sample size with estimates of:

- systematic uncertainty, also called bias (B_r) is calculated as Root Sum of Square (RSS) of each elementary error source (*i.e.*, calibration, data acquisition, data reduction, and conceptual bias) group of bias error. The elementary error sources have been divided and separately estimated;
- random uncertainty, also called precision uncertainty, (P_r), is calculated for each run, according to:

$$P_j(S) = KSDev_j \tag{A.1}$$

  where $SDev_j$ represents the standard deviation of j^{th} run, and $K=2$ according to the above-mentioned methodology;
- total uncertainty U_r is a RSS of B_r and P_r.

The bias, precision, and the uncertainties for non-dimensional coefficients (R_{TM}/Δ, τ, $Z/\nabla^{1/3}$, $S/\nabla^{2/3}$ and Fr_∇) are summarized in the table below.

Table A. 1 Experimental uncertainty analysis

Description	***Term***	***Speed***								***Units***
		1.290	2.357	3.131	4.629	5.368	6.336	7.300	8.054	[m/s]
Model Speed										
	Fr_∇	1.077	1.968	2.614	3.864	4.481	5.289	6.094	6.723	[adim]
	B_V	6.97E-04	6.97E-04	3.13E-03	4.62E-03	5.36E-03	6.33E-03	7.29E-03	8.05E-03	[adim]
		22.62%	8.05%	4.73%	2.22%	1.66%	1.20%	0.90%	0.74%	% of $B_{Fr\nabla}$
	B_∇	1.29E-03	2.35E-03	3.13E-03	4.62E-03	5.36E-03	6.33E-03	7.29E-03	8.05E-03	[adim]
		77.38%	91.95%	95.27%	97.78%	98.34%	98.80%	99.10%	99.26%	% of $B_{Fr\nabla}$
	$B_{Fr\nabla}$	1.47E-03	2.46E-03	3.20E-03	4.68E-03	5.41E-03	6.37E-03	7.33E-03	8.08E-03	[adim]
		0.14%	0.12%	0.12%	0.12%	0.12%	0.12%	0.12%	0.12%	% of Fr_∇
	$P_{Fr\nabla}$	4.38E-03	4.80E-03	5.22E-03	1.08E-02	1.36E-02	1.41E-02	2.08E-02	2.50E-02	[adim]
	$U_{Fr\nabla}$	4.61E-03	5.39E-03	6.13E-03	1.18E-02	1.47E-02	1.54E-02	2.21E-02	2.63E-02	[adim]
		0.43%	0.27%	0.23%	0.30%	0.33%	0.29%	0.36%	0.39%	% of Fr_∇
Model Resistance Ratio										
	R_{TM}/Δ	0.100	0.178	0.204	0.256	0.312	0.407	0.491	0.555	[N/N]
	B_R	6.62E-04	6.68E-04	6.71E-04	6.78E-04	6.86E-04	7.05E-04	7.25E-04	7.42E-04	[N/N]
		97.49%	97.54%	97.56%	97.61%	97.67%	97.78%	97.90%	98.00%	% of $B^2_{RT/\Delta}$
	B_Δ	1.06E-04	1.06E-04	1.06E-04	1.06E-04	1.06E-04	1.06E-04	1.06E-04	1.06E-04	[N/N]
		2.51%	2.46%	2.44%	2.39%	2.33%	2.22%	2.10%	2.00%	% of $B^2_{RT/\Delta}$
	P_R	4.08E-05	1.54E-07	1.54E-07	3.45E-07	2.25E-06	2.25E-06	2.25E-06	1.53E-06	[N/N]
	$U_{RTM/\Delta}$	6.72E-04	6.76E-04	6.79E-04	6.86E-04	6.95E-04	7.13E-04	7.33E-04	7.50E-04	[N/N]
		0.67%	0.38%	0.33%	0.27%	0.22%	0.18%	0.15%	0.14%	% of R_T/Δ

Trim Angle

τ	2.23	3.55	3.27	3.27	2.87	2.69	2.52	2.58	[deg]
$B_{\tau\text{-}cw}$	0.001	0.001	0.001	0.001	0.001	0.001	0.001	0.001	[deg]
	0.01%	0.01%	0.01%	0.01%	0.01%	0.01%	0.01%	0.01%	% of B_τ^2
$B_{\tau\text{-}ix}$	0.050	0.050	0.050	0.050	0.050	0.050	0.050	0.050	[deg]
	33.33%	33.33%	33.33%	33.33%	33.33%	33.33%	33.33%	33.33%	% of B_τ^2
$B_{\tau\text{-}iy}$	0.050	0.050	0.050	0.050	0.050	0.050	0.050	0.050	[deg]
	33.33%	33.33%	33.33%	33.33%	33.33%	33.33%	33.33%	33.33%	% of B_τ^2
$B_{\tau\text{-}iz}$	0.050	0.050	0.050	0.050	0.050	0.050	0.050	0.050	[deg]
	33.33%	33.33%	33.33%	33.33%	33.33%	33.33%	33.33%	33.33%	% of B_τ^2
B_τ	0.087	0.087	0.087	0.087	0.087	0.087	0.087	0.087	[deg]
	3.88%	2.44%	2.65%	2.65%	3.02%	3.22%	3.44%	3.36%	% of B_τ^2
P_τ	0.004	0.003	0.003	0.004	0.012	0.014	0.012	0.012	[deg]
U_τ	0.087	0.087	0.087	0.087	0.087	0.088	0.087	0.087	[deg]
	3.89%	2.44%	2.65%	2.65%	3.04%	3.26%	3.47%	3.39%	% of τ

Sinkage

$Z/\nabla^{1/3}$	-0.080	0.010	0.048	0.085	0.139	0.147	0.151	0.181	[mm/mm]
$B_{ZCG\text{-}cw}$	0.1	0.1	0.1	0.1	0.1	0.1	0.1	0.1	[mm]
	3.3E-03	3.3E-03	3.3E-03	3.3E-03	3.3E-03	3.3E-03	3.3E-03	3.3E-03	% of B_{ZCG}^2
$B_{ZCG\text{-}lf}$	1.00	1.00	1.00	1.00	1.00	1.00	1.00	1.00	[mm]
	0.33	0.33	0.33	0.33	0.33	0.33	0.33	0.33	% of B_{ZCG}^2
$B_{ZCG\text{-}la}$	1.00	1.00	1.00	1.00	1.00	1.00	1.00	1.00	[mm]
	0.33	0.33	0.33	0.33	0.33	0.33	0.33	0.33	% of B_{ZCG}^2
$B_{ZCG\text{-}lb}$	1.00	1.00	1.00	1.00	1.00	1.00	1.00	1.00	[mm]
	0.332	0.332	0.332	0.332	0.332	0.332	0.332	0.332	% of B_{ZCG}^2
B_{ZCG}	1.735	1.735	1.735	1.735	1.735	1.735	1.735	1.735	[mm]
	14.85%	114.14%	24.96%	14.03%	8.51%	8.07%	7.83%	6.56%	% of B_{ZCG}^2
P_{ZCG}	6.365	7.120	6.846	4.046	8.755	5.870	6.556	4.864	[mm]
$B_{Z/\nabla^{1/3}}$	0.016	0.012	0.014	0.017	0.023	0.024	0.025	0.028	[mm/mm]
	20.64%	115.04%	28.79%	20.06%	16.67%	16.45%	16.34%	15.77%	% of $Z/\nabla^{1/3}$
$P_{Z/\nabla^{1/3}}$	0.025	0.024	0.024	0.019	0.036	0.030	0.032	0.032	[mm/mm]
$U_{Z/\nabla^{1/3}}$	0.030	0.027	0.028	0.025	0.043	0.038	0.040	0.043	[mm/mm]

	-37.26%	261.37%	58.95%	29.82%	30.96%	26.01%	26.56%	23.52%	% of $Z/\nabla^{1/3}$
Model geometry									
$S/\nabla^{2/3}$				6.730					
B_S				0.284					$[m^2/m^2]$
				80.81%					% of $B^2_{S/\nabla 2/3}$
$B_{\bar{V}^{2/3}}$				0.138					$[m^2/m^2]$
				19.19%					% of $B^2_{S/\nabla 2/3}$
$P_{S/\bar{V}^{2/3}}$				0.032					[m/m]
$U_{S/\bar{V}^{2/3}}$				0.317					$[m^2/m^2]$
				4.72%					%of $S/\nabla^{2/3}$
Density									
ρ				1000					$[kg/m^3]$
B_{r1}				0.071					$[kg/m^3]$
				1.15%					% of B_ρ^2
B_{r2}				0.07					$[kg/m^3]$
				1.12%					% of B_ρ^2
B_{r3}				0.655					$[kg/m^3]$
				97.74%					% of B_ρ^2
B_r				0.663					$[kg/m^3]$
				0.066%					% of B_r
P_r				1.00					$[kg/m^3]$
U_ρ				1.20					$[kg/m^3]$
				0.12%					% of r

APPENDIX B

NUMERICAL UNCERTAINTY ANALYSIS

The validation uncertainty (U_V) is given by:

$$U_V^2 = U_D^2 - U_{SN}^2 \tag{B.1}$$

where U_D is the uncertainty of the experimental data.

The comparison error E is defined as the difference between the experimental data (D) and numerical simulation result (Sn), as reported below:

$$E = D - S_n \tag{B.2}$$

According to ITTC procedures [70], numerical simulation uncertainty U_{SN} is mainly composed of iterative (U_I), grid (U_G), and time-step (U_{TS}) uncertainty, as follows:

$$U_{SN}^2 = U_I^2 + U_G^2 + U_{TS}^2 \tag{B.3}$$

According to Wilson et al.[71], the most important source of uncertainty of the numerical results is the grid.

The sources of uncertainty have been evaluated for each of the simulation technique, i.e., overset grid and morphing grid.

The numerical uncertainty evaluation has been performed by using two different methods: the Grid Convergence Index (*GCI*) method and the Correction Factor (*CF*) method.

The general form of the uncertainty evaluation, based on the generalized Richardson Extrapolation (RE) method, can be written as follows:

$$U_k = F_S \left| \frac{\varepsilon_{21_k}}{r_k^{p_k} - 1} \right| \tag{B.4}$$

where ε_{21k} is the solution changes for the *k*-input parameter between the solutions fine (S_{n1k}) to medium (S_{n2k}) and coarse (S_{n3k}), r_k is the constant refinement ratio, p_k is the observed order of accuracy, and F_S is the safety factor.

Furthermore, another parameter is the convergence ratio (R_k), which provides information about the convergence/divergence of a solution. The R_k value has been determined by the following ratio:

$$R_k = \varepsilon_{21_k} / \varepsilon_{32_k} \tag{B.5}$$

There are four kinds of possible convergence conditions: monotonic convergence ($0< R_k <1$), oscillatory convergence ($R_k <0$ and $|R_k|<1$), monotonic divergence ($R_k >1$), and oscillatory divergence ($R_k <0$ and $|R_k|>1$). Since $0< R_k <1$, the monotonic convergence is satisfied.

The two different solution verification methods used in this study differ in the choice of the safety factor (FS).

The GCI method in Equation B.5, proposed by[72, 73], is used extensively and is recommended, for example, by the American Society of Mechanical Engineer (ASME)[74] and the American Institute of Aeronautics and Astronautics (AIAA)[75]. Roache recommended for three or more grids analyzed 1.25 as FS value.

The other method used is the CF in Equation B.6, as discussed in [76], which uses a variable value of FS, called correction factor (C_k). In the CF method, the uncertainty of the error depends on how much the solutions are close to the asymptotic range. The expressions defined the uncertainties were reported by[77]:

$$U_k = 1.25 \cdot \left| \frac{\varepsilon_{21_k}}{r_k^{p_k} - 1} \right| \tag{B.6}$$

$$U_k = \begin{cases} [9.6(1-C_k)^2 + 1.1]\left|\dfrac{\varepsilon_{21_k}}{r_k^{p_k} - 1}\right|, & |1-C_k| < 0.125 \\ [2|1-C_k| + 1]\left|\dfrac{\varepsilon_{21_k}}{r_k^{p_k} - 1}\right|, & |1-C_k| \geq 0.125 \end{cases} \quad \text{(B.7)}$$

Table B. 1 Overset grid case: uncertainty analysis

	Grid ratio	R_G	p_G	$\%U_G$ ***GCI***	$\%U_G$ ***CF***	$\%U_{SN}$	$\%U_D$	$\%U_V$	$\%\|E\|$
R_{TM}/Δ	√2	0.47	1.44	9.06	16.62	16.62	0.27	16.6	3.8
τ	√2	0.43	-2.45	3.23	0.37	3.23	2.65	4.2	3.7
$Z/\nabla^{1/3}$	√2	1.65	-2.16	N.A.	N.A.	N.A.	29.82	N.A.	42.1
$S/\nabla^{2/3}$	√2	0.89	-0.34	0.96	0.60	0.96	4.72	4.8	31.0

*U_G was expressed as a percentage value of the simulation solution for the finest grid

Table B. 2 Morphing grid case: uncertainty analysis

	Grid ratio	R_G	p_G	$\%U_G$ ***GCI***	$\%U_G$ ***CF***	$\%U_{SN}$	$\%U_D$	$\%U_V$	$\%\|E\|$
R_{TM}/Δ	√2	0.46	-2.27	6.92	0.49	6.92	0.27	6.9	18.3
τ	√2	0.78	-0.71	25.69	11.59	25.69	2.65	25.8	9.9
$Z/\nabla^{1/3}$	√2	0.90	-0.30	43.77	28.14	43.77	29.82	52.9	43.1
$S/\nabla^{2/3}$	√2	0.95	-0.14	13.65	11.95	13.65	4.72	14.4	53.2

*U_G was expressed as a percentage value of the simulation solution for the finest grid

REFERENCES

[1] F. Stern, J. Yang, Z. Wang, H. Sadat-Hosseini, M. Mousaviraad, S. Bhushan e T. Xing, «Computational Ship Hydrodynamics: Nowadays and Way Forward,» International Shipbuilding Progress, pp. 3-105; 2013

[2] G2010, «Gothenburg 2010 A Workshop on CFD in Ship Hydrodynamics,» Gothenburg, 2010

[3] L. Zou e L. Larsson, «A Verification and Validation Study Based on Resistance Submissions to the Gothenburg 2010 Workshop on Numerical Ship Hydrodynamics,» in Proceedings of 14th Numerical Towing Tank Symposium, Southampton, 2011.

[4] ITTC, «Specialist Committee on CFD in Marine Hydrodynamics - 27th ITTC,» 2014.

[5] W. Sottorf, «Experiments with Planing Surfaces,» 1934.

[6] S. Brizzolara and D. Villa, "CFD Simulation of Planing Hulls", in *7th International Conference On High-Performance Marine Vehicles*, Melbourne, October 11–15, 2010.

[7] F. De Luca, S. Mancini, S. Miranda and C. Pensa, "An Extended Verification and Validation Study of CFD Simulations for Planing Hulls "*Journal of Ship Research*", vol. 60, no. 2, pp. 101-118, 2016.

[8] R. Azcueta, V. Bertram, «High-performance marine vehicles as naval platforms», HIPER, vol. 2, pp. 22-33, 2002.

[9] SNAME, Transaction, 1911.

[10] J. Danielsson, J. Stomquist, «Conceptual design of a high-speed superyacht tender», KTH Marina system Centre for Naval Architecture, 2012.

[11] D. Savitsky, M. Morabito, «Surface wave contours associated with the forebody wake of stepped planing hulls,» Marine Technology 47, pp 1-16, January 2010.

[12] J. Kuttenkeuler, «Sailing for Performance SD2706, Lecture 1, Intro Fin,» KTH, Stockholm, Center of Naval Architecture, 2011.

[13] D. Savitsky, «Hydrodynamic design of planing hulls», Marine Technology, pp. 71-95, October 1964.

[14] D. Savitsky, MF. DeLorme, R. Datla, «Inclusion of whisker spray drag in performance prediction method for high-speed planing hulls,» Marine Technology 44, pp. 35–56, 2007.

[15] D. Tauton, D. Hudson, R. Shenoi, «Characteristics of series of high speed hard chine planing hulls-part 1: performance in calm water,» International Small Craft Technology 152, pp. 55-75, 2010

[16] D. Svahn, «Performance prediction of hulls with transverse steps,» M.Sc. thesis, KTH Centre for Naval Architecture, Stockolm, Sweden, 2009.

[17] W. R. Garland, K. J. Maki, «A Numerical Study of a Two-dimensional Stepped Planing Surface,» Journal of Ship Production 28, n. 2, pp. 60-72, 2012.

[18] M. V. Makasyeyev, «Numerical Modeling of Cavity Flow on Bottom of a Stepped Planing Hull,» Proceedings of the 7th International Symposium on Cavitation (CAV 2009). Ann Arbour, pp. 17-22, August 2009.

[19] K. I. Matveev, «Two-dimensional Modeling of Stepped Planing Hulls with Open and Pressurized Air Cavities,» International Journal of Naval Architecture and Ocean Engineering 4, n. 2, pp. 162-171, 2012.

[20] K. I. Matveev, «Hydrodynamic Modeling of Semi-Planing Hulls with Air Cavities,» International Journal of Naval Architecture and Ocean Engineering 3, n. 3, pp. 500-508, 2015.

[21] S. Brizzolara, A. Federici, «Designing of Planing Hulls with Longitudinal Steps: CFD in Support of Traditional Semi-Empirical Methods,» Proceedings of Design and Construction of Super & Mega Yachts,Genoa 8-9 May, 2013.

[22] P. Lotfi, M. Ashrafizaadeh, R. K. Esfahan, «Numerical Investigation of a Stepped Planing Hull in Calm Water,» Ocean Engineering, n. 94, pp. 103-110, 2015.

[23] M. Bakhtiari, S. Veysi, H. Ghassemi, «Numerical Modeling of the Stepped Planing Hull in Calm Water,» International Journal of Engineering, Transactions B: Applications 29, n. 2, 2016.

[24] L. Vitiello, «Significant improvement of the ship energy efficiency via design of experiments and regression analysis,» PhD thesis, Department of Naval Engineering, University of Naples “FedericoII”, Naples, 2014.

[25] E. P. Clement, D. L. Blount, «Resistance tests of a systematic series of planing hull forms,» Transactions of The Society of Naval Architects and Marine Engineers, Volume 71, 1963.

[26] H. D. Holling, E. N. Hubble, «Model resistance data of Series 65 hull forms applicable to hydrofoils and planning craft,» Naval Ship Research and Development Center, Report No. DTNSRDC 4141, Bethesda, 1974.

[27] B. J. Metcalf, L. Faul, E. Bumiller, J. Slutsky, «Resistance tests of a systemetic series of U.S. Coast Guard planing hulls,» Carderock Division, Naval Surface Warefare Center, Report No. NSWCCD-50-TR-2005/063, 2005.

[28] S. Mancini, «The Problem of the Verification and Validation Processes of CFD Simulations of Planing Hulls,» PhD Thesis, Department of Industrial Engineering, Naples: University of Naples "Federico II", 2016.

[29] G. Fridsma, «A systematic study of the roughwater performance of planing boats,» Stevens Institute of Technology, Report No. 1275, 1969.

[30] G. Fridsma, «A systematic study of the roughwater performance of planing boats (Irregular Waves - Part II),» Stevens Institute of Technology, Report No. 1495, 1971.

[31] E. E. Zarnick, C. R. Turner, «Rough water performance of high length to beam ratio planing boats,» David W. Taylor Naval Ship Research and Development Center, Report No. DTNSRDC/SPD-0973-01, Bethesda, Maryland, 1981.

[32] A. Rosen, «Loads and responses for planing craft in waves,» in Division of naval Systems, Aeronautical and Vehicle Engineering, KTH PhD, Stockholm, 2004.

[33] A. Rosen, K. Garme, «Model experiment addressing the impact pressure distribution on planing craft in waves,» Transactions of the Royal Institution of Naval Architects, Volume 146, 2004.

[34] K. Garme, J. Hua, «A method to analyse seakeeping model measurements in time domain,» in Proceedings of the Ninth International Offshore and Polar Engineering Conference (ISOPE-99). J. S. Chung, M. Olagnon, C. H. Kim, and A. Francescutto, pp. 629-634, 1999.

[35] M. Peters, «Peter on (fast) powerboats part 2,» Professional Boat Builder, n. 127, Oct/Nov 2010.

[36] Akers, «Dancing a fine line,» Professional Boat Builder, Oct/NOV 2003.

[37] B. Acampora, «SM racer: designand operation of one of the world's fastest monohulls,» MT, vol. 32, July 1995.

[38] P. Clement E.P., «Stepless and stepped planing hulls graph for performance prediction and design, report n° 1490,» DTMB, 1964.

[39] E.P. Clement, «A lifting approach to planing boat design, report n 1902,» 1964.

[40] SNAME, «Principles of naval architecture,» vol. second, Edward V Lewis.

[41] ITTC, «Recommended Procedures and Guidelines 7.5-01-01-01, » 2002.

[42] L. Vitiello and S. Miranda, "Towing tank test of stepped hull C03 (2016) - University of Naples Federico II, Italy," 2016. [Online]. Available: https://dx.doi.org/10.6084/m9.figshare.3466010.v1

[43] ITTC, «Recommended Procedures and Guidelines 7.5-02-02-02,» 2002.

[44] H. Coleman, W. Steel, «Experimental and Uncertainty Analysis for Engineers,» 2nd ed., John Wiley & Sons, New York, NY, 1999.

[45] F. Menter, «Two-equation Eddy-viscosity Turbulence Model for Engineering Applications,» AIAA Journal, vol. 30, pp. 2066-2072, 1994.

[46] CD-Adapco , «STAR CCM+ User's Guide Version 9.06,» 2014.

[47] H. K. Versteeg e W. Malalasekera, «An Introduction to Computational Fluid Dynamic The Finite Volume Method,» Longman Scientific & Technical, 1995.

[48] J. Wackers, B. Koren, H. C. Raven, A. van der Ploeg, A. R. Starke, G. B. Deng, P. Queutey, M. Visonneau, T. Hino e K. Ohashi, «Free-Surface Viscous Flow Solution Methods for Ship Hydrodynamics,» Archive of Computational Methods in Engineering, n. 18, pp. 1-41, 2011.

[49] C. W. Hirt e B. D. Nichols, «Volume of Fluid (VOF) Method for the Dynamics of Free Boundaries,» Journal of Computational Physics, n. 39, p. 201–225, 1981.

[50] C. Bohm, «A Velocity Prediction Procedure for Sailing Yachts Based on Integrated Fully Coupled RANSE-Free-Surface Simulations,» Delft, 2014.

[51] J. Wackers, B. Koren, H. C. Raven, A. van der Ploeg, A. R. Starke, G. B. Deng, P. Queutey, M. Visonneau, T. Hino e K. Ohashi, «Free-Surface Viscous Flow Solution Methods for Ship Hydrodynamics,» Archive of Computational Methods in Engineering, n. 18, pp. 1-41, 2011.

[52] O. Ubbink, «Numerical predictions of two fluid systems with sharp interfaces,» 1997.

[53] S. Muzaferija e M. Peric, «Computation of Free Surface Flows Using Interface-Tracking and Interface-Capturing methods,,» in Nonlinear Water Wave Interaction, Southampton, WIT Press, 1999.

[54] V. Andrillion e B. Alessandrini, «A 2D+T VOF Fully Coupled Formulation for Calculation of Breaking Free Surface Flow,» in Proceedings of the 24th Symposium on Naval Hydrodynamics, 2003.

[55] J. Ferziger e M. Peric, «Computational Method for Fluid Dynamics», Springer-Verlaag, 2003.

[56] I. M. Viola, R. G. Y. Flay e R. Ponzini, «CFD Analysis of the Hydrodynamic Performance of Two Candidate America's Cup AC33 Hulls,» International Journal of Small Craft Technology, vol. 154, n. B1-B12, 2012.

[57] P. M. Carrica, R. V. Wilson, R. W. Noack e F. Stern, «Ship Motions Using Single-Phase Level Set with Dynamic Overset Grids,» Computers & Fluids, vol. 36, n. 9, pp. 1415-1433, 2007.

[58] C. Bertorello, E. Begovic e S. Mancini, «Hydrodynamic Performances of Small Size Swath Craft,» Brodogradnja Shipbuilding, vol. 66, n. 4, December 2015.

[59] T. Tezdogan, Y. K. Demirel, P. Kellet, M. Khorasanchi e A. Incecik, «Full-Scale Unsteady RANS-CFD Simulations of Ship Behaviour and Performance in Head Seas due to Slow Steaming,» Ocean Engineering, n. 97, pp. 186-206, 2015.

[60] E. Begovic, A. H. Day, A. Inceçik, S. Mancini e D. Pizzirusso, «Roll Damping Assesment of Intact and Damaged Ship by CFD and EFD Methods,» in Proceedings of the 12th International Conference on the Ship Stability of Ship and Ocean Vehicles, Glasgow, 2015.

[61] A. Swidan, W. Amin, D. Ranmuthugala, G. Thomas e I. Penesis, «Numerical Prediction of Symmetric Water Impact Loads on Wedge Shaped Hull Form Using CFD,» World Journal of Mechanics, n. 3, pp. 311-318, November 2013.

[62] J. Y. Kang e B. S. Lee, «Mesh-Based Morphing Method for Rapid Hull Form Generation,» Computer-Aided Design, n. 42, pp. 970-976, 2010.

[63] M. E. Biancolini e I. M. Viola, «Sails Trim Optimisation Using CFD and RBF Mesh Morphing,» Computers & Fluids, n. 93, p. 46–60, 2014.

[64] A. de Boer, M. S. Schoot e H. Bijl, «Mesh Morphing Based on Radial Function Interpolation,» Computers and Structures, vol. 85, pp. 784-795, 2007.

[65] M. E. Biancolini, «Mesh Morphing and Smoothing by Means of Radial Basis Functions (RBF): A Practical Example Using Fluent and RBF Morph», IGI Global, 2012.

[66] ITTC, Recommended Procedures and Guidelines, «Practical Guidelines for Ship CFD Applications», 7.5-03-02-03, 2011.

[67] S. M. Mousaviraad, Z. Wang and F. Stern, «URANS Studies of Hydrodynamic Performance and Slamming Loads on High-Speed Planing Hulls in Calm Water and Waves for Deep and Shallow Conditions,» *Applied Ocean Research*, vol. 51, pp. 222-240, 2015.

[68] ITTC, Recommended Procedures and Guidelines, «Testing and Extrapolation Methods High Speed Marine Vehicles Resistance Test 7.5-02-05-01», 2002.

[69] L. Vitiello and Miranda, S., «Propulsive Performance Analysis of a Stepped Hull by Model Test Results and Sea Trial Data,» in *High Speed Marine Vehicles Symposium, ISBN 9788890611216*, Napoli, 2014.

[70] ITTC, « Uncertainty Analysis in CFD Verfication an Validation 7.5-03-01-01,» 2008

[71] R. V. Wilson, F. Stern, H. W. Coleman and E. G. Paterson, «Comprehensive Approach to Verification and Validation of CFD Simulations - Part 2: Application for RANS Simulation of a Cargo/Container Ship,» *Journal of Fluids Engineering*, vol. 123, pp. 803-810, 2001.

[72] P. J. Roache, «Verification and Validation in Computational Science and Engineering», New Mexico: Hermosa Publishers, 1998.

[73] P. J. Roache, «Code Verification by the Method of Manufactured Solutions,» *Journal of Fluids Engineering,* vol. 1, no. 124, pp. 4-10, 2002.

[74] I. B. Celik, U. Ghia, P. J. Roache, C. J. Freitas, H. Coleman and P. E. Raad, «Procedure for estimation and reporting of uncertainty due to discretization in CFD applications,» vol. 130, 2008.

[75] R. R. Cosner, W. L. Oberkampf, C. L. Rumsey, C. Rahaim and T. Shih, «AIAA Committee on standards for computational fluid dynamics: status and plans,» Reno, NV, USA, 2006.

[76] F. Stern, R. V. Wilson, H. W. Coleman and E. G. Paterson, «Comprehensive Approach to Verification and Validation of CFD Simulations - Part 1: Methodology and Procedures,» *Journal of Fluids Engineering,* vol. 123, pp. 793-802, December 2001.

[77] R. Wilson, J. Shao and F. Stern, «Discussion: Criticism of the Correction Factor», *Journal of Fluids Engineering,* vol. 126, July 2004.

ACKNOWLEDGEMENTS/RINGRAZIAMENTI

Con l'enorme gioia di tagliare un traguardo così importante, desidero ringraziare prima di tutto il Prof. Salvatore Miranda per avermi seguito con pazienza ed esperienza, con consigli preziosi sui contenuti e sulle modalità di compilazione del presente elaborato, contribuendo in maniera significativa alla mia formazione.

Desidero ringraziare i Proff. Fabio Bozza e Michele Grassi per avermi guidato in questo corso di Dottorato.

Un ringraziamento particolare va ai Proff. Claudio Pensa, Agostino De Marco, Ermina Begovic, Ernesto Fasano e all'Ing. Fabio De Luca con i quali ho quotidianamente collaborato in tutte le mie attività svolte durante il corso di Dottorato.

Un forte ringraziamento va ai colleghi Ingg. Luigi Vitiello e Simone Mancini per la disponibilità e il grande supporto che mi hanno concesso fin dai primi giorni in cui ho intrapreso questo percorso.

Infine un ringraziamento speciale va alla mia famiglia, in particolare a mia madre, per il forte incoraggiamento morale che non è mi mancato durante questi tre anni e alla mia fidanzata Marialaura, che mi ha quotidianamente sopportato e supportato nei momenti più significativi di questo percorso.